UNIVERSITY OF SOUTHAMPTON

A Study of X-ray Binaries in the Local Universe

by

Tana Dale Joseph

A thesis submitted in partial fulfillment for the
degree of Doctor of Philosophy

in the
Faculty of Physical Sciences and Engineering
Physics and Astronomy

27 June, 2013

UNIVERSITY OF SOUTHAMPTON

ABSTRACT

FACULTY OF PHYSICAL SCIENCES AND ENGINEERING

Physics and Astronomy

Doctor of Philosophy

A STUDY OF X-RAY BINARIES IN THE LOCAL UNIVERSE

by Tana Dale Joseph

In this thesis I present the research carried out on X-ray binaries in the Local Universe. These X-ray binaries are found in a wide variety of environments and display an array of interesting characteristics.

I present strong evidence for the discovery of a new black hole X-ray binary in a globular cluster of a nearby elliptical galaxy. At the time of discovery it was only the second such system known. I also present the first X-ray spectroscopic analysis of a source found in the central region of the nearby starburst galaxy, M 82. This source is most likely a high mass X-ray binary system and displays peculiar X-ray characteristics relative to its behaviour at other wavelengths.

I study the temporal and spectroscopic behaviour of the first black hole binary found in a globular cluster. The spectra of this source show evidence for a strong, soft X-ray emission line.

I also study the global properties of X-ray binaries. I analyse the X-ray binary population of NGC 4472, a nearby elliptical galaxy. I compare these sources to those of other galaxies and also analyse the characteristics of subpopulations of X-ray binaries within the galaxy.

Contents

List of Figures

List of Tables

Academic Thesis: Declaration of Authorship

I, Tana Dale Joseph, declare that this thesis and the work presented in it are my own and has been generated by me as the result of my own original research.

A Study of X-ray Binaries in the Local Universe

I confirm that:

1. This work was done wholly or mainly while in candidature for a research degree at the University of Southampton.
2. Where any part of this thesis has previously been submitted for a degree or any other qualification at this University or any other institution, this has been clearly stated.
3. Where I have consulted the published work of others, this is always clearly attributed.
4. Where I have quoted from the work of others, the source is always given. With the exception of such quotations, this thesis is entirely my own work.
5. I have acknowledged all main sources of help.
6. Where the thesis is based on work done by myself jointly with others, I have made clear exactly what was done by others and what I have contributed myself.
7. Parts of this work have been published as:

   A Variable Black Hole X-ray Source in an NGC 1399 Globular Cluster, 2010, ApJ, Volume 721, pp. 323-328

   The unusual radio transient in M82: an SS 433 analogue?, 2011, MNRAS: Letters, 415, pp. 59-63

Signed: .....

Dated: .....

To 11 year-old Tana,
who decided we should go on this adventure.

Chapter 1

Introduction

1.1 Binary Stellar Systems

It is thought that as many as a third of stars in our Galaxy are part of a binary stellar system (Lada, 2006). Binary stars are two stars that orbit a common centre of mass. Sir William Herschel was the first to describe these systems as "binary" (Herschel, 1802). The binary systems in the Milky Way have been observed, catalogued and studied as far back as the late 1700s and early 1800s (see e.g. Herschel, 1803; Heintz, 1978; Soulie, 1997).

The study of binary stars and their evolution is of great interest and importance in astrophysical research because binaries are progenitors of phenomena like Type Ia supernovae (SN Ia), detectable black holes and millisecond pulsars. These systems, in turn, are fundamental diagnostic tools in such areas as cosmology, gravitational wave physics, general relativity and particle physics (through the neutron star equation of state). For instance, SN Ia are used as standard candles in cosmology, but the nature of their progenitors is still controversial. The chemical composition of the progenitor could affect how well the standard candle can be calibrated (e.g. Bravo et al., 2010). Despite the research that has gone into this field and its importance to astrophysics, binary stellar evolution remains very complicated and is still poorly understood.

X-ray binaries (XRBs) are binary systems that are luminous ($L_X > 10^{36}\,erg\,s^{-1}$) in the X-ray regime and consist of an accreting compact object (black hole or neutron star) and a donor star. These sources are particularly useful in the study of binary stellar systems because they can be observed at great distances. In fact, XRBs are the only class of binaries that are identifiable at all outside the Local Group, a small (radius $\sim 1\,Mpc$) cluster of about 50 nearby galaxies that includes the Milky Way (see e.g. van den Bergh, 2000; Irwin et al., 2007).

1.2 X-ray Binaries Revealed

Scorpius X-1 (Sco X-1), the first extrasolar X-ray source to be discovered, is an X-ray binary (Giacconi et al., 1962). At the time of discovery, however, it was not possible to know the nature of the source. After considering the X-ray and optical data for Sco X-1 it was concluded that the source must be a neutron star (NS) accreting gas from its binary companion (e.g. Shklovsky, 1967).

The systematic study of XRBs, as well as other astrophysical X-ray emission, became possible with the use of the *Einstein X-ray Observatory* (*Einstein*) (Giacconi et al., 1979). Launched in November 1978, it was the first fully imaging X-ray satellite telescope. This instrument boasted an angular resolution of tens of arcseconds (compared to the few arcminute resolution of the rocket borne telescopes at the time; see e.g. Gorenstein et al., 1978), a field of view of a few arcminutes, a sensitivity nearly 1000 times better than previous instruments and operated in the 0.3–4 keV range.

Prior to the *Einstein* era, the known number of X-ray binaries in the Local Group (excluding the roughly 60 XRBs in the Milky Way) stood at six; five sources in the Large Magellanic Cloud and one in the Small Magellanic Cloud (Helfand, 1984, and references therein). Using *Einstein*, over 100 XRBs or XRB candidates were found in 10 Local Group galaxies (Helfand, 1984), making it possible to compare XRB populations in different environments. For instance, it was found that Population I XRBs (now called high mass X-ray binaries; see § 1.4.1) were found preferentially in later type galaxies and Population II XRBs (now called low mass X-ray binaries; see § 1.4.2) in earlier types. This result was not thought to be simply due to the increasing number of massive stars in later type galaxies. It was also discovered that a significant number of XRBs were associated with globular clusters and that the clusters that hosted XRBs were brighter than average (e.g. Clark, 1975, ; see also § 1.4.2.2).

Einstein ushered in a new and exciting age in X-ray astronomy. The large two X-ray satellite telescopes that followed, the *Röntgen Satellite* (*ROSAT;* Truemper, 1982) and the *Advanced Satellite for Cosmology and Astrophysics* (*ASCA;* Tanaka et al., 1994) had instruments that were improvement on *Einstein*. For instance, *ASCA* had a much larger energy range (0.5–10 keV) and *ROSAT* had a much larger field of view (2°).

The *Chandra* X-ray observatory was launched in 1999 and formed part of NASA's Great Observatories programme (Weisskopf et al., 2000). This telescope has subarcsecond spatial resolution and an energy range of 0.1–10 keV. the *XMM-Newton* Observatory, launched later that same year, has a much coarser angular resolution ($\sim 15''$) than *Chandra*, but with an effective area three times as large (1500 cm^2 at 1 keV) (Lumb et al., 2012) and operates in a similar energy range (0.1–15 keV). Using

these telescopes, it is now possible to carry detailed studies of X-ray binaries, and other X-ray sources, in galaxies well outside the Local Group.

1.3 Accretion Physics in X-ray Binaries

1.3.1 The accretion disk

The accretion of material from the donor star to the compact object is what powers the enormous energy output of XRBs. Accreted material flowing from the donor star towards the compact object under the influence of gravity will have too much angular momentum to fall directly onto the compact object (Shakura & Sunyaev, 1973). Instead, the matter settles into a circular orbit around the compact object, since a circle is the orbit of lowest energy for a given angular momentum (e.g. King, 2003). Due to viscous processes within the accretion material, angular momentum and energy are transferred outwards (Shakura & Sunyaev, 1973). The accreted gas then spreads out into a disk of concentric annuli of matter following circular, Keplerian orbits.

The viscosity operating within the accretion disk is not due to the normal molecular interactions of matter. At present, the best model for this viscous process is the magneto-rotational instability model (see e.g. Krishan & Mahajan, 2008). In this model, the viscosity process are caused by the interactions of the matter with the weak, magnetic fields that thread the accretion disk.

As the gas loses kinetic energy and angular momentum, it moves deeper into the gravitational potential well of the compact object and gravitational energy is released. The proportion of rest mass energy released as radiation depends on the nature of the compact object (Pringle, 1981). In neutron stars, approximately 10 % of the rest mass energy of the accreted material can be released as radiation. For black holes (BHs), the proportion can be as high as 40 %.

1.3.1.1 Properties of the accretion disk

The structure of the accretion disk and its radiation output is mostly determined by the rate at which matter flows from the donor into the accretion disk and towards the compact object (see e.g. Shakura & Sunyaev, 1973). This accretion rate, $\dot{M}$, is related to the luminosity of the disk in the following way: $L = \eta \dot{M} c^2$, where η is the efficiency with which the gravitational energy is released as radiation and c is the speed of light.

At a certain critical value of accretion rate, $\dot{M}_{\rm crit}$, the disk luminosity is such that the force due to the radiation pressure on the electrons equals the gravitational force of the compact object on the protons (Shakura & Sunyaev, 1973). $\dot{M}_{\rm crit}$ is defined as $3 \times 10^8 \eta M/yr$, where M is the mass of the compact object. The resultant

luminosity is called the Eddington luminosity and is defined as $L_{Edd} = \frac{4\pi G M m_P c}{\sigma_T} = 1.3 \times 10^{38} \frac{M}{M_\odot} \,\mathrm{erg\,s^{-1}}$, where G is the gravitational constant, m_P is the mass of a proton, and σ_T is the Thompson scattering cross section of an electron. I note that the Eddington luminosity is determined under the assumption that the accretion disk consists of fully ionised pure hydrogen. Despite this, it is still used extensively to parametrise the luminosity of XRBs.

When $\dot{M} < \dot{M}_{crit}$, the radiative processes cool the disk sufficiently for it to be geometrically thin (but optically thick), such that the disk scale height, H$\ll$R, where R is the disk radius (see e.g. Shakura & Sunyaev, 1973; Pringle, 1981). The disk temperature profile in the thin disk is then: $T(R) = \left\{ \frac{3GM\dot{M}}{8\pi R^3 \sigma} \left[1 - \beta \left(\frac{R_{in}}{R} \right) \right] \right\}^{1/4}$, where R_{in} is the inner radius if the accretion disk, β is a dimensionless parameter determined by the boundary condition at R_{in} and σ is the Stefan-Boltzmann constant.

The smallest stable Keplerian circular orbit that the accretion disk can extend to around the compact object depends on the nature of the compact object (Shakura & Sunyaev, 1973). For a non-magnetic NS, the inner disk radius is equal to the surface of the star. For a magnetic NS, it is at the magnetospheric radius, i.e. the radius at which the magnetic pressure is equal to the ram pressure of the infalling accreting material. For a BH, this inner disk radius is called the innermost stable circular orbit (ISCO) and it is equal to 3 times the Schwarzschild radius ($= 2\frac{GM}{c^2}$). There are no stable orbits with radius smaller than the ISCO due to the general relativistic effects in the strong gravitational field of the BH.

Since the thin accretion disk rotates at approximately Keplerian velocities at each radius, half the energy in the disk has been converted into kinetic energy. The other half of the energy has been released as radiation. BHs do not have a solid surface. They are surrounded by an event horizon, an immaterial boundary that contains the region of spacetime that cannot communicate with the universe outside it (see e.g. McClintock & Remillard, 2006). The kinetic energy carried in the accretion disk is therefore lost once it passes the event horizon of the BH.

In the case where the compact object is a NS, the region where the accretion disk meets the star is called the boundary layer (see e.g. Popham & Sunyaev, 2001). If the NS is not rotating too quickly, most the kinetic energy in the accretion disk will be released in the boundary layer. The boundary layer is therefore hot ($> 10^8$ K). The soft photons from the disk are Compton up-scattered by the boundary layer and hard X-rays are produced. Therefore, given the same accretion rate, a NS XRB would be more luminous than a BHB.

1.3.1.2 The multicolour disk model

Mitsuda et al. (1984) showed that this geometrically thin, optically thick accretion disk can be well modelled as a superposition of blackbody spectra up to a maximum temperature that occurs near R_{in} (T_{in}), a so called "multicolour" disk (MCD). This model is a non-relativistic approximation of the thin accretion disk described above and does not take into account the effects of the strong gravitational field near the inner disk radius. Despite this, the MCD approximation to the thin disk of (Shakura & Sunyaev, 1973) is used widely to parametrise the spectra of XRBs. The disk luminosity is obtained by integrating the blackbody luminosity at each radial distance in the disk. The disk luminosity is then $L = 4\pi\sigma R_{in}^2 T_{in}^4$.

For BHs, we then have that $M \propto T_{in}^{-2} L^{1/2}$ (Feng & Soria, 2011, and references therein). Therefore, more massive BHs will have lower characteristic disk temperatures.

1.3.1.3 The disk instability model

Many XRBs display strong flux variability on time-scales ranging from days to weeks (see e.g. Yu & Yan, 2009). This variability is thought to be due to instabilities in the accretion disk caused by the changes in ionisation state of the accretion disk material (see e.g. Lasota, 2001; Frank et al., 2002, and references therein). For a range of accretion rates, the accretion disk is thought to exist in either a hot, highly ionised, high viscosity state or a cool, low viscosity, low ionisation state. The opacity of the disk is very sensitive to the ionisation state of the accretion disk material and thus disk temperature. Therefore, small changes in temperature cause the disk to change between the hot and cool states on very short timescales.

In order for the accretion disk to have a stable flow of matter through it, the accretion material must be fully ionised through out the disk. Such a stable flow will result in a persistently bright X-ray source.

The disk temperature must then sufficiently high to ensure that hydrogen is fully ionised, i.e. the disk temperature must greater than the ionisation temperature of hydrogen (6500 K) (see e.g. King, 2003). Since the disk temperature decreases with increasing disk radius, the condition for disk stability is that the outer disk temperature must then be greater than 6500 K.

Conversely, if the outer disk temperature is not greater than the ionisation temperature of hydrogen, the disk will contain regions of neutral hydrogen, which will quickly spread throughout the disk. The cool, neutral accretion matter does not flow as readily as ionised matter and the flow of matter towards the compact object is reduced. The decrease in $\dot{M}$ leads to a decrease in luminosity. The decrease in $\dot{M}$ also changes the nature of the accretion disk. In the next section (§ 1.3.1.4), I discuss the state of the accretion disk in the context of low and high accretion rates.

The changes in the accretion rate as described by the disk instability model, and the subsequent changes in accretion disk structure, lead to widely varying emission of radiation. In § 1.3.2 and § 1.3.3, I describe the salient XRB properties that arise due to accretion rate variations.

1.3.1.4 Deviation from the standard accretion disk model

At very low accretion rates ($< 0.01\dot{M}_{\rm crit}$), it is thought that the energy released from the accretion disk through viscous processes is then not radiated away efficiently as in a normal accretion disk that extends to the last stable Keplerian orbit. Instead the energy is stored inside the accretion material. The inner part of the accretion material then expands and becomes optically thin and geometrically thick and hot with electron temperature of $\sim 100\,\mathrm{keV}$. The inner radius of the accretion disk then recedes outward and the disk is truncated. The energy inside the hot, optically thin plasma is advected along with the plasma towards the compact object. Only a small portion of the energy is released before the accreting plasma reaches the compact object; the radiative efficiency of this accretion process is less than 1 %. This accretion flow is called an advection dominated accretion flow (ADAF) (see e.g. Narayan, 1996; Quataert & Narayan, 1999).

At supercritical accretion rates, the entire accretion disk can become both geometrically and optically thick. The temperature profile then changes from $\mathrm{T(R)}\propto\mathrm{R}^{-3/4}$ for a thin disk to $\mathrm{T(R)}\propto\mathrm{R}^{-1/2}$. This type of accretion disk is called a 'slim' disk (see e.g. Quataert & Narayan, 1999, and references therein; see also § 1.4.4.2).

1.3.2 Black hole binary emission states

It has long been known that black hole binaries (BHBs) transition between quasi-stable emission states in which either thermal or non-thermal emission dominates the X-ray spectrum, due to changes in the accretion rate, which can be explained by the disk instability model (see .e.g. Remillard & McClintock, 2006). In the following sections I will describe the canonical BHB X-ray emission states as well as the accretion flow and physical structures associated with them.

1.3.2.1 The quiescent state

Black hole binaries where the companion star has a low mass ($< 1\,\mathrm{M}\odot$; see § 1.4.2) spend the majority of their lifetime in a very low luminosity ($\mathrm{L}_X = 10^{30.5} - 10^{33.5}\,\mathrm{erg\,s^{-1}}$) state called the quiescent state (McClintock & Remillard, 2006). The accretion rate is very low in state ($< 0.01\dot{M}_{\rm crit}$; see e.g. Esin et al., 1997;

McClintock & Remillard, 2006) and the ADAF model is invoked to explain the low luminosity of the quiescent state as described in § 1.3.1.4.

The X-ray emission arising in the quiescent state is from soft photons from the accretion disk that have been Compton up-scattered by the corona of hot electrons that surrounds both the accretion disk and the ADAF. This gives rise to hard (up to 100 keV), non-thermal emission. This type of energy spectrum is well fit by a power law (PL) spectral model, defined as $F(E) \propto E^{-\Gamma}$, where F is the flux, E is the energy and Γ is the photon index. In the quiescent state, $1.7 \lesssim \Gamma \lesssim 2.1$ (e.g. McClintock & Remillard, 2006).

1.3.2.2 The thermal dominant state

The thermal-dominant state is defined as the emission state in which thermal emission contributes more than 75 % of the BHB flux (McClintock & Remillard, 2006). In this emission state, the accretion rate is thought to be $0.1 \lesssim \dot{M}/\dot{M}_{\rm crit} \lesssim 0.5$(Esin et al., 1997; McClintock & Remillard, 2006). The spectrum can be well modelled as a MCD, with $\mathrm{T_{in}} = 0.7 - 1.5$ keV. There is also sometimes a small contribution from a hard, non-thermal component, modelled by a steep PL component, $2.1 \lesssim \Gamma \lesssim 4.8$. The source displays only weak variability in this emission state. In this state the accretion disk is thought to be the canonical thin disk of Shakura & Sunyaev (1973).

1.3.2.3 The hard state

This emission state is characterised by hard, non-thermal emission. A PL spectrum in the 2–20 keV range accounts for at least 80 % of the emission, with $1.7 \lesssim \Gamma \lesssim 2.1$. There is also a small contribution to the emission from the soft X-rays that can be modelled as a cool disk component with $0.1 \lesssim \mathrm{T_{in}} \lesssim 0.2$ keV (McClintock & Remillard, 2006). Some BHBs also have an excess of photons in the 20–100 keV range, which has been interpreted as a reflection of the PL component by the inner accretion disk. Some regard the hard state as a less extreme version of the quiescent state (see e.g. Esin et al., 1997; McClintock & Remillard, 2006). The accretion rate is thought to be higher than in the quiescent state, but lower than in the thermal dominant state.

Detailed spectral analysis of the Galactic BHBs have revealed that the accretion disk appears to be truncated at some radius much larger than the ISCO, just as in the case for the quiescent state (McClintock & Remillard, 2006, and references therein). However, there is still much debate concerning the nature of the accretion flow inside the inner radius of the truncated disk. One possibility is that this region is filled by an ADAF. It is also thought that the inner region of the accretion disk is actually intact, but merely obscured by a Compton-scattering corona (see e.g. Esin et al., 2001; Frontera et al., 2003). There is also no consensus on the origin of the hard,

non-thermal emission in the hard state. For instance, the hard state X-ray spectrum of the Galactic BHB XTE J1118+480 has been fit with physical models that involve ADAF, synchrotron and thermal-Comptonisation processes (e.g. Esin et al., 2001; Markoff et al., 2001; Frontera et al., 2003).

The hard state is associated with the presence of compact, quasi-steady radio jets in BHBs (see e.g. Fender, 2006, and references therein). The jets emit radiation via the synchrotron process. These structures are seen to disappear when the BHB transitions from the hard state back to the thermal-dominant state. Thus there appears to be relationship between the nature of the accretion disk and the launching of jets in BHBs.

1.3.2.4 The steep power law state

In the steep PL state, the X-ray emission is non-thermal and the spectrum is well characterised by a power law model with photon index $\Gamma > 2.4$. The power law component contributes at least 20 % of the flux on this state (McClintock & Remillard, 2006, and references therein). The X-ray luminosity in this state is generally found to be $> 0.2\mathrm{L_{Edd}}$ and $\dot{M} \gtrsim 0.5\dot{M}_{\mathrm{crit}}$.

At present, it is not known which physical processes give rise the emission seen in the steep power law state. Inverse Compton scattering of disk photons by the energetic electrons of the corona is the process most often used to explain the steep power law emission (see e.g. Zdziarski et al., 2000; Titarchuk & Shrader, 2002). Alternatively, Yan & Wang (2011) present a model whereby photons are down scattered to produce the observed steep power law spectrum. In this model, the seed photons originate from synchrotron radiation produced by highly magnetised regions near the ISCO. These photons can reach energies higher than the MeV range. The high energy photons are then down scattered by the electrons in the corona to give the steep power law spectrum.

1.3.3 Neutron star binary emission states

The emission states of neutron star binaries are much less well-defined than those of BHBs. However, it was found that neutron star binaries with a low mass donor star ($< 1\,\mathrm{M_\odot}$; see § 1.4.2) and weak magnetic fields can be divided into two classes, 'Z' sources and atoll sources, based on their X-ray spectral behaviour (Hasinger & van der Klis, 1989). I will briefly discuss these classes below.

1.3.3.1 Z Sources

Z sources are so called because they trace out roughly Z shaped tracks in their X-ray colour-colour (CD) and hard-intensity (HID) diagrams on timescales of hours to days (Hasinger & van der Klis, 1989; van der Klis, 2004). These tracks are made up of three branches. The topmost branch in the CD/HID is the horizontal branch. Whether or not this branch is actually horizontal depends on the energy ranges of the hard and soft bands used to calculate the hardness ratio of the source. The normal branch is the middle branch. It is so named because it was thought that the source spent more time on this branch than the horizontal branch. The flaring branch is the bottom branch. It is named after the fact that Sco X-1 emits X-ray flares when it moves along this branch. Most other 'Z' sources also exhibit an increase in flux along this track, but several sources have been seen to become fainter when on the flaring branch. Z sources are luminous XRBs with $L_X =\sim 0.5- \sim 1\, L_{Edd}$.

1.3.3.2 Atoll sources

Atoll sources also trace out distinct shapes in their CD and HID over a period of hours to days (see e.g. Hasinger & van der Klis, 1989; van der Klis, 2004). These shapes are called the extreme island state, the island state and the banana branch. The extreme island state is associated with the lowest X-ray luminosity and hardest X-ray spectra. This state is similar to the hard state in BHBs (see § 1.3.2.3). The island state is associated with sightly softer spectra and higher luminosities. The source can remain in the island state for days to weeks at a time. Observational windowing can then lead to clusters of data points in the CD and HID when the source is in this state, which is why it is called the island state. The state with the highest luminosity and softest spectrum is the banana branch. The overall luminosity for an atoll source is $\sim 0.01 - 0.5\, L_{Edd}$.

1.3.3.3 The difference between Z and atoll sources

Apart from having widely varying tracks in their CDs and HIDs, atoll and Z sources also show disparity in other properties, such as luminosity, the rate at which they show thermonuclear X-ray bursts and even radio emission (see e.g. Homan et al., 2010, and references therein). These differences present an unresolved problem in the study of NS LMXBS. Several source characteristics have been put forward to explain these disparities, including mass accretion rates, magnetic field strengths and source viewing angle (see e.g. Hasinger & van der Klis, 1989; Psaltis et al., 1995; Kuulkers & van der Klis, 1995).

More recently, XTE J1701–462 was found to evolve from being a Z source to an atoll source (Homan et al., 2007b,c,a). Subsequent detailed analysis of XTE J1701–462 provided strong evidence that the wide variety of source properties seen between atoll and Z sources can be explained by changes in the mass accretion rate alone (Homan et al., 2010).

1.4 Types of X-ray Binaries

X-ray binaries can be classified into four main types: high mass X-ray binaries, low mass X-ray binaries, ultraluminous X-ray sources and supersoft X-ray sources. In the following sections I will define these systems and discuss their salient characteristics such as spectral and temporal properties.

I note that X-ray binaries with intermediate mass (IMXB) (1–10 $M_\odot$) companion stars do exist (e.g. van den Heuvel, 1975). Accretion onto the compact object in an IMXB proceeds via Roche lobe overflow (see § 1.4.1.2). However, due to the relatively high mass ratio between the compact object and donor star, this accretion phase proceeds very rapidly, lasting only a few thousand years (Tauris & van den Heuvel, 2006, and references therein). Thus these systems are not easily observed due to their short life times. IMXBs are not discussed further in this work.

1.4.1 High mass X-ray binaries

High mass X-ray binaries (HMXBs) are comprised of an accreting NS or BH and a massive ($> 10\,M_\odot$) giant or subgiant companion star. These companions were found to be O or B type main sequence progenitors. For HMXBs, $L_{opt}/L_X > 1$ (White et al., 1995; Tauris & van den Heuvel, 2006).

1.4.1.1 Properties of high mass X-ray binaries

It has long been known that HMXBs are associated with regions of recent star formation and young stellar populations (e.g. Giacconi & Gursky, 1974). Recent studies have served to confirm this association (e.g. Grimm et al., 2003; Mineo et al., 2012). HMXBs have hard spectra, with $kT \geq 15\,keV$ (Tauris & van den Heuvel, 2006).

A significant proportion of HMXBs were found to exhibit regular pulsations in the X-ray, with a wide range of pulsations periods ($< 1\,s$ to 20 minutes) (Liu et al., 2000). These pulsations are due to magnetically confined accretion onto the magnetic poles of the compact object and the misalignment of the rotational and magnetic axes. The pulsating systems require magnetic field strengths of at least $10^{11}\,G$ (Taam & van den Heuvel, 1986).

HMXBs can be divided into two categories: standard HMXBs and Be star X-ray binaries (Tauris & van den Heuvel, 2006, and references therein). The first type of HMXB has short orbital periods (≤ 10 days) and relatively low orbital eccentricity ($e < 0.1$). The companions are found to be supergiant O or B type stars. This class of HMXB can be further divided into wind-fed or Roche lobe overflow systems (see § 1.4.1.2) (Chaty, 2011).

These classic HMXB systems are persistent X-ray sources. The pulsating systems in this subgroup also have emission or absorption features in their X-ray spectra, thought to be due to cyclotron processes caused by their strong magnetic fields (B$\sim 5 \times 10^{12}$ G; Kirk & Trumper, 1983).

The second type of HMXBs have B-emission star (Be-star) companions (BeXRBs), wider orbits (P$\sim 10 - 350$ days) and higher eccentricity ($\lesssim 0.2 - 0.5$) than the previous class (see Maraschi et al., 1976). Be-star XRBs are highly variable, transient X-ray sources due to the eccentric orbit of the compact object (Tauris & van den Heuvel, 2006).

1.4.1.2 Formation of high mass X-ray binaries

High mass X-ray binaries are formed from the coevolution of two massive stars in a primordial binary ($> 12\,M_\odot$; Tauris & van den Heuvel, 2006). The more massive (primary) star evolves more quickly, going through successive phases of burning increasingly heavier elements in its core. After roughly 10^7 yr the primary star has evolved into a giant star with its envelope of hydrogen much larger than when it was a main sequence star. The envelope of the primary star then fills its Roche lobe. The Roche lobe is a surface of gravitational equipotential around the star that goes through the first Lagrangian point (see e.g. van den Heuvel, 1994). Matter from the hydrogen envelope of the more massive star will then flow though the first Lagrangian point and onto the less massive (secondary) star; this process is called Roche lobe overflow.

The secondary star is now much more massive than the primary, having acquired the hydrogen envelope of the primary star during Roche lobe overflow. The initially more massive primary star is now a helium star and is undergoing core nuclear burning of elements heavier than helium. After approximately 1.5×10^7 yr, the primary will have exhausted its nuclear fuel and develop a core of iron. The star then explodes as a supernova, leaving behind either a BH or NS.

In the case of the wind-fed supergiant HMXBs, the secondary is a O or B type star with a strong, dense, high velocity stellar wind (see e.g. Chaty, 2011). The secondary does not fill its Roche lobe. The orbit of the primary star is inside the stellar wind of its companion. The primary accretes the material from the secondary's steady stellar wind, resulting in a persistent X-ray source, with $L_X = 10^{35} - 10^{36}\,\mathrm{erg\,s^{-1}}$ (e.g.

Liu et al., 2006). For the other type of supergiant HMXB the secondary expands to fill its Roche lobe and mass transfer occurs via Roche lobe overflow, resulting in a much higher luminosity of $\sim 10^{38}\,\mathrm{erg\,s^{-1}}$; these sources are also persistent.

The Be-star binaries have eccentric orbits as a result of asymmetric supernova explosions (e.g. Verbunt & van den Heuvel, 1995). During the initial mass transfer from the primary to the secondary, the Be star is spun up to the point where a circumstellar disk of material is created around the primary star (Rappaport & van den Heuvel, 1982). Mass transfer onto the primary star then occurs at periastron, when the highly eccentric orbit of the primary takes it inside the circumstellar disk of the secondary.

1.4.2 Low mass X-ray binaries

A low mass X-ray binary (LMXB) consists of an accreting compact object with a low mass ($< 1\,\mathrm{M_\odot}$) companion (Tauris & van den Heuvel, 2006). These companion stars are faint and almost never observed, with $\mathrm{L_{opt}/L_X} \ll 0.1$ (White et al., 1995; Tauris & van den Heuvel, 2006).

1.4.2.1 Properties of low mass X-ray binaries

These systems have orbital periods of between 11 minutes to 17 days. When they are luminous, LMXBs have soft spectra, with $k_\mathrm{T} \leq 10\,\mathrm{keV}$. When the sources are fainter, the spectra can have hard power law tails that extend to 100–300 keV. As a consequence of their relatively weak magnetic fields ($10^{10} - 10^{11}$ G; e.g. Taam & van den Heuvel, 1986), very few LMXBs are observed to pulsate. LMXBs are associated with old stellar populations such a those found in elliptical galaxies, the Galactic bulge and globular clusters (Tauris & van den Heuvel, 2006). The GC-LMXB relationship is especially interesting because these clusters appear to be particularly efficient at forming LMXBs.

1.4.2.2 Low mass X-ray binaries in globular clusters

Globular clusters are gravitationally bound stellar clusters that orbit galaxies. They are compact systems with half light radii of a few parsecs, masses in the range $\sim 10^4 - 10^6\,\mathrm{M_\odot}$ and luminosities of M_V = -5 to -10 (Brodie & Strader, 2006). These clusters are comprised of $10^5 - 10^6$ very old ($\gtrsim 10\,\mathrm{Gyr}$) stars (e.g. Hut et al., 1992).

In the Milky Way, 10% of LMXBs reside in GCs (e.g. Liu et al., 2001, and references therein). Milky Way LMXBs are therefore at least two orders of magnitude more likely to be found in a GC than in the field of the Galaxy (see e.g. Verbunt, 2002). Elliptical galaxies have a higher fraction of their stellar mass in GCs (see e.g.

Rhode & Zepf, 2001), so we would expect their GC-LMXB fraction to higher. And indeed, it has been found that between 20% and 70% of LMXBs in well studied early type galaxies are found in GCs (see e.g. Angelini et al., 2001; Sarazin et al., 2001; Kundu et al., 2003; Kim et al., 2009).

Globular clusters have a bimodal optical colour distribution (e.g. Zepf & Ashman, 1993; Rhode & Zepf, 2001; Jordán et al., 2009) due mainly to a difference in metallicity between two GC subpopulations (Brodie & Strader, 2006, and references therein). LMXBs are over three times as likely to reside in metal rich (red, and/or younger) GCs rather than in metal poor (blue and/or older) GCs (e.g. Kundu et al., 2002; Kim et al., 2006b, 2009; Voss et al., 2009). This effect could be due to the age or metallicity of the GCs and is still a matter of debate.

The idea that there is a relationship between the number density of LMXBs and the metallicity of GCs has been touted for decades (e.g. Silk & Arons, 1975; Grindlay, 1987). It was found that GCs with higher metallicity had flatter initial mass functions, which would lead them to form neutron stars at a higher rate than clusters with steeper initial mass functions and hence they would be more likely to host a LMXB. Kundu et al. (2003) also found that metallicity rather than age was the reason LMXB were more likely to reside in red GCs. They studied the GC systems of two elliptical galaxies, NGC 4365 and NGC 3115. The younger GC population of NGC 4365 did not provide evidence of an increased LMXB formation rate compared to the older GC population of NGC 3115. In contrast, NGC 3115 has two GC subpopulations that are the same age, but have different metallicities. It was found that the red, metal rich GC subpopulation was more than three times more efficient at producing LMXBs than the blue, metal poor subpopulation. Maccarone et al. (2004) suggested that the low metallicity subpopulations would have strong stellar winds due to inefficient line cooling. These winds would cause the LMXBs in the clusters to evolve faster and thus decrease the number of observed LMXBs in metal poor GCs.

On the other hand, evidence also exits that increased incidence of LMXBs in red GCs is due to dynamical effects. Jordán et al. (2004) find that the probability that a GC will host a LMXB is dependent on the dynamical processes, such as the rate of neutron-star binary exchanges, within the cluster rather than metallicity. This result is in keeping with the outcomes of dynamical simulations of formation of LMXBs in GCs (Ivanova et al., 2005). Kim et al. (2006b) found that smaller galactocentric radius increased the chances that a GC would host a LMXB. They put forward the idea that GCs closer to the galactic centre would need to have denser cores and be more compact so as not to be tidally disrupted. These properties would then increase the likelihood of dynamical LMXB formation processes. Ivanova et al. (2012) also put forward the idea that the metallicity dependence is due to a difference in stellar content of the red and blue GCs. The stars that constitute red GCs are more likely to be involved in dynamical processes that lead to the production of LMXBs.

1.4.2.3 Formation of low mass X-ray binaries

Low mass X-ray binaries outside of globular clusters, i.e. in the field of the host galaxy, are formed by the evolution of a binary system with a mass discrepancy (Tauris & van den Heuvel, 2006). The initial masses for the primary and secondary stars are $> 10\,\mathrm{M}_\odot$ and $< 2\,\mathrm{M}_\odot$ respectively. Consequently, the primary evolves much more quickly than the secondary. After approximately 10^7 yr, the primary has evolved to fill its Roche lobe (Kalogera & Webbink, 1998). At this stage, the secondary star is still very close to the zero age main sequence. Mass transfer to the secondary then proceeds via Roche lobe overflow.

The mass transfer disturbs the thermal equilibrium of the secondary. The timescale on which a star can return to thermal equilibrium, the thermal timescale, is dependent on its mass ($\tau_{\mathrm{th}} =\sim 30(M/M_\odot)^{-2}$ Myr; Tauris & van den Heuvel, 2006). However, the mass transfer timescale is determined by the thermal timescale of the primary. Thus, the secondary returns to thermal equilibrium on a time scale much longer than the mass transfer timescale. The accreted material then cannot cool as it is transferred to the secondary, causing the secondary to expand and fill its Roche lobe. The outer envelopes of the two stars then come into contact and form a common envelope (Kalogera & Webbink, 1998).

The secondary experiences a frictional drag force as it moves inside the common envelope and so it spirals in towards the primary. The orbital energy of the secondary is deposited in the common envelope, causing it to expand and become unbound from the binary system. The primary has lost all of its envelope and a helium star remains. The secondary remains mostly intact. The orbital separation of the binary is much smaller than before the common envelope phase.

The primary continues to undergo core nuclear burning until it develops an iron core and explodes as a supernova, resulting in a BH or NS. The secondary has continued to follow normal stellar evolution after the common envelope phase and it eventually evolves to fill its Roche lobe. At this point, mass transfer to the primary occurs via Roche lobe overflow, creating an X-ray source.

LMXBs in globular clusters are not thought to be the result of the evolution of primordial binaries as described above. Instead they are thought to be formed by various dynamical processes within the dense stellar environment of the globular cluster (e.g. Clark, 1975, and references therein). These processes include the dissipative tidal capture of a low mass star by a compact object (Clark, 1975; Fabian et al., 1975), exchange interactions whereby the compact object interacts with a binary and ejects and replaces one of the original binary stars (Hills, 1976) and direct collisions between compact objects and red giant stars (Verbunt, 1987).

1.4.3 Supersoft X-ray sources

Long et al. (1981), using the *Einstein* telescope, were the first to observe supersoft X-ray sources (SSS). These sources are thought to be white dwarfs undergoing steady surface nuclear burning of hydrogen accreted from low mass ($\sim$1–2.5 $M_\odot$) donors (van den Heuvel et al., 1992; Kahabka & van den Heuvel, 1997). These systems are able to maintain steady nuclear burning due to the rapid, thermal time scale mass transfer from the Roche lobe overflow of the donor star.

SSS have very soft blackbody spectra that peak in the energy range 15–80 eV and bolometric luminosities of between 10^{36} and 10^{38} erg s^{-1} (Kahabka & van den Heuvel, 1997, and references therein). SSS are considered to be good candidates for the progenitors of Type Ia supernovae (e.g. Branch et al., 1995; Hachisu et al., 2010).

Other types of SSS were later revealed by *Chandra* and *XMM*. These sources have harder spectra characterised by blackbody spectra with energies of 0.1–0.3 keV (e.g. Di Stefano & Kong, 2003, 2004), the aforementioned SSS spectrum with an additional hard component or have $L_X > 10^{37}$ erg s^{-1} (e.g. Di Stefano et al., 2004). These new populations of soft sources are not thought to be comprised of a single type of binary system. Instead they could be explained by a variety of sources, including BH and NS binaries.

1.4.4 Ultraluminous X-ray sources

An ultraluminous X-ray source (ULX) is a non-nuclear mass accreting BH with peak, apparent (i.e. assumed isotropic) X-ray luminosity, $L_X 10^{39}$ erg s^{-1}, roughly the Eddington luminosity for a 10 $M_\odot$ BH (Feng & Soria, 2011). Such sources were first observed using the *Einstein* telescope (Long & van Speybroeck, 1983). Later surveys showed that ULXs are strongly associated with regions of star formation (e.g. Roberts et al., 2002; Humphrey et al., 2003; Swartz et al., 2004; Liu & Bregman, 2005; Liu & Mirabel, 2005).

1.4.4.1 Spectral properties of ultraluminous X-ray sources

ULXs exhibit a range of often conflicting spectral properties. Initial analysis of ULXs showed that their spectra could be well fit by the same spectral model used on Galactic BHBs, i.e. a continuum model consisting of a multi-colour disk plus a harder power law component (e.g. Miller et al., 2003, 2004; Jenkins et al., 2005; Roberts et al., 2005). Using this model, the spectra were shown to have disk temperatures kT = 0.1–0.3 keV and power law slopes (Γ = 1.6–2.5) (Stobbart et al., 2006) as compared to $kT \sim 1$ keV and power law slopes Γ = 2.1–4.8 for Galactic BHBs (e.g. McClintock & Remillard, 2006).

However, this model was not the only one that could produce acceptable fits to ULX spectra. A model where the soft end of the spectrum is fit by a power law and the disk component fits the harder energies was found to give a much better fit to several of the ULX spectra studied (Stobbart et al., 2006). The disk temperatures were higher ($kT = 0.9$–2.7 keV) and the power law steeper ($\Gamma = 2.5$–4.3) than the previous model. This new model also revealed a spectral break or curvature above 2 keV. This spectral feature was found to exist in other ULXs as well (Okajima et al., 2006; Dewangan et al., 2006). The spectral break implies that the corona near the black holes in ULXs are optically thick, in contrast to the optically thin coronae of Galactic BHBs (Roberts, 2007, and references therein). Gladstone et al. (2009) carried out further detailed spectral analysis on ULXs. They suggest that the optically thick corona plus disk model implies that ULXs are in an ultraluminous emission state in which the accretion rate is super-Eddington.

Kubota et al. (2004) showed that a model comprised of a multi-colour disk and a Compton scattering component gives good fits to some ULX spectra as well. In this scenario, the disk photons undergo inverse Compton scattering by energetic electrons. These high energy electrons are thought to originate when the inner region of the accretion disk becomes unstable during periods when the accretion rate is very high. Thus this cloud of energetic electrons is probably confined to the inner region of the disk (see e.g. Kubota et al., 2001; Kobayashi et al., 2003).

The spectral variability of ULXs has not been studied in great detail, although the systems that been investigated display two distinct types of variability. Some ULXs exhibit the same behaviour as Galactic BHBs in that their spectra become softer with increasing luminosity. Other sources have shown the opposite trend: the spectra harden as the source brightens (e.g. Dewangan et al., 2004; Jenkins et al., 2004; Feng & Kaaret, 2006; Soria et al., 2007; Roberts et al., 2012). This unusual spectral behaviour could be caused by a system with a cool, optically thick accretion disk and a optically thick corona where the corona heats up as the ULX becomes more luminous (Roberts et al., 2006).

This wide variety of X-ray properties would imply that the ULX population is a heterogeneous group of sources. Indeed, several ideas have been put forward to address the seemingly diverse nature of ULXs.

1.4.4.2 The nature of ultraluminous X-ray sources

ULXs are found predominantly in region of recent or active star-formation. Thus it has been suggested that ULXs in late type galaxies are a type of HMXB (e.g. Rappaport et al., 2005). It is thought that the ULXs that do reside in early type galaxies are LMXBs (Humphrey et al., 2003; Colbert et al., 2004).

Some believe that some ULXs, especially those with $L_X > 10^{41}\,erg\,s^{-1}$, could be BHB systems in which the BH has a mass of roughly 100–$10^4\,M_\odot$ (e.g. Colbert & Mushotzky, 1999; Miller, 2005). These massive black holes could be formed by the collapse of dense stellar clusters (e.g. Gürkan et al., 2004), Population III stars in the early universe (e.g. Heger & Woosley, 2002) or the merging of stellar mass BHs (e.g. Lee, 1995). Black holes in this mass range, called intermediate mass black holes (IMBHs), would easily explain the high X-ray luminosities observed. The low inner disk temperatures derived from the spectral analysis favours the IMBH scenario, as the inner disk temperature scales inversely with the mass of the BH ($T \propto M^{-0.25}$; see e.g. Miller et al., 2003; Roberts, 2007). The best candidate for such a system is HLX-1 in ESO 243-49, with $L_X \sim 10^{42}\,erg\,s^{-1}$ (Farrell et al., 2009).

Another school of thought maintains that the majority of ULXs are in fact stellar mass BHBs in which the X-ray emission enhanced by processes such as beaming (e.g. King et al., 2001; Körding et al., 2002), super-Eddington emission from a non-standard accretion disk (e.g. Begelman, 2002; Ebisawa et al., 2003) or a combination of the two (Poutanen et al., 2007; King, 2009).

The geometric beaming scenario put forward by King et al. (2001) states that the X-ray emission from a stellar mass BHB is not isotropic, but rather the emission escapes the system from only a small area, leading to large apparent luminosity if the source is viewed along the line of sight of the emission region. They propose that easiest way to achieve this beaming is an accretion disk with decreased optical depth over some small area and the X-rays would then preferentially escape in the direction of the low optical depth. They suggest that this beamed emission scenario is a short lived phase of all stellar mass BHBs.

Markoff et al. (2001) first suggested that the jet emission from stellar mass BHBs could be contributing to X-ray emission seen from these sources. This implies that some of these systems could be relativistically beamed, which would lead to an overestimate of the source luminosity if isotropic emission is assumed. Subsequently, Körding et al. (2002) compared the relativistically beamed model with the IMBH scenario and found that either of these could reproduce the X-ray luminosity functions of their sample of X-ray binaries in three nearby galaxies. They showed that the jets would require Lorentz factors of roughly five and that between 10% and 30% of the soft X-ray emission would have to come from the jets in order to account for the observed X-ray luminosity functions. However, this and other similar relativistic beaming models (Fabrika & Mescheryakov, 2001; Begelman et al., 2006) were subsequently shown to be implausible as they predicted a higher number of low luminosity ULXs than the observational data can account for (Davis & Mushotzky, 2004).

Begelman (2002) put forward a model whereby the super-Eddington luminosity is generated in the inner part of a geometrically thin, radiation pressure dominated

accretion disk around a stellar mass black hole. Such disks are predicted to develop small scale density inhomogeneities in which the transfer of energy is increased and photons can escape more easily. They predict this effect could lead to the emission from the inner region of the disk reaching approximately 10 times the Eddington limit of the black hole.

The 'slim' accretion disk model can also account for the super-Eddington luminosities seen in ULXs (Ebisawa et al., 2003, and references therein; see also § 1.3.1.4). For the slim disk case, the luminosity of the disk $L_{disk} \approx 10 L_{Edd} \left(\frac{h}{R}\right)$, where h is the half thickness of the disk. For a slim disk, $\frac{h}{R} \approx 1$, thus L_{disk} exceeds the Eddington limit for the BH in the system by a factor of ten.

Poutanen et al. (2007) and King (2009) explain the high X-ray luminosity of ULXs using a combination of the beaming and super-Eddington emission models. For super-Eddington accretion rates the inner region of the accretion disk becomes geometrically thick and has a strong outflow, resulting in $L_{disk} \sim L_{Edd}\,(1 + \ln(\dot{m}))$, where $\dot{m}$ is the accretion rate normalised to the Eddington accretion rate, $\dot{M}_{Edd}$. The strong outflow also serves to confine the outgoing radiation from the disk to a cone shape on either side of the disk. The apparent luminosity of the source is then $L \sim \frac{L_{Edd}}{b}\,(1 + \ln(\dot{m}))$, where b is the beaming factor, defined as $\Omega/4\pi$ and Ω is the solid angle of the emission (see King et al., 2001). King (2009) showed that $b \sim 70/\dot{m}^2$. Thus accretion rates of $10 \lesssim \dot{m} \lesssim 30$ would account for most ULXs with $L_X \lesssim 10^{41}\,\mathrm{erg\,s^{-1}}$.

High mass stellar BHs ($\sim 30 - 90 M_\odot$) also provide a viable alternative for the nature of the BHs in ULXs (e.g. Zampieri & Roberts, 2009). These massive stellar remnant BHs are formed in the collapse of low metallicity stars with masses $> 40\,M_\odot$. BHs in this mass range would easily explain ULXs where $L_X \lesssim 10^{40}\,\mathrm{erg\,s^{-1}}$ without having to invoke high beaming factors or strongly super-Eddington accretion.

I note that the spectral properties discussed here are for ULXs in star forming galaxies only. Due to the lack of recent star formation in early type galaxies, they are not expected to have significant populations of ULXs (Fabbiano, 2006, and references therein). However, the two ULXs discussed in chapters § 4 and § 5 reside in globular clusters.

1.5 X-ray Sources in the Milky Way and Nearby Galaxies

Over 200 HMXBs have been observed in the Galaxy (Coleiro & Chaty, 2013). The majority of these HMXBs are located in the Galactic plane (Grimm et al., 2002). Most (∼60%) HMXBs in the Galaxy are found to be BeXRBs (Liu et al., 2006). The Magellanic Clouds are known to contain over 100 HMXBs (Liu et al., 2005). Mineo

et al. (2012) have collated data for 29 star-forming galaxies within 40 Mpc. They find that these galaxies contain over 700 HMXBs.

The size of HMXB populations scale with star formation rate (SFR), thus HMXBs are good tracers of star formation rate within star-forming galaxies (e.g. Grimm et al., 2003). Mineo et al. (2012) showed that the X-ray luminosity of the HMXB populations scales with SFR as $L_X(\mathrm{erg\,s^{-1}}) = 2.6 \times 10^{39}\,\mathrm{SFR}\ (M_\odot/\mathrm{yr})$, in good agreement with the results of Grimm et al. (2003).

There are more than 180 LMXBs in the Milky Way and Magellanic Clouds alone (Liu et al., 2007). Tens to hundreds of LMXBs have been detected in galaxies outside the Local Group (see e.g. Fabbiano & White, 2006).

For nearby (< 25 Mpc) galaxies of various morphological types and spanning a stellar mass range, $\log(M_\star) = \sim 9 - 11.5$, Gilfanov (2004) found that the combined X-ray luminosity of the LMXB population of a galaxy scaled directly with the mass of the galaxy. LMXB populations are therefore good tracers of stellar mass of the host galaxy, rather than SFR.

Walton et al. (2011) used the X-ray data from the 2*XMM* Serendipitous Survey and the RC3 galaxy catalogue (see Watson et al., 2009) to search for ULXs in nearby galaxies. They found 470 ULXs, 367 of which were not listed in previous catalogues. Similarly, Liu (2011) used archival *Chandra* data to search for ULXs in galaxies within 40 Mpc and found 342 sources.

Using the *XMM* sample of ULXs, Walton et al. (2011) find that ULXs in elliptical galaxies trace the stellar mass of the host galaxies, in keeping with the idea that ULXs in these galaxies are LMXBs (Humphrey et al., 2003; Colbert et al., 2004; Gilfanov, 2004). In spiral galaxies, the number of ULXs per unit galaxy mass was found to decrease with increasing galaxy mass, consistent with the work of Swartz et al. (2008). SFR per unit galaxy mass also decreases with increasing spiral galaxy mass (e.g. Brinchmann et al., 2004). Thus ULXs in spirals appear to be tracing SFR, supporting the scenario that ULXs in early type galaxies are HMXBs (Grimm et al., 2003; Rappaport et al., 2005; Mineo et al., 2012).

More than 100 SSS have been observed in nearby (< 20 Mpc) galaxies of different morphological types, including nine in the Milky Way (Kahabka, 2006, and references therein). These systems are distributed throughout the halo, disk and bulge of their host galaxy. SSS found in the disks of galaxies are associated with a younger stellar population. Those SSS in the bulges and halos are associated with older stellar populations.

1.6 Thesis Outline

In § 2, I discuss the X-ray analysis of an intriguing radio transient source discovered in the central region of M 82, a nearby starburst galaxy. In § 3 I present the results of a study of the X-ray point source population of NGC 4472, a nearby elliptical galaxy, using deep *Chandra* observations. The outcome of the investigation into the spectral and temporal properties of XMMU 122939.7+075333, the first BH to be discovered in a globular cluster, are detailed in § 4. § 5 deals with the discovery of another BH in a globular cluster, this time in NGC 1399. Lastly, in § 6, I put forward my concluding remarks and discuss further plans for future work.

Chapter 2

The unusual radio transient in M 82: an SS 433 analogue?

2.1 Introduction

M 82 is prolific star-forming galaxy at a distance of 3.6 Mpc (Freedman et al., 1994). Its proximity therefore makes it an ideal place to study star formation. To this end, M 82 has been well monitored by various observatories at several wavelengths for decades (e.g. Telesco & Harper, 1980; Kronberg et al., 1981; Bland & Tully, 1988; Muxlow et al., 1994; Strickland et al., 1997; Weiß et al., 2001; Fenech et al., 2008). In particular, radio observations have revealed approximately 60 compact radio sources in the central region of M 82 (McDonald et al., 2002). A quarter of these sources are of unknown origin. In addition to compact sources, frequent radio observations have also found transient sources of an undetermined nature in M 82 (Kronberg & Sramek, 1985; Muxlow et al., 1994) and monitored the evolution of radio supernovae (e.g. Muxlow et al., 1994; Beswick et al., 2006; Fenech et al., 2008).

The next generation of radio telescopes should reveal many more such transient sources. These observatories will have the ability to detect a 0.1 mJy source within minutes. We will then more easily be able to observe transient populations not only in star-forming galaxies like M 82 where these systems are abundant, but also in galaxies with low star-formation rates like ellipticals. By attempting to determine the nature of the unknown transients such as those in M 82, we will make the task of studying the large number of transients expected to be observed in the future much easier.

In this chapter we investigate further the most recently discovered radio transient of unknown origin in M 82 and show that this source is unlikely to be a normal microquasar (an X-ray binary with relativistic jets). We discuss the possibility that the M 82 source could be an extragalactic analogue of SS 433, a very unusual

Galactic microquasar (Margon, 1984, and references therein). Both sources have low X-ray and high radio luminosities. If the M 82 transient is an extragalactic SS 433 like microquasar, it will be only the second such source, after the microquasar S 26 in NGC 7793, to be discovered (Pakull et al., 2010).

2.2 Properties of the source

The radio source was first discovered with the Multi-Element Radio-Linked Interferometer Network (MERLIN) early in May 2009 by Muxlow et al. (2009) as part of a continuous monitoring of the recent supernova SN 2008iz in M 82. Brunthaler et al. (2009) later also reported a detection of the source on 2009 April 30 with the Very Long Baseline Array (VLBA).

For the last 15 to 20 years M 82 has been observed at radio frequencies at intervals of six months to one year. In that time, only two other transient sources of unknown nature have been detected in the galaxy (Kronberg & Sramek, 1985; Muxlow et al., 1994). This most recent transient source was not detected by Muxlow et al. (2009) in the period 2009 April 24th to 27th to a $3\,\sigma$ upper limit of < 0.2 mJy/ beam at 4.9 GHz. Brunthaler et al. (2009) found that the source was not detected in their observations taken on 2009 April 8 ($3\,\sigma$ limit of 0.6 mJy at 22 GHz) and 2009 April 27 ($3\,\sigma$ limit of 0.9 mJy at 43 GHz and 0.7 mJy at 22 GHz). Moreover, Muxlow et al. (2010) report that the source has not been detected in other wavebands previously or concurrently with their radio detections, including infrared (Fraser et al., 2009), optical (Matilla, private communication) and X-ray observations (Kong & Chiang, 2009).

The source is situated in the nuclear region of the galaxy, at a position of RA $09^h55^m52^s.5083$, Dec. $69°40'45''.410$ (J2000) with 5 mas error in each coordinate. The VLBA observations show flux densities of 1.1 mJy and 0.5 mJy at 1.6 GHz and 4.8 GHz respectively. The observations from the first week of 2009 May revealed a peak radio flux of between 0.6 and 0.7 mJy at 4.9 GHz. Follow up observations showed that the flux remained roughly constant over the next 150 days (Muxlow et al., 2010) (see Fig. 2.1). The radio spectral index, α, also remained unchanged at -0.7 during this time, where $F_\nu \propto \nu^\alpha$. MERLIN data taken in 2010 January (over 240 days after the initial detection) show that the source is roughly 15 mas in size. This implies a physical size of approximately 0.3 pc, less than an order of magnitude bigger than the extent of the radio jets of SS 433 ($\sim$0.05 pc; Paragi et al., 2001).

2.3 X-ray Observations and Analysis

The nucleus of M 82 was observed with Chandra ACIS-S on 2009 April 17 (Obs ID 10025) and 2009 April 29 (Obs ID 10026). For transient sources, the peak X-ray

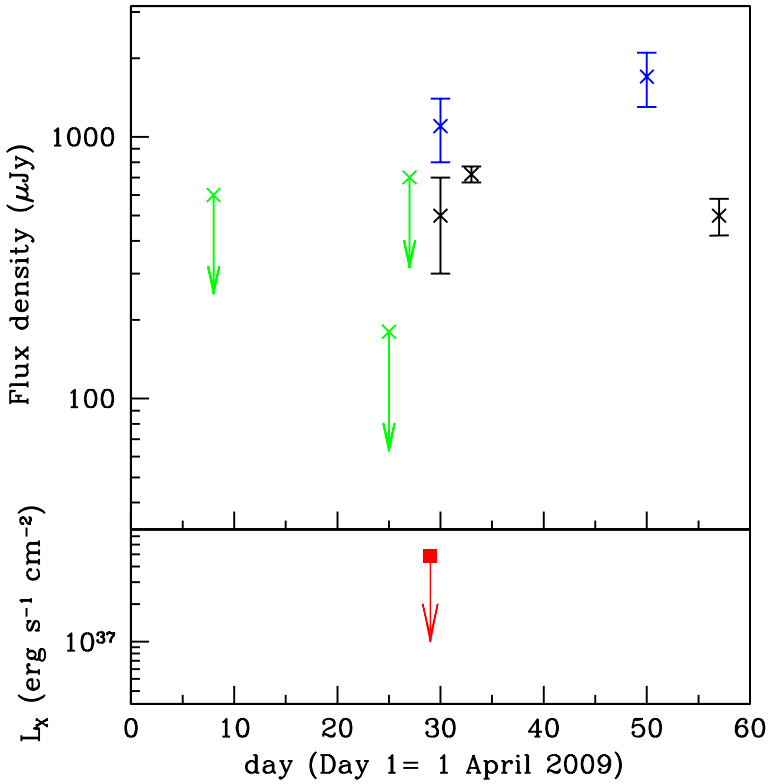

FIGURE 2.1: A light curve for the M 82 transient showing radio and X-ray data from April and May 2009. The top panel shows the radio data for the source. The blue, black and green symbols indicate data taken at 1.6, 4.9 and 22 GHz respectively. The bottom panel shows the X-ray luminosity upper limit for the source estimated from Obs ID 10026.

emission usually occurs a few days before that of the radio emission (see e.g. Hjellming & Rupen, 1995; Kuulkers et al., 1999; Rodriguez et al., 2008, and references therein). The source was detected in radio on 30 April and reached its peak a few days later. We therefore expect that the source should already be visible in X-rays in the days before the radio peak flux occurred. Thus an X-ray observation of the source taken on 29 April could well detect the source near or at its peak X-ray flux. The date of Obs ID 10026 are shown in relation to the radio observations in Fig. 2.1.

The data files were downloaded from the Chandra on-line archive. The data were checked for background flares and spectra were produced using the CIAO script *psextract*. We used a circular region of radius 2″ centred on the radio source to extract the source and background spectra from Obs ID 10026 and 10025 respectively. The X-ray images, including the position of the source, are shown in Fig. 2.2.

The spectra were analysed using the Interactive Spectral Interpretation System (ISIS), version 1.6.1. As Obs ID 10025 was taken well before the source was first seen in radio, we used this observation as the background spectrum for our analysis. Given the initial, sharp radio variability, we expect that the variable component of the X-ray

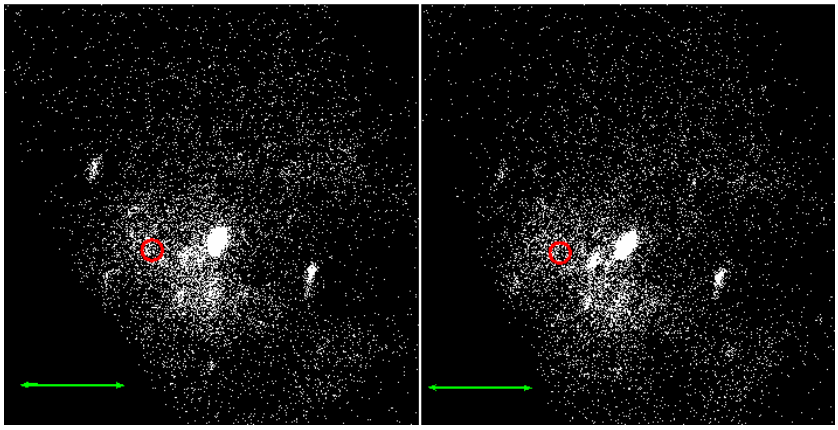

FIGURE 2.2: The X-ray images for Obs ID 10025 (left panel) and 10026 (right panel) showing the central region of M 82. The images includes data in the 0.3–10 keV range. The red circle indicates the position of the source. The green line is 20″ long.

flux should be comparable to the X-ray flux itself. We were unable to use the standard detection experiment approach because of the strong diffuse X-ray emission in the centre of M 82. The data were grouped into bins of 50 counts to increase signal-to-noise; binning to the standard signal-to-noise ratio of 5 produced too few bins for fitting. Only data in the range 0.3−10 keV were included in the spectral fitting. Due to the low number of counts only two spectral models were used, namely disk blackbody (diskBB) and power law (PL) (see Mitsuda et al., 1989). We fixed the PL index, $\Gamma = 2$ and the diskBB temperature, $T_{in} = 1$ keV. The Gehrels statistic was used to calculate errors as it gives a more reliable fit to data with low count rates (Gehrels, 1986). Both the diskBB and PL models give similar results.

The spectral fitting of the data yielded no clear detection of significant X-ray flux. In fact, the background spectrum had a higher number of counts than the source spectrum. We calculated the upper limits corresponding to a 99 % confidence level for the X-ray luminosity and found that the unabsorbed luminosities are $1.8{\times}10^{37}$ erg s^{-1} and $1.5{\times}10^{37}$ erg s^{-1} for PL and diskBB respectively, using Galactic column density, $n_H = 4 \times 10^{20}$ cm^{-2} (Dickey & Lockman, 1990). The spectral fit for the 99 % confidence level limit of the PL model is shown in Fig. 2.3. The data are in the range 0.3−10 keV. The bottom panel shows the $\Delta\chi^2$ value from each bin.

The source is situated at a local minimum in foreground column density with a value of $3.5{\times}10^{22}$ cm^{-2} estimated from CO maps (Walter et al., 2002). Using this measured column density, the upper limits corresponding to a 99 % confidence level for $L_{\rm X}$ in the $0.3 - 10$ keV range is $4.9{\times}10^{37}$ erg s^{-1} (PL) and $3.1{\times}10^{37}$ erg s^{-1} (diskBB). The X-ray non-detection is therefore unlikely to be caused by absorption in M 82.

2.4 Properties of Galactic black hole binaries

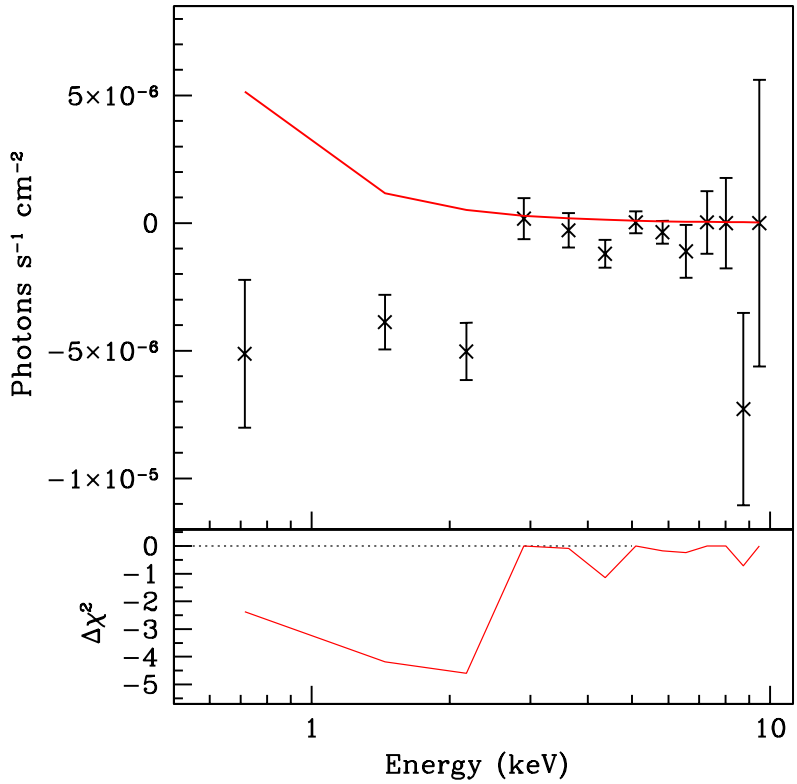

FIGURE 2.3: The PL model fit (99 % confidence level upper limit) of X-ray (0.3−10 keV) data for the M 82 source. The $\Delta\chi^2$ contributions from each bin are shown in the bottom panel, with the sign indicating when the data are above or below the model.

Muxlow et al. (2010) discuss various possibilities regarding the nature of the source, including that the source is an extragalactic microquasar. Other ideas put forward are that the source might be an AGN in the centre of M 82 or an unusual radio supernova. However, they also note that both these explanations are unlikely. If the source is an AGN it would require the supermassive black hole to be significantly displaced from the dynamical centre of the galaxy. The source is also too faint to be a Type I supernova and the unchanging spectral index argues against young radio supernovae in general.

In this work we focus on the microquasar scenario. We use the properties of black hole binaries (BHBs) to predict various parameters, such as X-ray luminosity, for our source.

An unambiguous correlation has been found between X-ray luminosity, $L_{\rm X}$, and radio luminosity, $L_{\rm radio}$, for stellar mass black holes in the hard X-ray state (always the case below 1% Eddington), of the form $L_{\rm radio} \propto L_{\rm X}^{b}$ where $0.6 \leq b \leq 0.7$ (Corbel et al., 2003; Gallo et al., 2003, 2006). At higher Eddington ratios, X-ray binaries can enter phases of radio flaring associated with state transitions. As discussed in Fender et al. (2004) (see for example their Fig. 2), in such states the radio/X-ray correlation is still

broadly consistent with the data, albeit with a larger scatter (of around 1 dex in $L_{\rm radio}$, corresponding to a scatter in $L_{\rm X}$ of ~ 1.4 dex).

This radio/X-ray correlation has been shown to extend, with the addition of a mass term, M, to active galactic nuclei (AGN), in a tight correlation for AGN at low Eddington ratios (Falcke et al., 2004), and with a similar correlation but broader scatter when including a sample of AGN with no restriction on Eddington ratio or state, and which thus must include flaring sources (Merloni et al., 2003). The best fit to the Merloni et al. (2003) 'fundamental plane' is of the form $L_{\rm radio} \propto L_{\rm X}^{0.6} M^{0.8}$, and has a scatter of about 2 dex in $L_{\rm radio}$. The current state of knowledge is, therefore, that for 'normal' X-ray binaries and AGN there is a common radio/X-ray correlation which is tighter in hard states but which follows a similar, but less precise, correlation even in flaring states. There are of course additional caveats if the radio observations are very sparse (e.g. whether or not the flare peak was caught), but in the case of the M82 transient the sampling is good.

Assuming that the M 82 source is a normal BH X-ray binary transient following the hard state Corbel/Gallo relations, we can estimate its associated X-ray luminosity. We use the peak flux density of 0.7 mJy at 4.9 GHz ($\rm L_{radio} = 5.3 \times 10^{34}\,erg\,s^{-1}$) to calculate the X-ray luminosity as the source remained at that brightness for an extended period of time. The measured radio luminosity implies $L_{\rm X} \sim 6 \times 10^{42}$ erg $\rm s^{-1}$, far in excess of our established upper limit (see Fig. 2.5).

The Merloni et al. (2003) fundamental plane can also be used to estimate the X-ray luminosity of the source. As mentioned previously, in the case of the fundamental plane, the source does not have to be in the hard state for the relation to hold. If we now assume that the source is in some high luminosity state where $L_{\rm X} = L_{\rm Edd} = 1.3 \times 10^{38} (M/M_{\odot})\,\rm erg\,s^{-1}$ and again using $\rm L_{radio} = 5.3 \times 10^{34}\,erg\,s^{-1}$, the fundamental plane scaling implies $M = 1.9 \times 10^3\,\rm M_{\odot}$ and $L_{\rm X} = 2.5 \times 10^{41}\,\rm erg\,s^{-1}$. This inferred luminosity suggests that the source should be very bright in X-rays and that it could be an intermediate mass BH system. For the Eddington limited case $L_{\rm X} \propto M$ and thus $L_{\rm radio} \propto L_{\rm X}^{1.4}$, leading to a scatter of 1.4 dex in $L_{\rm X}$, the same as that estimated for the radio/X-ray correlation. This scatter introduces an uncertainty of a factor of about 30 into the implied $L_{\rm X}$. If $L_{\rm X}$ is reduced by a factor of 30, the resulting luminosity is still several orders of magnitude higher than the upper limit estimated from the spectral fits.

It should be noted that $L_{\rm radio}/L_{\rm X}$ could sometimes be higher for HMXBs than for LMXBs. HMXBs have dense stellar winds that might interact with the jets from the BH (see e.g. Romero et al., 2003). Any jet-wind interaction could give rise to synchrotron radiation thereby increasing the radio emission of the system. The mass transfer rate, $\dot{M}$, of the binary system also increases with the mass of the donor star (see § 2.5). Additionally, HMXBs in Roche lobe overflow may have donor stars

sufficiently massive to allow unstable mass transfer. If this happens, the accretion rates can become highly super-Eddington. When $\dot{M}$ is strongly super-Eddington, the accretion disk is expected to become geometrically thick and the X-rays from the BH are scattered and absorbed (e.g. Begelman et al., 2006). Both the low radiative efficiency in the X-rays and the high radiative efficiency of the jets in radio then serve to increase $L_{\rm radio}/L_{\rm X}$.

Now we compare the M 82 source to other non-standard BHBs to try and establish whether or not our source could be such a system. Cyg X-3 was discovered in 1966 in X-ray survey of the Cygnus region of the galaxy (Giacconi et al., 1967). The source was subsequently detected across the electromagnetic spectrum, from radio to γ-ray (see Vladimirskiĭ et al., 1985, and references therein), with γ-ray flares reaching energies > 100 MeV (Tavani et al., 2009). The emission from Cyg X-3 was found to vary on timescales ranging from weeks to minutes. Infrared data suggest that Cyg X-3 has a massive companion, making it a HMXB (van Kerkwijk et al., 1992).

Cyg X-3 is the brightest quasi-persistent Galactic BHB at radio wavelengths with a peak flux density of approximately 20 Jy at 2.25 GHz (Waltman et al., 1995). When scaled to the distance of Cyg X-3 (d=9 kpc; Predehl et al., 2000) the peak flux density of our source is 110 Jy, more than fives times that of the brightest Cyg X-3 flare. Thus this source would be exceptionally radio bright if it is a microquasar. Moreover, the spectral index of Cyg X-3 varies greatly during flaring episodes, with $-0.4 \lesssim \alpha \lesssim 1.8$ (Waltman et al., 1995). It is then unlikely that Cyg X-3 and the source in M 82 are in the same accretion state. Figure 2.4 (top panel) shows a radio (2.25 GHz) light curve of Cyg X-3 for a period of 150 days taken with the Green Bank Interferometer (GBI) (Waltman et al., 1995). The horizontal line indicates the peak flux density of our source scaled to the distance of Cyg X-3.

Most other Galactic microquasars have radio flaring events that show a rapid increase in flux density over periods of hours to days; the flares then decay back to quiescent levels within a few days to weeks (see e.g. Hannikainen et al., 2001; Brocksopp et al., 2002; Fender et al., 2002; Stevens et al., 2003). The flux density of the M 82 source increased by at least a factor of five over a period of a few days. Unlike most other microquasars, however, the source then remained at approximately constant flux for several months, with flux density variations of less than a factor of two (Muxlow et al., 2010, see Fig. 2).

SS 433 is an exotic Galactic microquasar. This source was first identified as a star with Hα emission (Stephenson & Sanduleak, 1977). Subsequent observations showed that it was a variable X-ray and radio source (Feldman et al., 1978; Seaquist et al., 1978). This system is a close, high mass, eclipsing binary with a period of 13.1 days (Crampton et al., 1980; Cherepashchuk, 1981; Hillwig & Gies, 2008). SS 433 was the first stellar object found to have relativistic jets (see e.g. Fabrika, 2004). These jets

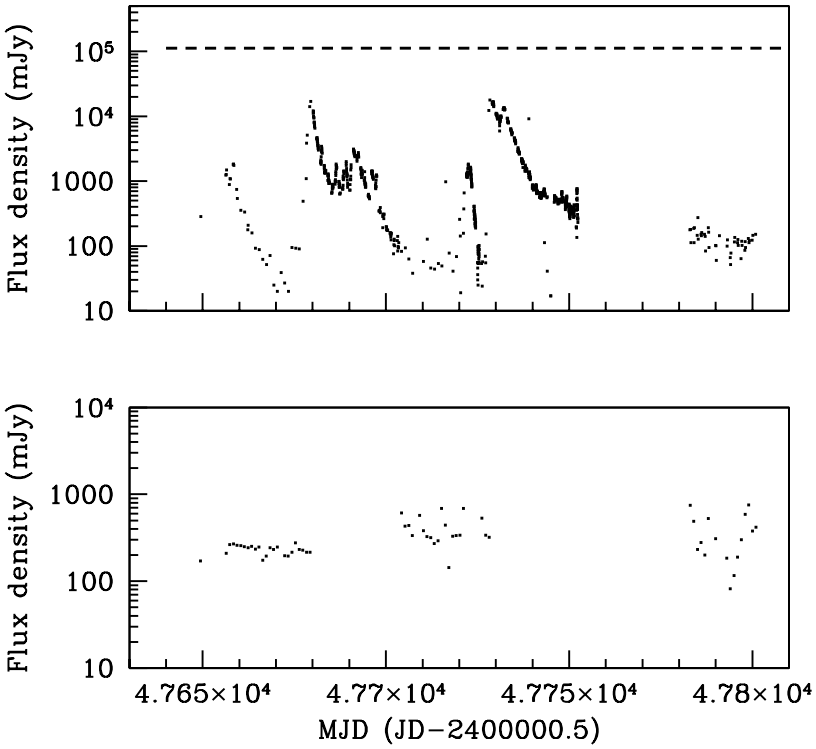

FIGURE 2.4: Light curves of Cyg X-3 and SS 433 for the same 150 day period. Top panel: A light curve of Cyg X-3 taken with the GBI at 2.25 GHz (Waltman et al., 1995). The horizontal line indicates the flux density of our source scaled to the distance of Cyg X-3. Bottom panel: A light curve of SS 433 taken with the GBI at 2.7 GHz (data downloaded from the GBI website; see Fiedler et al., 1987, for data analysis procedure).

were shown to be precessing and helical and they give rise to highly blue- and redshifted (tens of thousands of $\mathrm{km\,s^{-1}}$) optical emission lines (see e.g. Margon et al., 1979; Fabian & Rees, 1979; Hjellming & Johnston, 1981). SS 433 is thought to be undergoing super-Eddington mass transfer (roughly $10^{-4}\,\mathrm{M_\odot}$/year; Fabrika, 2004, and references therein) onto the compact object. The entire system is surrounded by a cocoon of gas called the W50 nebula (Margon, 1984). This gaseous envelope is thought to have arisen due to the interaction between the jets of SS 433 and the surrounding interstellar medium.

In some respects SS 433 exhibits radio emission unlike that of other BHBs (e.g. Fabrika, 2004). A 150 day light curve for SS 433 taken with the GBI at 2.7 GHz is shown in Fig. 2.4 (bottom panel). The data were downloaded from the GBI website [1]; the procedure is the same as in Fiedler et al. (1987). The light curve of SS 433 is similar to that of our source as its flux density stays roughly constant over a period much greater than the decay time of most microquasar flares. In addition, the spectral index of SS 433 is -0.5 (Dubner et al., 1998), similar to that of the M 82 source.

[1] http://www.gb.nrao.edu/fgdocs/gbi/gbint.html

S 26 is already thought to be an extragalactic analogue of SS 433 (Soria et al., 2010). In contrast to the point-like M 82 transient, S 26 has extended structures of radio lobes and X-ray and radio hotspots nearly 300 pc apart enveloped in a cocoon of gas that has been inflated by the jets. The radio spectral index varies across the system. In the lobes $-0.7 \lesssim \alpha \lesssim -0.6$, it flattens across the cocoon with $-0.4 \lesssim \alpha \lesssim 0$ and is inverted near the base of the jets where $0 \lesssim \alpha \lesssim 0.4$. The core of S 26 has an X-ray luminosity of $\sim 7 \times 10^{36}\,\mathrm{erg\,s^{-1}}$ ($0.3 - 10\,\mathrm{keV}$), but no radio emission has been detected from this region ($3\,\sigma$ upper limit $\sim 3{\times}10^{33}\,\mathrm{erg\,s^{-1}}$). This more complex structure suggests that if S 26 and the M 82 source are binary systems with similar components (i.e. similar donor star and accretor), then S26 has been undergoing mass transfer for a much longer duration so that it has had a chance to power strong lobes.

2.5 Discussion

In Fig. 2.5 we present the observed upper limit on the X-ray luminosity and the X-ray luminosity predicted from the Gallo et al. (2003) correlation versus the radio luminosity on the plot of the observed X-ray and radio luminosities for BHBs, using the data from Calvelo et al. (2010). For the purpose of this comparison we recalculate L_{X} for the M 82 source to be in the $1{-}10\,\mathrm{keV}$ range and L_{radio} is calculated from the flux density data at 4.9 GHz. Data for SS 433 (Margon, 1984, and references therein) and Cyg X-3 (Gallo et al., 2003) are also included in the plot. The X-ray luminosity for the M 82 source is lower than any other transient Galactic BHB, yet the radio luminosity is exceptionally high. This, along with behaviour of the light curve, makes it unlikely that the source is a normal microquasar. Like the M 82 source, SS 433 is also relatively faint in X-rays compared to radio, with $L_{\mathrm{X}} \sim 3 \times 10^{35}\,\mathrm{erg\,s^{-1}}$ ($2{-}10\,\mathrm{keV}$) and $L_{\mathrm{radio}} \sim 7 \times 10^{31}\,\mathrm{erg\,s^{-1}}$ at 4.9 GHz. The M 82 transient source could therefore possibly be an extragalactic analogue of this system.

As we note in § 2.3, there are fewer source counts in Obs ID 10026 than in 10025. This deficit appears to affect mainly the soft ($\lesssim 2\,\mathrm{keV}$) X-ray emission. Using aperture photometry, we find that there are 340±18.44 in Obs ID 10026 and 283±16.82 in 10025 in the $0.3 - 2\,\mathrm{keV}$ range, leading to a deficit of 57±24.96. This count deficit is therefore significant at the $2\,\sigma$ level.

Using the simulation tool `PIMMS`, the exposure time for Obs ID 10026 (17.4 ks) and a power law model with $\Gamma = 2$, we find that the difference in counts in the soft X-rays between the two observations is equivalent to $6.2{\times}10^{37}\,\mathrm{erg\,s^{-1}}$ in the $0.3 - 10\,\mathrm{keV}$ range.

If the X-ray emission detected in Obs ID 10025 represents the peak X-ray flux from the source, then it is still an unusual source, as the ratio of X-ray to radio flux is still low compared to normal Galactic BHBs, as discussed above. If, instead, the peak

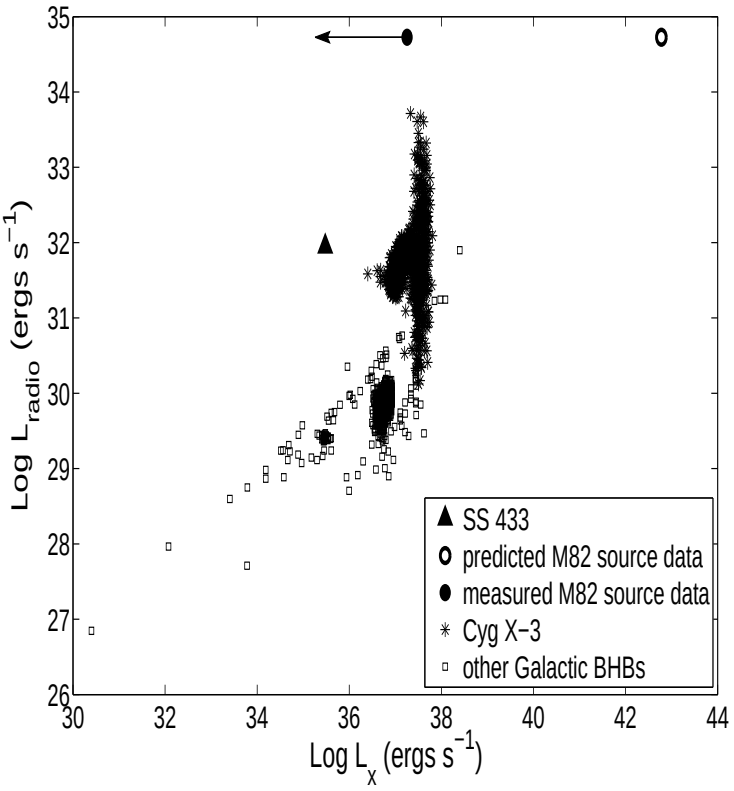

FIGURE 2.5: Plot showing radio/X-ray correlation for hard state BHBs. The squares indicate the BHB data from Calvelo et al. (2010); the X-ray data are in the 1−10 keV range and the radio data are calculated at 5 GHz. The triangle shows a representative SS 433 data point (2−10 keV and 4.9 GHz for X-ray and radio data respectively; Margon, 1984, and references therein). The asterisks indicate Cyg X-3 data (2−11 keV and 4.9 GHz for X-ray and radio data respectively; Gallo et al., 2003). The filled and open circles are the actual and estimated (from the radio/X-ray correlation) data for the M 82 source respectively, with $L_{\rm X}$ in the 1−10 keV range and $L_{\rm radio}$ calculated at 4.9 GHz. The errors have been omitted from the plot for clarity. For error estimates see Merloni et al. (2003).

X-ray emission occurred in the days before Obs ID 10026 (X-ray flares in transient outbursts usually decay back to quiescence over a period of a few days; see e.g. Hjellming & Rupen, 1995; Kuulkers et al., 1999; Rodriguez et al., 2008, and references therein), then the radio lag between X-ray and radio peak emission is about three weeks. A three week lag between X-ray and radio peak emission is a week longer than some of the longest lags seen in X-ray transients (see e.g. Harmon et al., 1995).

The fact that the M 82 source has a significantly higher radio luminosity than SS 433 could be explained, perhaps, by a more massive donor star. The mass of the donor star in SS 433 is thought to be only about 12 $M_\odot$ (Hillwig & Gies, 2008). This mass is at the lower limit for systems powered by thermal timescale accretion onto a BH (King et al., 2000). It is worth bearing in mind that at the distance of M 82, SS 433 and the W50 nebula would be difficult to distinguish from a supernova remnant. Additionally, the flux density of W50 ($d = 5.5$ kpc) is 70 Jy at 1.4 GHz

(Dubner et al., 1998). At the distance of M 82, the flux density would be 160 μJy spread over an angular scale of 7″. At these flux densities such sources will be impossible to detect as they are well below the confusion limit for M 82 (1.45 mJy with 1″ angular resolution at 4.9 GHz; Kronberg et al., 1981). Thus only the brightest and/or most compact SS 433-like systems will be detectable in galaxies like M 82.

Strong blue- and redshifted optical emission lines like those seen in SS 433 could potentially be used a diagnostic tool to verify the nature of our source. SS 433 has an R band magnitude of 12 mag; the H α emission line is 10 times brighter than the continuum and 5 000 km s^{-1} wide. At the distance of M 82, assuming similar intrinsic luminosity and extinction, the continuum of our source would not be detected with ground based instruments, but the H α line should be. Given that the radio luminosity of the M 82 source is many times greater than that of SS 433, it would not be surprising if the M82 source were also more luminous optically, increasing the chances of detecting the emission lines. However, if the M 82 source suffers from more extinction there may also be several bright infrared emission lines (Paschen α and Brackett γ to B15) that could be used to identify it instead (Thompson et al., 1979).

2.6 Conclusions

We have shown that the recently discovered transient in M 82 is relatively faint in X-rays given its radio luminosity. The lack of variability in its radio light curve also makes it unlikely that the source is a normal BH transient. The source could very well be the extragalactic analogue of SS 433 or a younger version of S 26.

Chapter 3

The X-ray point source population of NGC 4472: a deeper look using long *Chandra* observations

3.1 Introduction

The *Chandran X-ray Observatory* (Weisskopf et al., 2000) has made it possible to carry out detailed studies of low mass X-ray binaries (LMXBs) beyond the Local Group, allowing us to probe these systems in a wide variety of galactic environments. LMXBs can be formed either at the end point of stellar evolution or via N-body capture in globular clusters (GCs) (Clark, 1975; Fabian et al., 1975; Hills, 1976). Yet, despite all we know about them, many unanswered questions about LMXBs still remain. Is the LMXB X-ray luminosity function universal across all galaxies? Is there a difference between LMXBs found in the field of the galaxy and those found in GCs? Why do XRBs prefer red GCs over blue ones? The GC-LMXB relationship is of particular interest as these clusters appear to be a rich environment for LMXBs (see §1 for a discussion on the GC-LMXB connection). It is necessary to study nearby elliptical galaxies and their GC systems to gain a better understanding of the issues related to LMXB formation and evolution.

NGC 4472 is a massive (8×10^{11} $M_{\odot}$; Côté et al., 2003), nearby elliptical galaxy that is falling into the Virgo cluster (d = 16 Mpc; e.g. Macri et al., 1999). It contains much less bright diffuse X-ray gas than other massive nearby ellipticals such as M 87 and NGC 1399, making it easier to probe fainter X-ray point sources within the galaxy. NGC 4472 has a system of roughly 6000 globular clusters (Rhode & Zepf, 2001) and is therefore an excellent environment in which to study the GC-LMXB connection.

Kundu et al. (2002) studied the X-ray point source population of NGC 4472 using a 40 ks *Chandra* observation and archival *Hubble Space Telescope* (*HST*) data (see also Kundu & Whitmore, 2001). They considered only X-ray data from the *Chandra* ACIS–S3 chip and excluded the central 8" due to the high background in this region. A total of 144 X-ray sources were detected. This study found that the spatial distribution of the GCs, the GC-LMXBs and the field LMXBs were similar. They showed that 30 of the 72 LMXBs situated within the *HST* fields were coincident with GCs. The subsequent work of Maccarone et al. (2003) found no statistically significant differences between the X-ray properties of the GC and field LMXBs. These findings could imply that a significant proportion of field LMXBs were created in GCs and then ejected from the cluster due to dynamical interactions or the destruction of the cluster.

More recently, similar studies using deep X-ray observations have been carried out on nearby early type galaxies. Kim et al. (2006b) used archival data for six elliptical galaxies to study their LMXB populations. A total of 544 field and 285 GC sources were found. Brassington et al. (2008) studied the X-ray point source population of NGC 3379. They found 132 LMXBs, 10 of which reside in GCs. The survey of NGC 4278 by Brassington et al. (2009) revealed 236 LMXBs with 39 found to be in GCs. NGC 3379, NGC 4278, and NGC 4697 were found to have between 90 and 170 LMXBs each (Kim et al., 2009). The combined data for these three galaxies showed 75 LMXBs residing in GCs. Voss et al. (2009) analysed the LMXB populations of Cen A, finding 146 field sources and 47 GC-LMXBs. Zhang et al. (2011) studied the LMXB population of several nearby galaxies in various environments and found a total of 185 GC-LMXBs and 1033 non-GC LMXBs.

More recent deep *Chandra* data has become available for NGC 4472. By combining these data with archival observations we should be able to detect enough X-ray sources to carry out robust comparisons of various LMXB populations within the galaxy. The data sets also span many years and would thus allow us to study the long term variations of the X-ray sources as well as search for transient sources.

3.2 Observations and Data Analysis

In this work we used both archival and recent Chandra observations of NGC 4472 to study its X-ray point source population. All the data were taken with ACIS-S. The most recent data were taken in 2011 on February 14 (Obs ID 12889) and February 21 (Obs ID 12888); with exposure times of 140 ks and 160 ks respectively. Two shorter observations of 40 ks each were also used, giving a total exposure time of 380 ks. The more recent of the two (Obs ID 11274; Maccarone et al., 2010) was taken on February 27 2010 and the oldest observation (Obs ID 321; Kundu et al., 2002) was taken on June 12 2000. These data are summarised in Table 3.1.

Date	Obs ID	Exposure Time (ks)
2000-06-12	321	40
2010-02-27	11274	40
2011-02-14	12889	140
2011-02-21	12888	160

TABLE 3.1: A list of all the *Chandra* observations of NGC 4472 used in this work.

All the data sets were first reprocessed with the CIAO [2] script *chandra_repro* using calibration data from March 2011. New level two event files were created for all the observations using this script. The data were then checked for background flares and these were eliminated. The event files and images were restricted to the well calibrated 0.5–5 keV range using the CIAO command *dmcopy*.

Exposure maps were created for each CCD chip of each observation using the *asphist*, *mkinstmap* and*mkexpmap* scripts. PSF files were produced using *mkpsfmap* to determine the size of the PSF at each position on the images. The exposure maps and PSF file data were then used by the point source detection script *wavdetect* with a false source detection probability threshold of 10^{-7} to correctly identify point sources in the images.

All sources within $8''$ of the galaxy centre were excluded to avoid the area of very high X-ray background, consistent with the work of Kundu et al. (2002). Furthermore, only sources within $3.7'$ of the galaxy centre were included in this study, to avoid areas close to the CCD edges that were not adjacent to another CCD. Thus we only include sources from ACIS-S3 and ACIS-S4 in this this work. To illustrate this, Fig. 3.1 shows the included and excluded regions of NGC 4472 for Obs ID 12889.

We obtained a counts-to-energy conversion factor by comparing the fluxes of two bright sources with their respective net count rate. The spectrum of a bright source that had a disk blackbody (diskbb) continuum with an inner disk temperature, $k\mathrm{T} = 1.5$ keV, and one that had a power law (PL) continuum with Γ=1.7 were analysed in ISIS and fluxes and flux errors were obtained. The respective net count rates (net counts per source divided by the net exposure) and the corresponding errors were obtained from *wavdetect*. The counts-to-energy conversion factor was then calculated by dividing the flux obtained through spectral fitting by the net count rate of each source. These conversion factors were then used to calculate the X-ray fluxes for both diskbb and PL models for the rest of the X-ray point sources using their respective count rates. The errors for the flux values were calculated by using the flux errors obtained from ISIS for the two bright sources mentioned above and the errors on the count rate obtained from *wavdetect* and propagating them in the standard way.

[2] http://cxc.harvard.edu/ciao4.4/threads/index.html

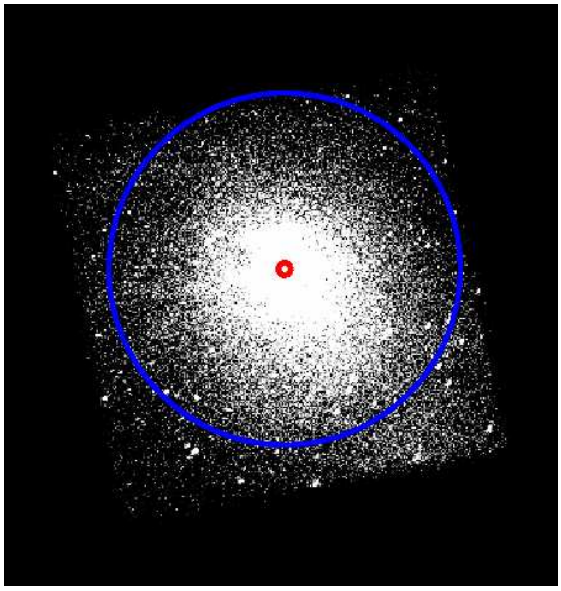

FIGURE 3.1: The X-ray area of NGC 4472 covered by Obs ID 12889. The area inside the red circle was excluded from the search for X-ray point sources because the X-ray emission from the centre of the galaxy is too high in that region. The area inside the blue circle is the 3.7′ region in which we search for X-ray point sources.

A $4\,\sigma$ completeness limit was calculated for the combined 380 ks data set. Using the smoothed background image of the data set created in *wavdetect*, the number of background counts at each source position was determined using the a region enclosing 90 % of the the source energy. This gives the background sensitivity as a function of position. The $4\,\sigma$ upper limit was then calculated and these background counts were then converted to flux values using the counts-to-energy conversion factor. It was found that the diffuse X-ray emission in the central region of the galaxy dominated the background sensitivity and the completeness limit was determined based on the flux values in that region.

We made use of the TOPCAT programme to search for sources coincident with GCs found in both ground (Rhode & Zepf, 2001) and space based (Jordán et al., 2009) optical observations. Rhode & Zepf (2001, hereafter referred to as RZ01) surveyed the GC system of NGC 4472 using *B, V* and *R* filters. The survey field covers the central 0.66′–23′ region of the galaxy and 1465 GCs were detected (see Fig. 3.2).

Jordán et al. (2009) surveyed the GC system of the inner region of NGC 4472 using the F475W and F850LP bandpasses as part of their *Virgo Cluster Survey* (VCS). These bandpasses are approximately equivalent to the Sloan *g* and *z* filters respectively and will be referred to as such in the rest of the is work. This survey covers the central $3.3' \times 3.3'$ of the galaxy (see Côté et al., 2004); 764 GCs were detected in this region of NGC 4472. This area is shown in Fig. 3.2.

We estimated the boresight corrections for the X-ray positions by calculating the weighted mean offset between obvious initial matches of the optical and X-ray data.

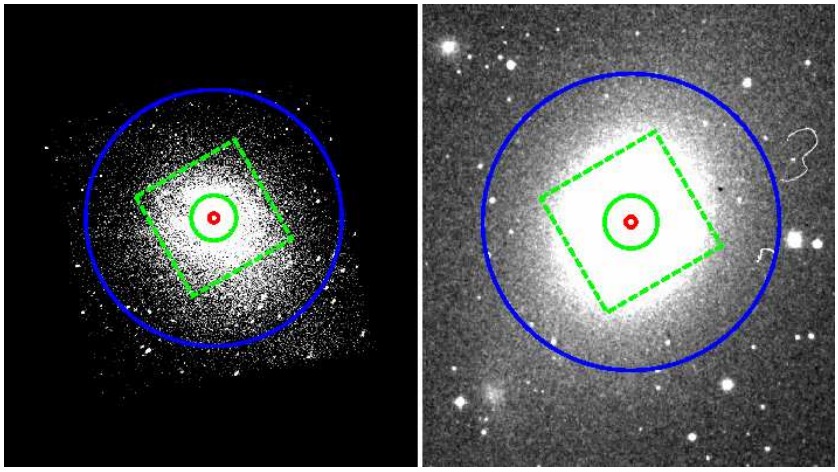

FIGURE 3.2: The X-ray (left panel) and optical (right panel) images of NGC 4472 showing the areas covered by the surveys of Rhode & Zepf (2001) and Jordán et al. (2009). The X-ray data shown is from Obs ID 12889. The optical image is from the DSS survey. The red and blue circles are the same as in Fig. 3.1. The green circle encloses the region of NGC 4472 that was *not* covered by the RZ01 survey. The rest of the X-ray and optical fields of view are covered by the RZ01 survey as the field extends out to 23′ from the centre of NGC 4472. The green square with dashed lines indicates the area covered by the VCS survey.

The RZ01 data had offsets of -0.25″ (RA) and -0.50″ (DEC), while the VCS positions had offsets of 0.18″ and 0.10″ for RA and DEC respectively. These mean offsets were then applied to the X-ray positions and a 0.75″ matching radius was used.

The false match probability for matches between the optical and X-ray data were determined by shifting each X-ray source position by a distance much greater than the matching radius and much smaller than the field of view and then seeing how many matches were found. In this case, the shift value used was 10″.

3.3 Results and Discussion

3.3.1 X-ray point source population

We find 242 sources within 3.7′ of the galactic centre, 70 of which are bright enough to be detected in all four observations. 194 sources are found to be brighter than $6.3\times10^{-16}\,\mathrm{erg\,s^{-1}\,cm^{-2}}$ (0.5–2 keV; $L_{X,0.5-5\,keV}=3.7\times10^{37}\,\mathrm{erg\,s^{-1}}$), the $4\,\sigma$ completeness limit for the combined data set. We expect roughly 10 of the X-ray sources to be background sources at this completeness limit (Tozzi et al., 2001). These data are summarised in Fig. 3.3.

A list of the X-ray luminosities of the sources can be found in Appendix A. A sample of this table is shown in Table 3.2.

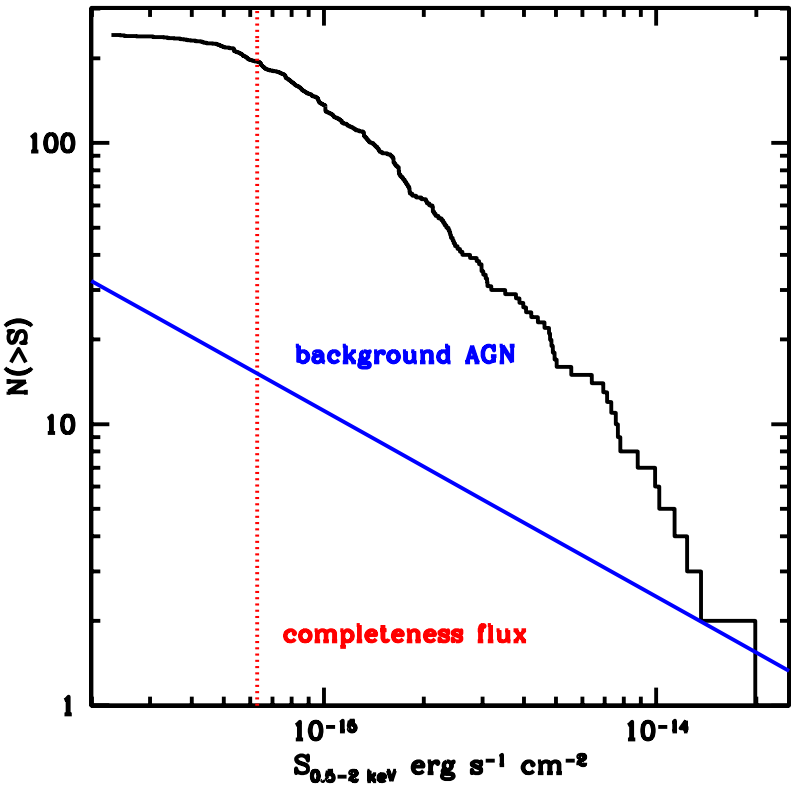

FIGURE 3.3: The log N–log S plot for the entire XRB sample. The dotted vertical line indicates the 0.5–2 keV completeness limit and the diagonal solid line indicates the number of background sources as a function of flux (see Eqn.,1 in Tozzi et al., 2001).

RA	DEC	$\mathrm{Flux_{PL}}$	$\mathrm{Flux_{PL}}$ err	$\mathrm{Flux_{PL}}$	$\mathrm{Flux_{PL}}$ err	$\mathrm{Flux_{DBB}}$	$\mathrm{Flux_{DBB}}$ err	$\mathrm{Flux_{DBB}}$	$\mathrm{Flux_{DBB}}$ err	Flag
degrees	degrees	0.5–5 keV	0.5–5 keV	0.5–2 keV	0.5–2 keV	0.5–5 keV	0.5–5 keV	0.5–2 keV	0.5-2 keV	Flag
187.49977	8.02063	1.456E-14	1.724E-15	7.641E-15	9.052E-16	1.536E-14	1.829E-15	6.248E-15	7.436E-16	
187.49804	8.02989	9.137E-16	2.96E-16	4.795E-16	1.553E-16	9.639E-16	3.125E-16	3.921E-16	1.271E-16	
187.49757	7.99843	1.097E-15	2.586E-16	5.759E-16	1.357E-16	1.158E-15	2.732E-16	4.709E-16	1.111E-16	
187.49175	7.96768	2.955E-15	7.334E-16	1.551E-15	3.849E-16	3.118E-15	7.746E-16	1.268E-15	3.151E-16	
187.4915	7.96826	1.831E-15	3.881E-16	9.61E-16	2.037E-16	1.932E-15	4.101E-16	7.858E-16	1.668E-16	
187.49098	7.99121	1.57E-15	3.028E-16	8.242E-16	1.589E-16	1.657E-15	3.201E-16	6.739E-16	1.302E-16	
187.49021	7.9924	1.708E-15	3.068E-16	8.962E-16	1.611E-16	1.801E-15	3.245E-16	7.328E-16	1.32E-16	GC

TABLE 3.2: A sample of the table of X-ray fluxes of the sources within 3.7' of the galaxy centre. The fluxes are in units of erg $\mathrm{s^{-1}}$ $\mathrm{cm^{-2}}$. The PL and DBB subscripts denote the spectral model conversion factor used to calculate the flux. The "err" designation denotes flux errors. The flag column identifies sources that are interesting and/ or for which caution must be used when analysing the source properties. The key is as follows: bkg = source in an area of high background, c = *wavdetect* has misidentified or not detected the source in one of the observations, cg = the source is in or very close to a chip gap in one of the observations and GC = the source is associated with a globular cluster.

We have constructed the X-ray luminosity function (XLF) for NGC 4472 using multi-epoch data. One might therefore believe that the population of transient X-ray sources in the galaxy would lead to an incorrect XLF. However, Grimm et al. (2003) point out that XLFs created from *Chandra* observations of the same galaxy taken at different times and even from different parts of the galaxy were not significantly different from each other. Thus we expect that combining observations of NGC 4472 taken at different time, but covering the same area to create one XLF would not lead to an incorrect XLF. Kim et al. (2006a) also found that source variability did not change the slope or normalisation of an XLF created from merged data sets taken at different epochs compared to XLFs created from individual observations.

We fit a power law function to the differential XLF, using only the completeness limited luminosity data. The function has the form $\frac{dN}{dL_X} = kL_X^{-\beta}$ (see e.g. Kim et al., 2006a, and references therein). We use a maximum likelihood fitting procedure to find the best fit parameters, as outlined in Scaife & Heald (2012).

We find that the best fit parameters for the slope and normalisation are $\beta = 2.1 \pm 0.09$ and $k = 74.37 \pm 5.48$ respectively. This slope is in good agreement with the results of other studies of the XLF for individual ellipticals as well as the average XLF for an ensemble of elliptical galaxies, where β is typically found to be ~ 2 (e.g. Kim & Fabbiano, 2004; Kim et al., 2006a). The cumulative XLF is shown in Fig. 3.4.

Other studies have found that the XLF for LMXBs in elliptical galaxies are better fit with a broken power law function due to a flattening of the luminosity distribution at low luminosities ($L_X \lesssim 5 \times 10^{37}\,erg\,s^{-1}$)) (e.g. Voss & Gilfanov, 2006). Gilfanov (2004) suggested that this flattening is a ubiquitous property of the XLF for LMXBs. In the case of NGC 4472 itself, Kundu et al. (2002) found that the XLF required a broken power law fit, with a break at $L_X = 3 \times 10^{38}\,erg\,s^{-1}$. This break is also seen in the XLF of other galaxies and it was suggested that this break corresponds to the transition in the XLF from neutron star to black hole binary luminosities (Sarazin et al., 2000).

We fit a broken power function to our XLF, leaving the break luminosity free to vary. We determine the Bayes factors, Z, for each function fit to the XLF and use the ratio of these factors to determine whether or not there is evidence to support the need for a broken power law fit (see e.g.§4 in Scaife & Heald, 2012, ; and references therein). We find that $\ln Z = -202.7 \pm 0.05$ and -202.8 ± 0.08 for the single and broken power law fits respectively, giving $\Delta \ln Z = 0.07$. The Jeffreys scale is used to assess the ratio of Bayes factors and determine where they are sufficient to imply that the broken power law is required. Since $\Delta \ln Z \ll 1$, we find no evidence for that broken power law is needed to fit our XLF. Kim et al. (2006a) also find that the flattening of the XLF slope at low luminosities is not seen in their ensemble of galaxy XLFs. They caution against the acceptance of the flattening as a general characteristic of the XLF across

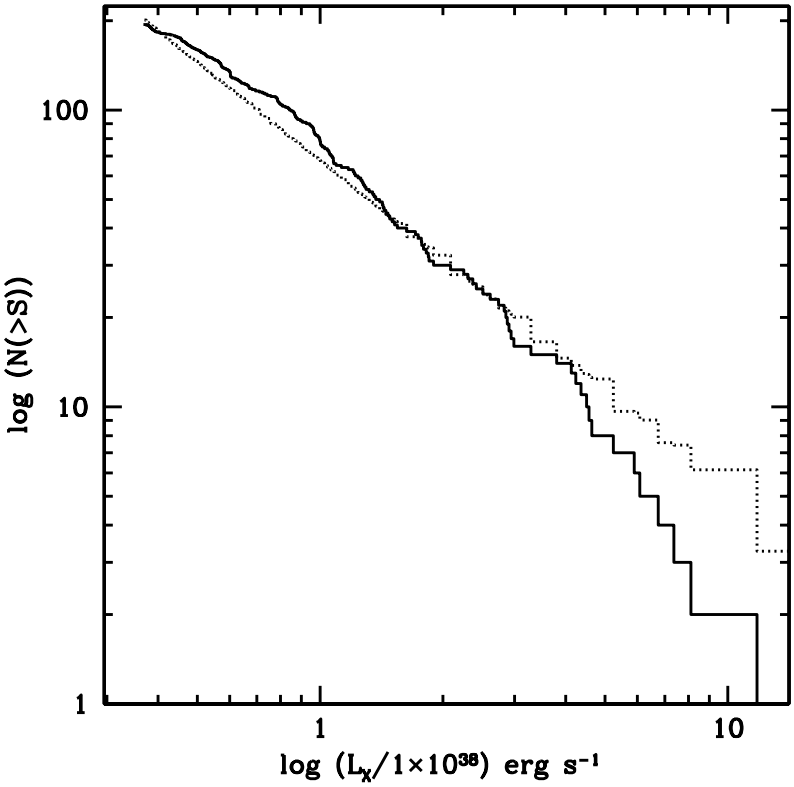

FIGURE 3.4: The X-ray luminosity function for the completeness limited XRB sample (sold line) with the best fit function over plotted (dotted line). The luminosity is for the 0.5–5 keV range and have been normalised to $10^{38}\,\mathrm{erg\,s^{-1}}$.

all galaxies, since factors such as incompleteness and multiple XRB populations may not have been taken into account in other studies.

We note that since our completeness limit is $3.7{\times}10^{37}\,\mathrm{erg\,s^{-1}}$, we do not sample the same low luminosity range as other studies. It is then perhaps not surprising that we do not see the flattening of the XLF slope at low luminosities.

3.3.2 Globular cluster LMXB population

We find that a total of 81 of the 242 detected X-ray sources are associated with GCs, 68 with fluxes above the completeness limit. We found that 233 X-ray sources lie within the RZ01 survey field and of these 40 were found to have a match with a RZ01 GC, with a subsample of 35 with fluxes above the X-ray completeness limit. The VCS field included 210 X-ray sources and 62 matches were found with this data, 49 of which have fluxes above the completeness limit. We estimate that there would be two and five false matches in the RZ01 and VCS samples respectively.

RZ01 found that their GC sample has a bimodal $B-R$ colour distribution with peaks at 1.1 and 1.35, with a dividing $B-R$ colour of 1.23. Using this criterion we

find that 28 of the 40 RZ01 GCs in our sample are red and 12 are blue. Using only the X-ray completeness limited subsample, 9 RZ01 GCs are blue and 26 are red. When we account for the larger number of blue GCs in the RZ01 catalogue, we find that red GCs are 4.4 times more likely than blue GCs to host a LMXB.

For the VCS GC sample, the $g-z$ colour distribution is also bimodal, with peaks at roughly 1.1 and 1.45 and a dividing $g-z$ colour of approximately 1.17 (see Fig. 6 in Jordán et al., 2009). We then have 56 red and 6 blue VCS GCs in our sample; the completeness limited subsample contains 6 blue and 43 red GCs. Correcting for the greater number of red GCs in the sample, we find that a red GC is 4.6 times more likely to host an LMXB than a blue GC.

Previous studies (see e.g. Kundu et al., 2002; Jordán et al., 2004; Kim et al., 2006b; Sivakoff et al., 2007; Kim et al., 2009) have found that red GCs are roughly three times more likely to host a LMXB than blue GCs. Jordán et al. (2004) provide the figure with the largest error, 3±1. Thus our values of 4.4 and 4.6 are significantly higher and not consistent with these results.

3.3.3 Field versus globular cluster LMXB populations

We compare the GC and field LMXB populations to ascertain whether the the two populations have significantly different X-ray properties. We find that there is not statistically significant difference between the mean 0.5–5 keV luminosity for the GC-LMXB ($1.6^{+0.5}_{-0.6} \times 10^{38}\,\mathrm{erg\,s^{-1}}$) and field LMXB populations ($1.3^{+0.2}_{-0.3} \times 10^{38}\,\mathrm{erg\,s^{-1}}$). These values and findings are consistent with those found by Kundu et al. (2002) for their smaller sample of NGC 4472 LMXBs.

A Kolmogorov-Smirnov (KS) test was performed on the luminosities of the GC and field samples to quantify any differences. We find that the probability that the GC and field LMXB luminosities are drawn from the same sample cannot be ruled out at greater than the 13 % level. The findings of previous studies of other elliptical galaxies (see e.g. Kim et al., 2006b) as well as that of the previous study of NGC 4472 (Kundu et al., 2002) do not find any significant difference between the two luminosity distributions. Fig. 3.5 shows the normalised log N–log S plots for both the GC and field LMXB populations.

However, our samples have a limiting luminosity of $3.7{\times}10^{37}\,\mathrm{erg\,s^{-1}}$. Other studies, e.g. Voss et al. (2009) and Kim et al. (2009), find that the luminosity functions for field and GC-LMXB populations differ significantly for sources with $L_X < 10^{37}\,\mathrm{erg\,s^{-1}}$and $L_X < 5 \times 10^{37}\,\mathrm{erg\,s^{-1}}$ respectively, with fewer faint sources in the GC population. These results do not necessarily undermine the theory that all LMXBs are formed in GCs, as the ejected systems could well have different physical parameters

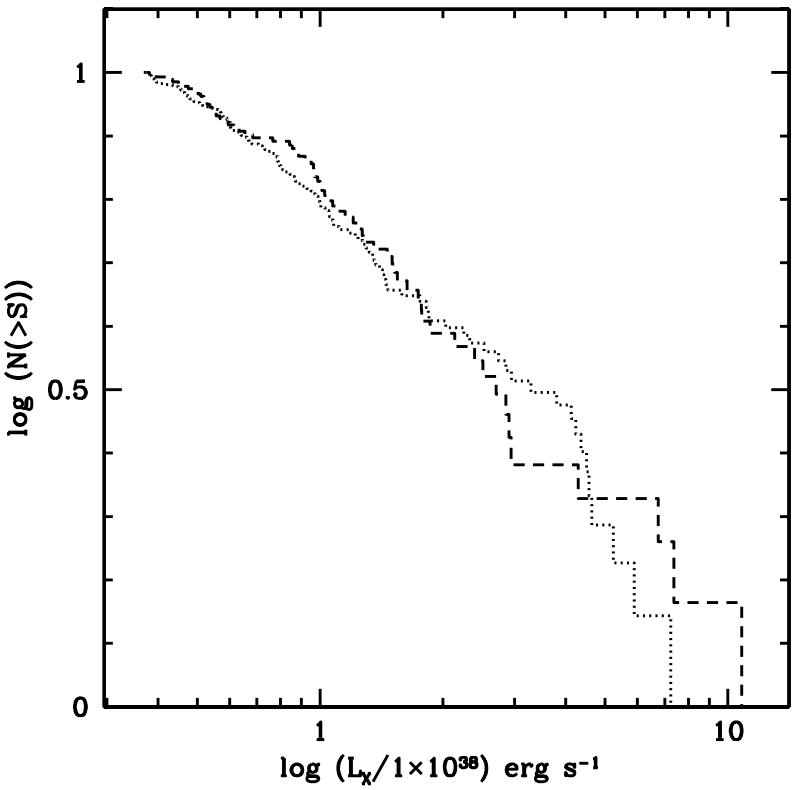

FIGURE 3.5: The log N–log L plots for the GC (dashed line) and field (dotted line) populations. The number of sources in each sample has been normalised to one for ease of comparison and the luminosity has been normalised to $10^{38}\,\mathrm{erg\,s^{-1}}$.

(orbital period, mass transfer rate, etc.) than the systems that are not ejected (e.g. Juett, 2005).

The radial distance distributions of the GC and field LMXB populations were also analysed. We perform a KS test and find that the probability that the two radial distance distributions are drawn from the same sample is 13 %. Kundu et al. (2002) found a similar result for NGC 4472. The radial surface density profiles for the GC and field populations is shown in Fig. 3.6. The radial density distribution of the GC LMXBs is broadly consistent with that of the field LMXB population. This similarity can be simplistically interpreted as evidence for the idea that the field is populated with LMXBs that have been ejected from GCs.

3.3.4 Red versus blue globular cluster subpopulations

We compare the red and blue GC subpopulations to try and determine the role that GC colour, and hence metallicity, plays in LMXB formation. For some of the analysis, we combine our VCS and RZ01 GC samples. This does not present a problem, even though not all VCS sources have RZ01 counterparts and vice versa. The colour

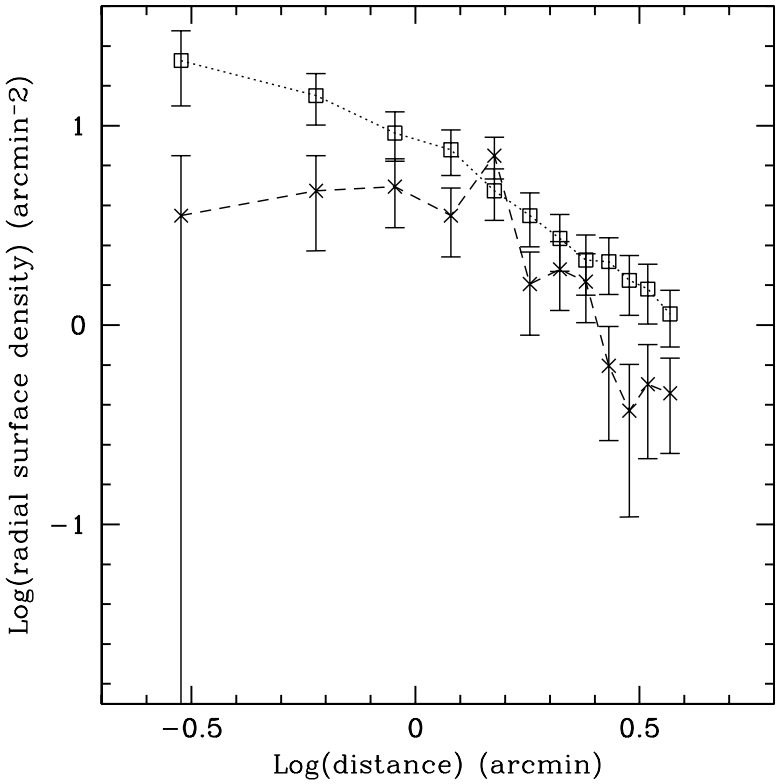

FIGURE 3.6: The radial density profiles for the GC (crosses and long dashed lines) and field (squares and short dashed lines) LMXB populations of NGC 4472.

bimodality of the GC system of NGC 4472 is well known and has been quantified by both the RZ01 and VCS surveys. It is an intrinsic property of the GC system. Therefore, for analysis that only requires the source to be labelled blue or red, it does not matter which photometric system was used to measure the colour of the GC. Once a GC colour has been measured and the GC has been assigned the red or blue qualitative property, we can use that to carry out further analysis. Combining the two samples and taking both X-ray and optical completeness into account, where the completeness limits are V ~ 23.5, $g = 23.3$ and $z = 22.2$ for RZ01 and VCS respectively, gives us a sample of 10 blue and 42 red GCs.

The mean 0.5–5 keV luminosity for the red and blue subpopulations are $1.5^{+0.7}_{-0.8} \times 10^{38}\,\mathrm{erg\,s^{-1}}$ and $2.2^{+1.8}_{-1.8} \times 10^{38}\,\mathrm{erg\,s^{-1}}$ respectively; they are statistically indistinguishable. Using a KS test, we find that probability that the two X-ray luminosity distributions are drawn from the same sample cannot be ruled out at more than the 12 % level.

The radial distributions of the red and blue GC subpopulations were analysed with a KS test. We find that the probability of the two distributions being drawn from the same sample is only 7.9 %. Thus there is marginal evidence to suggest that the red and blue LMXB hosting GC populations have different radial profiles. Figure 3.7 shows

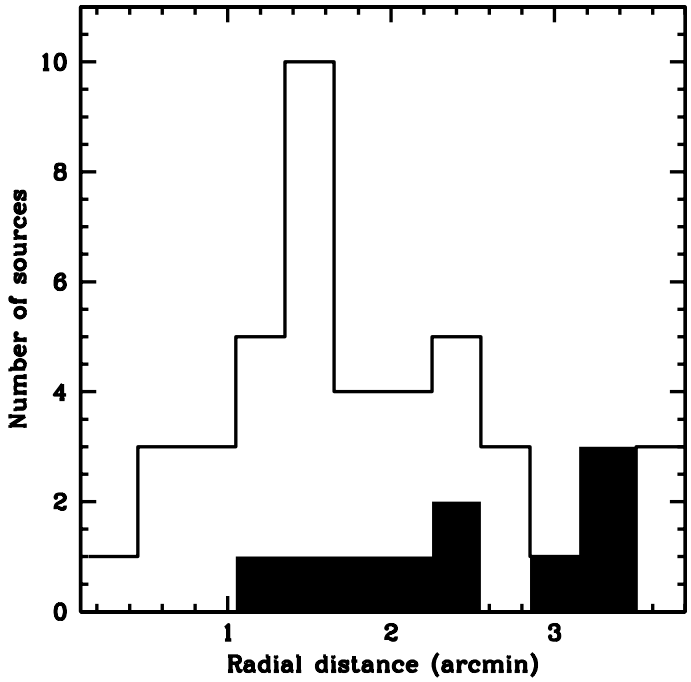

FIGURE 3.7: The histograms of radial distance for the red and blue GC subpopulations of NGC 4472. The shaded histogram is that of the blue GCs.

the histograms of radial distances for the blue (shaded) and red GC subpopulations. The blue GCs do not appear to be as centrally concentrated as the red GCs. This is consistent with the work of Kim et al. (2006b) who posited the idea that GCs with smaller galactocentric radius would be more compact to avoid tidal disruption and thus would have an increased rate of dynamical LMXB-forming processes.

The luminosity of a globular cluster is directly proportional to its mass (see e.g. Anders et al., 2003; Bruzual & Charlot, 2003). Therefore, we can use the photometric optical data to qualitatively assess the mass distributions of the red and blue GC samples. Unfortunately, due to the particular bandpasses used in the VCS and RZ01 surveys, it is not possible to convert all the photometric data of one survey to another. Therefore, we will assess the RZ01 and VCS samples separately.

The average brightness for red and blue RZ01 GCs that host LMXBs is V=21.36±0.13 and 21.65±0.20 respectively. For the VCS sample, the average red and blue g band values are 21.93±0.14 and 22.05±0.43 respectively. Both sets of red and blue brightness values agree within uncertainty. Thus there does not appear to be a mass difference between blue and red LMXB-GCs in NGC 4472.

3.4 Conclusions

We have found 242 XRBs in the central $3.7'$ of NGC 4472; of which 194 were brighter than the $4\,\sigma$ completeness limit of $6.3{\times}10^{-16}\,\mathrm{erg\,s^{-1}\,cm^{-2}}$ (0.5-2 keV). 81 LMXBs are found to reside in GCs. We have shown that there is no significant difference between the X-ray luminosities of the LMXBs in the field and those found in GCs. We note however, that all our sources have $\mathrm{L_X} > 10^{37}\,\mathrm{erg\,s^{-1}}$, which is greater than the value at which the luminosity functions are found to differ in other work.

Our study also shows that within the GC-LMXB population, the X-ray sources are preferentially found in red GCs at a ratio of roughly four to one. Our analysis of the red and blue GC subpopulations shows that they have indistinguishable X-ray properties. However, the respective radial source distributions provide tentative evidence that red LMXB hosting GCs are more centrally located. This finding, though marginal, supports the theory that red GCs are more likely to host LMXBs due to dynamical processes within the cluster rather than the metallicity of the cluster.

Chapter 4

Deep *Chandra* observations of the NGC 4472 globular cluster black hole XMMU 122939.7+075333

4.1 Introduction

XMMU 122939.7+075333, the first X-ray emitting globular cluster black hole (BH) system was discovered using data from *X-ray Multiple Mirror-Newton* (*XMM*) satellite (Maccarone et al., 2007). This source is situated in a spectroscopically confirmed globular cluster (RZ 2109) of the massive Virgo elliptical galaxy NGC 4472 (Rhode & Zepf, 2001). The peak X-ray luminosity of the source at discovery, $L_X = 4 \times 10^{39}\,\mathrm{erg\,s^{-1}}$, is more than 10 times the Eddington luminosity (L_{Edd} of a neutron star. This high luminosity makes the source an ultraluminous X-ray source (ULX; a non-nuclear X-ray source with $L_X > \times 10^{39}\,\mathrm{erg\,s^{-1}}$) . However, it was the rapid variability of its luminosity that confirmed this source as a BH. The luminosity varied by a factor of seven in just a few hours, thereby ruling out the possibility that the system is a superposition of neutron stars.

Shih et al. (2008) carried out spectroscopic analysis of XMMU 122939.7+075333 using the *XMM-Newton* data of Maccarone et al. (2007) as well as additional *Chandra* data. They found that the spectra were well fit by a multicolour disk model and had an inner disk temperature of about $kT_{in} = 0.15\,\mathrm{keV}$ with the same underlying continuum whether the source was bright or faint phase, but with varying absorption column. The results of this spectral analysis support the idea that the X-ray variability was due to a change in absorption column. Further investigation by Maccarone et al. (2010) using four short *Chandra* and *Swift* observations of XMMU 122939.7+075333 found that its luminosity appeared to be declining over a period of several years.

In addition to X-ray observations, XMMU 122939.7+075333 has also been studied at optical wavelengths. Zepf et al. (2007) found [O III] λ 5007 emission associated with the system. The emission line was found to have a velocity width of at least a few hundred km s^{-1} and a luminosity of about 4×10^{35} erg s^{-1}. An optical spectroscopic follow up with higher signal-to-noise by Zepf et al. (2008) revealed both [O III] λ 5007 and [O III] λ 4949 emission from XMMU 122939.7+075333. In addition to the narrow core already found by Zepf et al. (2007), these emission lines were found to have very broad wings with a velocity width of about 2000 km s^{-1} and were therefore blended. The total emission line luminosity was found to be 1.4×10^{37} erg s^{-1}. Moreover, the flux ratio of [O III] to Hβ is at least 30. A long term spectroscopic campaign was carried out by Steele et al. (2011) in order to monitor the variability and velocity structure of the [O III] emission from XMMU 122939.7+075333. No dramatic variation was found in the [O III] velocity structure over a time span of more than 400 days. However, the luminosity of the emission lines declined by approximately 10% over that period. Most recently, Peacock et al. (2012) used spatially resolved spectroscopic data from *HST*/STIS to determine that the spatial structure of the [O III] emission. They found that the half-light radius of the gas is between 3 and 7 pc and that the light profile of the oxygen gas emission is consistent with the light profile of RZ 2109's continuum.

Both the X-ray and optical data help to constrain the nature and evolution of XMMU 122939.7+075333. Maccarone et al. (2007) initially postulated that XMMU 122939.7+075333 is a wide binary system with a red giant donor star, based on the high luminosity of the system over a decade (Colbert & Ptak, 2002) and the fact that X-ray transients that have long orbital periods tend to have long outburst durations (e.g. Portegies Zwart et al., 2004). The X-ray variability could then be explained by obscuration of the X-ray source by a warped, precessing outer accretion disk formed in such a system (Shih et al., 2008).

The optical spectral data argue against this scenario, however. The high ratio of [O III] to Hβ determined by Zepf et al. (2008) suggests that the donor star is much more likely to be a hydrogen deficient star such as a white dwarf (WD), as first suggested by Gnedin et al. (2009). Most WDs are composed almost entirely ($> 99\%$ by mass) of carbon and oxygen (e.g. Dufour, 2011). Thus we would expect that the matter accreted from such a donor would be rich in carbon and oxygen and poor in hydrogen. This is in keeping with the findings of Zepf et al. (2008), who showed that the optical spectrum associated with XMMU 122939.7+075333 is poor in hydrogen and rich in oxygen.

On the basis of evolutionary arguments Ivanova et al. (2010) suggested that the system is most likely a hierarchical triple star system, with an inner stellar mass BH-WD binary. In this scenario, the outer star in the triple plays an important role in the evolution of the inner binary through the Kozai mechanism (Kozai, 1962). The

motion of the outer star in the triple perturbs the inner binary, causing the eccentricity of the binary to oscillate. These changes in eccentricity cause the binary orbit to shrink enough to allow mass transfer from donor to compact object. The Kozai mechanism continues to operate after mass transfer has started and the eccentricity of the inner binary is therefore still varying. The mass transfer rate ($\dot{m}$) is strongly dependent on the eccentricity (e) of the binary in the context of a triple ($\dot{m} \propto exp(e)$; see e.g. Hut & Paczynski, 1984). Maccarone et al. (2010) argued that we would expect $\dot{m}$ (and therefore the X-ray flux of the binary) to vary significantly on the time-scale for which e varies due to the Kozai mechanism. They showed that for representative values of the system parameters, the period of e variations is about 40 years; we then expect the X-ray flux of the inner binary to vary on a similar timescale. Maccarone et al. (2010) studied X-ray data for XMMU 122939.7+075333 that spanned 30 years and they show that long term variation in flux is consistent it declining on the timescale of the period of eccentricity. Thus the scenario of XMMU 122939.7+075333 as a triple system with an inner WD-BH binary was favoured.

The X-ray observations of XMMU 122939.7+075333 between 1994 and 2004 all showed that $L_X > 10^{39}\,erg\,s^{-1}$; it seemed plausible that the central object could be intermediate mass black hole (IMBH). The [O III] emission could then be caused by the tidal detonation of a WD by an IMBH (Rosswog et al., 2009; Irwin et al., 2010). But, the nature of the [O III] emission argues strongly against the central X-ray source of XMMU 122939.7+075333 being an IMBH. Because the oxygen emission is from forbidden lines, there are strong constraints on the density of the gas and therefore the number of emitting particles within a given volume. The emission lines are too luminous and broad for their velocity to originate from material in a Keplerian orbit around an IMBH given the volume available (Zepf et al., 2008). Moreover, Peacock et al. (2012) find that the [O III] emission region of XMMU 122939.7+075333 (on the scale of pc) is very much larger than the expected scale over which the velocity dispersion due to an IMBH would yield such a broad line (on the scale of 10^{-6} pc). In addition, the tidal detonation model is ruled out for similar reasons. The size of the [O III] emission region determined for this scenario is at least an order of magnitude smaller than observed. The explosion of the WD is also expected to produce heavy elements, such as iron, that should be observed in the optical spectrum, but are not.

The tidal detonation model also does not fit the X-ray data. Rosswog et al. (2009) predict that the accretion of the explosion's debris will cause a luminous X-ray flare that lasts for roughly one year followed by a $L \propto t^{-5/3}$ decay. This timescale of X-ray activity is not consistent with any of the X-ray observations of XMMU 122939.7+07533. The X-ray variability for the source is all below 0.7 keV. A changing absorption column is the simplest scenario that could explain the variability (Maccarone et al., 2007; Shih et al., 2008; Maccarone et al., 2010). This changing absorption could be due to a variable disk wind produced by super-Eddington

accretion onto the central BH; at lower accretion rates strong disk winds are not produced (Proga et al., 1998; Begelman et al., 2006).

It has also been suggested that the [O III] emission could be caused by the following scenarios: photoionisation by the central X-ray source of the ejected material from a nova event within RZ 2109 (Ripamonti & Mapelli, 2012) and photoionisation by the central source of an accretion disk wind driven from the system (Zepf et al., 2007, 2008). However, Peacock et al. (2012) show that the observed size of the [O III] emission region is more than an order of magnitude greater than the emission region of the nova ejecta model. The optical data are consistent with emission from a photoionised disk wind being driven across the globular cluster by a central source accreting at or above the Eddington limit (Zepf et al., 2008; Peacock et al., 2012).

Thus, given the above-mentioned, the model that best fits the available data for XMMU 122939.7+07533 is a triple system with a WD and stellar mass BH inner binary. It is not possible to constrain the nature of the third star in the triple system and, apart from the work of Ivanova et al. (2010), at present no good evidence exists favouring the triple scenario over binary evolution scenarios. The X-ray variability is likely to be due to a variable absorption column caused by an accretion disk which has the same composition as the WD donor star. The [O III] emission is likely to be from the disk wind, driven by moderately super-Eddington accretion onto the central compact object. The disk wind is then photoionised by the X-ray emission from the central source.

Such a system would have several observational features and parameters that could be observed to test the veracity of this model. A WD-BH binary is expected to be compact and have a short orbital period (Bildsten & Deloye, 2004). This gives rise to a high accretion rate, a fully ionised accretion disk and thus a persistently luminous X-ray source. The material from the WD would also have chemically enriched the accretion disk wind with oxygen and carbon. This would lead to soft X-rays (<1 keV) being absorbed preferentially, which means that the source spectrum would be softer when the source is more luminous. It may also be possible to detect X-ray and/ or ultraviolet emission lines from carbon or oxygen in the source spectra. If the photoionised accretion disk wind is variable, we expect to see aperiodic modulations of the X-ray luminosity due to obscuration by a changing absorption column (Proga et al., 1998).

Recent deep observations of XMMU 122939+075333 have made it possible to probe some of these questions. In this chapter we explore both the temporal and spectral properties of this source to help us improve our understanding of its nature. In particular, the data are of high enough quality that we are able to model the soft (<0.7 keV) excess in the spectra as a Gaussian line component.

4.2 Observations and Data Analysis

The two most recent deep observations of XMMU 122939+075333 were obtained from the *Chandra* telescope (Obs ID 12889 and 12888). They were taken one week apart on 14 and 21 February 2011 respectively, with exposure times of 140 ks and 160 ks respectively.

The data were first reprocessed using *Chandra* calibration data from March 2011 to create new level two events files with the CIAO *acis_reprocess_events* script. The images were then checked for background flares. We used *specextract* to produce source and background spectra and *dmextract* to make light curves. A long term light curve of the source was also produced using data from the *Chandra*, *XMM* and *ROSAT* telescopes.

Spectral analysis of the *Chandra* observations was carried out using the Interactive Spectral Interpretation System (ISIS) version 1.6.1. Only data in the well calibrated, low background range of 0.5−5 keV were used in our analysis. The Gehrels statistic was used to calculate errors as it gives a more reliable fit to data with low count rates (Gehrels, 1986). As the spectra include data with varying spectral shapes, the observations were split into bright and faint phases (with the dividing line being the mean count rate of $\sim 1.3 \times 10^{-3}$) to more accurately analyse the data. The bright and faint phase spectra were grouped to a minimum signal-to-noise ratio of three and two per bin respectively. These spectra were then separately fit with power law (PL) or disk blackbody (diskbb) continuum models (Mitsuda et al., 1989) and a Gaussian component to fit an excess of counts at ∼0.6 keV, with the Galactic absorption column, nH=$1.6 \times 10^{20}\,\mathrm{cm}^{-2}$ (Dickey & Lockman, 1990) to obtain the X-ray luminosity.

We do not have a sufficient number of counts in the spectra to allow for the fitting of models where both the spectral parameters and the absorption column are free to vary. We thus keep the absorption column frozen to the Galactic foreground value. The interstellar medium of elliptical galaxies contain very little cool molecular or atomic gas (see e.g. Welch et al., 2010), so any absorption from NGC 4472 itself would be negligible. To test whether varying absorption plays a significant role in the different between the faint and bright spectra, we also fit the faint spectra with the best fit parameters of their respective bright spectrum and allow nH to vary.

The full Obs ID 12889 and 12888 spectra and a 100 ks *XMM* observation of the source taken in 2004 (hereafter referred to as XMM04; Maccarone et al., 2007), were then fit jointly with the same models. A joint fit was used so that the Gaussian component could be tied to the same value across all three data sets. The data sets were fit simultaneously with the same continuum model, with the associated continuum spectral parameters (e.g. Γ) free to vary between each data set. The F test was carried out on the Gaussian line component to determine its significance.

The full Obs ID 12888 and 12889 spectra, XMM04 and the bright phase spectra were also fit (separately) with a model consisting of a diskbb continuum plus a PL component. This is the standard model used for Galactic BH binaries as well as ULXs. The faint phase spectra were not fit with this model as they do not contain enough counts to enable us to fit the model.

Due to the low number of source counts in each observation, we calculated hardness ratios in order to parametrise the spectra. The counts in the bright and faint phases were divided into hard (1−5 keV) and soft (0.5−1 keV) energy bands, such that there were a roughly even number of counts in each band for the bright phase. XMMU122939+075333 is situated near the edge of CCD chip ACIS-5 in Obs ID 12889 and 12888. In order to calculate the source count rate accurately, we made exposure maps of the chip using *mkexpmap* and used them to correct for the decreased effective area near the chip gaps. The hardness ratio, $HR = (H - S)/(H + S)$ where H and S are the number of counts in the hard and soft bands respectively, was then determined for bright and soft phase of each observation. We also compute the probability that the changes in hardness ratio between faint and bright phases happened by chance, using the binomial probability distribution.

4.3 Light Curves

4.3.1 Long term light curve

In order to establish whether the source is persistently bright, we look to a long term X-ray light curve spanning several years. The data include the most recent deep *Chandra* observations of XMMU 122939.7+075333 as well as archival data from *XMM*, *Chandra* and *ROSAT*.

The flux from *Chandra* data set taken in 2000 was determined using ISIS and the spectral parameters from Shih et al. (2008). The flux for the 2004 *XMM* observation was taken from the bright phase spectrum (count rate $\geqslant 0.04$ counts/s) of XMM04 only and calculated in ISIS using the spectral parameters found in Shih et al. (2008). This was done to be consistent with the work of Shih et al. (2008) and Maccarone et al. (2010). The 2002 *XMM* (values taken from the 2*XMM* catalogue of Watson et al., 2009) and 2010 *Chandra* (Maccarone et al., 2010) fluxes and errors were calculated from their respective count rate or flux errors using the W3PIMMS tool and assuming either a $\Gamma = 1.7$ power law or a $k\mathrm{T_{in}}$=1 keV blackbody spectral model.

The *ROSAT* data (Colbert & Ptak, 2002) had poor spectral resolution and W3PIMMS was used to calculate the flux from the count rate. Shih et al. (2008) found that the count rate for the *ROSAT* data were consistent with that of the bright XMM04 data; they therefore used the XMM04 inner disk temperature value (0.2 keV)

to fit the *ROSAT* data. The *ROSAT* luminosity is a factor of 6 higher when a 1 keV blackbody temperature is assumed compared to a temperature of 0.2 keV. The errors for this source are thus dominated by the uncertain energy to counts conversion for this data. Maccarone et al. (2010) estimate that the luminosity of the source at the time of the *ROSAT* observation is between 10^{39} and 10^{40} erg s^{-1}. In this work we used to 0.2 keV blackbody to estimate the flux of the *ROSAT* data.

All the data plotted in the light curve, shown in Fig. 4.1, are the unabsorbed X-ray luminosities for the 0.2–10 keV range (see figure caption for details on errors). We find that during the period from 1994 to 2011, the source has $L_{\rm X} \gtrsim 10^{38}$ erg s^{-1}, thus meeting the criterion set out in § 4.1. In addition, the source luminosity has increased significantly between the observation of Maccarone et al. (2010) in February 2010 and the most recent observations in February 2011. This large increase in luminosity over a the period of a year argues against the idea that the long term flux variations are caused by the influence of outer star in a triple system on the inner binary. Thus the triple scenario out forward in Maccarone et al. (2010) is no longer favoured.

4.3.2 Light curves of Obs ID 12889 and 12888

The light curves for Obs ID 12889 and 12888 are used to explore the short term variation of the X-ray flux. The source displays periods of brightening (by a factor of roughly three from the mean count rate) on the timescale of hours. This intra-observational variability is too short to be due to spectral state changes, which have time scales on the order of days to weeks for stellar mass black hole binary systems (see e.g. Yu & Yan, 2009).

These variations could, however, be easily explained by a variable absorption column. The light curves for Obs ID 12889 (140 ks) and 12888 (160 ks) are shown in Fig. 4.2.These source light curves were fit with a straight line. This yielded a χ^2/ν of 35.95/34 and 68.86/40 for Obs ID 12889 and 12888 respectively. For Obs ID 12889, we find that the straight line fit to the light curve cannot be ruled out at greater than the 37 % level. We can therefore say that the source is not varying significantly over this observation. However, for Obs ID 12888, the straight line can be ruled out at greater than the 99 % level. So the source is displaying significant flux variation over this time period.

4.4 Hardness Ratios

The count rate threshold between the bright and faint phases is 1.5×10^{-3} counts/s (as indicated by the dashed horizontal lines in Fig. 4.2) . The hardness ratios for each

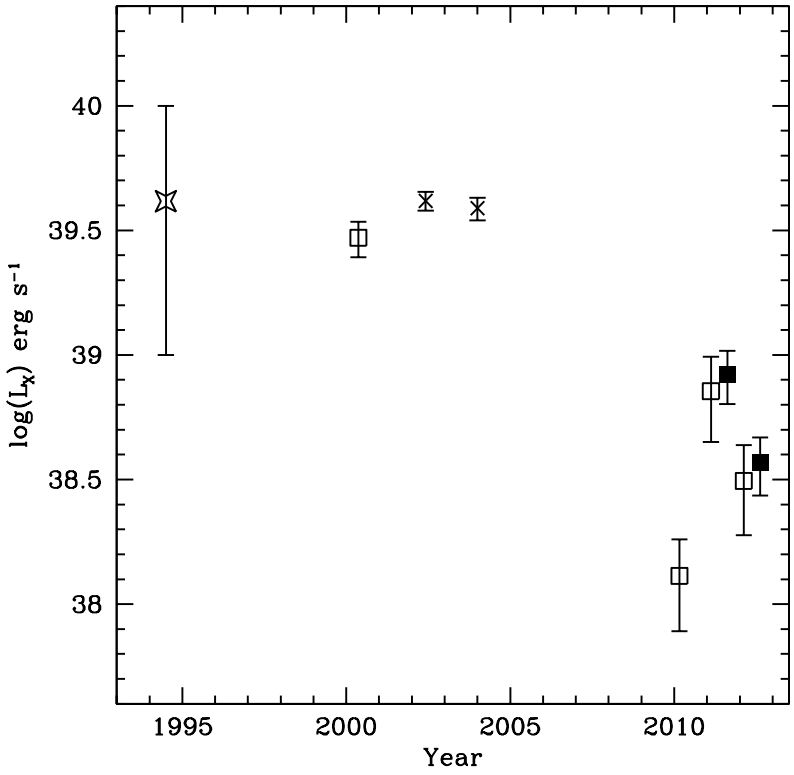

FIGURE 4.1: The long term light curve of XMMU 122939.7+075333. The squares, crosses and stars represent *Chandra*, *XMM* and *ROSAT* data respectively. The filled squares represent the bright phase *Chandra* data from Obs ID 12889 and 12888. All luminosities are in the 0.2–10 keV range. For clarity, the data points for Obs ID 12889 bright, Obs ID 12888 faint and Obs ID 12888 bright phases have been plotted with offsets of six, 12 and 18 months respectively. The errors for the *Chandra* fluxes, except those taken in 2010, as well as that of XMM04 reflect the 90 % confidence intervals. The *ROSAT*, 2002 *XMM* and 2010 *Chandra* errors were calculated from their respective count rate or flux errors using the W3PIMMS tool. The dominant source of error for the *ROSAT* luminosity is due to uncertainty in converting counts to energy (see Shih et al., 2008; Maccarone et al., 2010).

observation as a function of intensity is shown in Fig. 4.3. As stipulated in §1, we see an increase in HR as the luminosity decreases; i.e. the source gets harder as it gets fainter.

We use the binomial probability distribution to determine whether or not the change in HR between bright and faint phases is significant, with each photon simply being assigned a probability of being in the soft or hard band. In our case, the null hypothesis is that the HR of the faint phases is only different from that of the bright ones by chance (given that in the bright phases the chances of a photon falling into the hard or soft band is 50%). Hardness ratio data as well as the probabilities are displayed in Table 4.1.

We find that the null hypothesis probability for Obs ID 12888 is 0.006; thus the difference in hardness between the faint and bright phases is statistically significant.

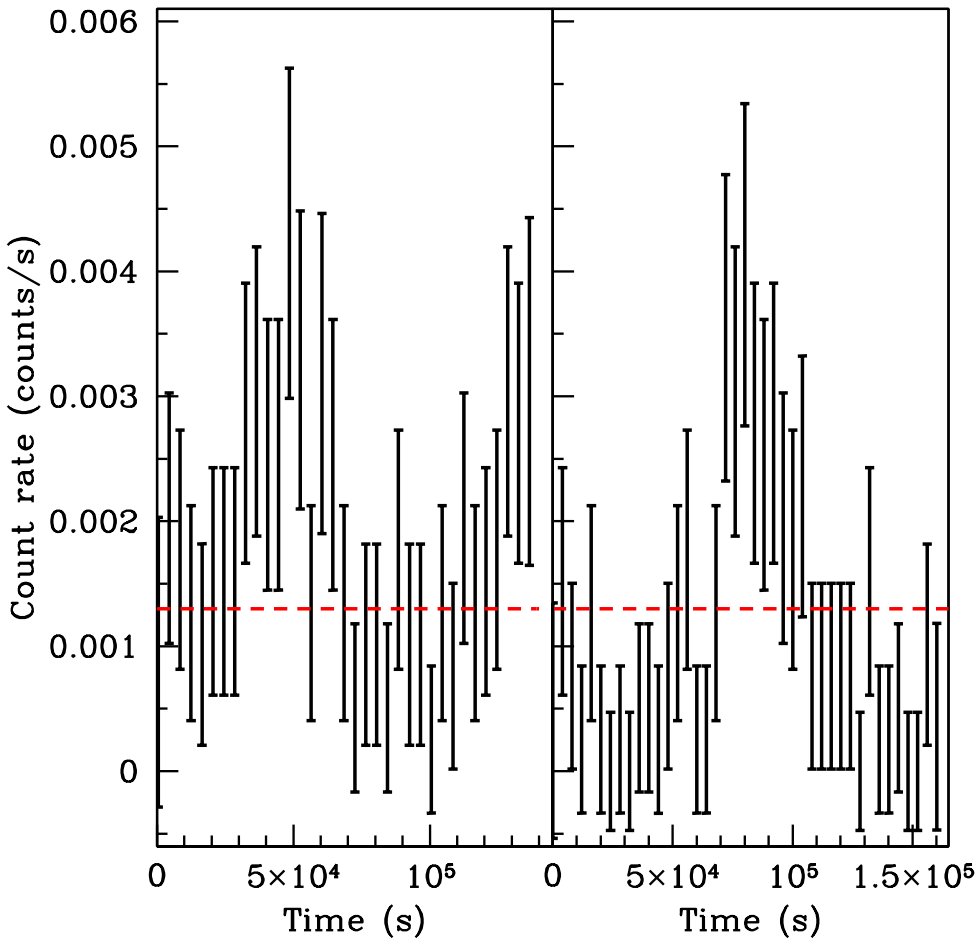

FIGURE 4.2: The 140 ks (left panel) and 160 ks (right panel) light curves of XMMU 122939.7+075333, taken a week apart, showing the brightening of the source. The dashed line indicated the count rate threshold between the faint and bright phases. The count rate is averaged over 4000 s.

This result is consistent with the explanation discussed in §1: that a variable absorption column is responsible for the decrease in X-ray luminosity due to the preferential absorption of soft X-ray photons. Shih et al. (2008) also found that the spectral changes between the faint and bright phases in XMM04 we due to a lack of soft photons in the faint phase, which is consistent with our result for Obs ID 12888.

For Obs ID 12889 the probability of 0.35 indicates that that change in HR is not significant between the phases. This is consistent with our finding in § 4.3.2. The source flux is not varying significantly over the course of Obs ID 12889 and so we do not expect to see any significant correlation between source brightness and hardness ratio.

Phase	HR	Probability
12889 bright	0.0 ± 0.08	-
12889 faint	0.06 ± 0.13	0.35
12888 bright	0.02 ± 0.11	-
12888 faint	0.38 ± 0.13	0.006

TABLE 4.1: HR values (define H and S bands and HR=H-S/H+S) and the probability column indicates the null hypothesis probability that the faint HR could be produced from a spectrum that is the same as in the bright phase for Obs ID 12889 and 12888.

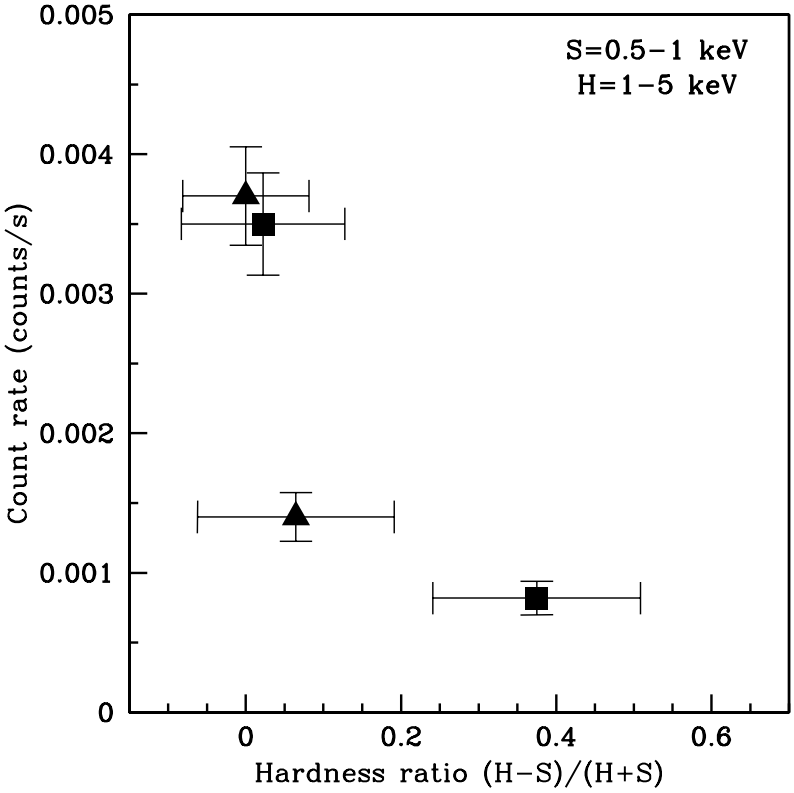

FIGURE 4.3: A hardness intensity diagram for XMMU 122939.7+075333. The triangles represent data from Obs ID 12889 and the squares represent Obs ID 12888 data. The errors shown on the data points were obtained by propagating the associated errors in the standard way. The null hypothesis probability (i.e. the probability that the HR of the faint phases is only different from that of the bright ones by chance, given that in the bright phases the chances of a photon falling into the hard or soft band is 50%) is 0.006 for Obs ID 12888 and 0.35 for Obs ID 12889. The marginally significant result for Obs ID 12888 is consistent with the Shih et al. (2008) finding that the spectral changes between the faint and bright phases in XMM04 we due to a lack of soft photons in the faint phase.

4.5 Spectral Analysis

We are unable to fit complex physical models to these spectra due to the low number of counts (98 and 66 total counts for the faint phase spectrum of Obs ID 12889 and 12888 respectively). These spectral fits are used only to parametrise the data.

4.5.1 Continuum plus Gaussian spectral model

4.5.1.1 Continuum in bright and faint phases

The continuum of both the faint and bright phases of Obs ID 12889 were better fit by single PL models than by diskbb models, but both classes provide statistically acceptable fits. Γ was found to be $3.45^{+1.66}_{-1.21}$ and $2.61^{+1.33}_{-1.33}$ for Obs ID 12889 faint and Obs ID 12889 bright respectively. The bright and faint phase continua of Obs ID 12888 were better fit by the diskbb model with inner disk temperature, $k\mathrm{T}_{in}$=$0.57^{+0.13}_{-0.24}$ and $0.47^{+1.17}_{-0.24}$ keV respectively.

If we assume that the X-ray emission of a ULX can be categorised using the emission states defined for Galactic black hole binaries, i.e. the source is in a normal, sub-Eddington accretion state, we can calculate limits on the mass of the black hole in XMMU 122939.7+075333 (e.g. Stobbart et al., 2006). The best fit values of Γ found for the Obs ID 12889 spectra are consistent with the steep PL (SPL) emission state ($\Gamma \geq 2.4$) for BHs (McClintock & Remillard, 2006). The SPL state is often associated with the X-ray luminosity of the BH binary, $\mathrm{L_X} > 0.2\mathrm{L_{Edd}}$. Using the values of $\mathrm{L_X}$ derived from the spectral fitting (see Table 4.2) and the fact that $\mathrm{L_{Edd}} = 1.3 \times 10^{38}(M/M_\odot)\,\mathrm{erg\,s^{-1}}$, we calculate that the mass of the BH should be at least $27\,\mathrm{M_\odot}$. However, because the spectral parameters are not well constrained, the values of Γ are also consistent with the hard emission state ($1.5 < \Gamma < 2.1$ McClintock & Remillard, 2006). Generally, in the hard state $\mathrm{L_X} \lesssim 0.03$ (Fender et al., 2004); implying a BH mass greater than $180\,\mathrm{M_\odot}$.

For Obs ID 12888, the spectra were better fit by a diskbb model. For the standard accretion disk, there is a relationship between the inner disk temperature, $\mathrm{T_{in}}$, the black hole mass, M and the total X-ray luminosity, $\mathrm{L_X}$, such that $\mathrm{M} \propto \mathrm{T_{in}^{-2}\,L_X^{1/2}}$ (Feng & Soria, 2011, and references therein). Galactic stellar mass BHs with $\mathrm{M}=10\,\mathrm{M_\odot}$ typically have $\mathrm{T_{in}} \sim 1\,\mathrm{keV}$ (with a range of 0.7–1.5 kev McClintock & Remillard, 2006) and $\mathrm{L_X} \sim 10^{38}\,\mathrm{erg\,s^{-1}}$. The typical parameter ranges for ULXs are $10^{39} < \mathrm{L_X} < 10^{40}\,\mathrm{erg\,s^{-1}}$ and $0.1 < \mathrm{T_{in}} < 0.4\,\mathrm{keV}$, implying a BH mass range of $200 < \mathrm{M} < 10^4\,\mathrm{M_\odot}$. For the bright Obs ID 12888 spectrum, the best fit values of $\mathrm{T_{in}}$ and $\mathrm{L_X}$ suggest BH masses of 60–80 $\mathrm{M_\odot}$. However, as $\mathrm{T_{in}}$ is poorly constrained in the case of the faint spectrum, the BH mass could be as high as $390\,\mathrm{M_\odot}$.

Spectrum	Model	χ^2/ν	Γ	T_{in} (keV)	Line energy (keV)	PW (keV)	EW (keV)	L_X (10^{38} erg s^{-1})
12889 faint	PL	2.75/7	$3.45^{+1.66}_{-1.21}$	–	–	–	–	$7.16^{+2.68}_{-2.68}$
12889 bright	PL + Gaussian	3.83/4	$2.61^{+1.33}_{-1.33}$	–	$0.62^{+0.05}_{-0.31}$	$0.05^{+0.10}_{-0.05}$	0.92	$8.36^{+2.05}_{-2.01}$
12888 faint	diskbb	0.48/3	–	$0.47^{+1.17}_{-0.24}$	–	–	–	$3.12^{+1.23}_{-1.23}$
12888 bright	diskbb + Gaussian	0.10/2	–	$0.57^{+0.13}_{-0.24}$	$0.65^{+0.04}_{-0.21}$	$0.05^{+0.10}_{-0.05}$	2.1	$3.70^{+0.96}_{-0.97}$

TABLE 4.2: The best fit spectral parameters for the faint and bright phases of Obs ID 12889 and 12888 using the continuum plus Gaussian spectral model. The errors shown are the 90% confidence intervals. The luminosity is for the range 0.2–10 keV. PW and EW are the physical and equivalent widths for the emission line, respectively

These mass estimates are based on the assumption that the source is in a sub-Eddington accretion state. However, most ULXs are now thought to be accreting at super-Eddington rates (e.g. Gladstone et al., 2009). The interpretation of the continuum spectrum of a ULX must therefore be different. For instance, it is thought that the cool disk-like components in ULX spectra are due to a disk wind blown from the super-Eddington disk by its high radiation pressure (e.g. Kajava & Poutanen, 2009).

4.5.1.2 Gaussian component in bright and faint phases

Both bright phase spectra are better fit when a Gaussian component is included in the spectral model to account for the excess of soft photons at approximately 0.6 keV. The Gaussian component energy is $0.62^{+0.05}_{-0.31}$ for Obs ID 12889 bright phase and $0.65^{+0.04}_{-0.21}$ for Obs ID 12888 bright phase. The physical and equivalent widths for the line are $0.05^{+0.10}_{-0.05}$ keV and 0.92 keV respectively for the bright Obs ID 12889 spectrum. The physical width (PW) and equivalent width (EW) for the bright Obs ID 12888 spectrum are $0.05^{+0.10}_{-0.05}$ keV and 2.1 keV respectively. The line luminosity is $\sim 10^{38}$ erg s^{-1} for both spectra. Neither of the faint phase spectra required the Gaussian component in order to have acceptable fits.

The energies for Gaussian component found in both the PL and diskbb models are consistent with emission from highly ionised oxygen, O VIII, with line energy of 0.65 keV. The O VIII edge absorption feature is located at 0.87 keV. We have not attempted to model this feature due to the low signal-to-noise of the data, but cannot rule out its presence. However, because the fitted emission lines are strong and narrow, the absence or presence of the absorption edge should not affect whether the emission line is detected. In the next section, we test the significance of the Gaussian component.

The best fit spectral parameters for all bright and faint phase spectra are summarised in Table 4.2. The unfolded bright and faint spectra and χ^2 residuals are shown in Fig. 4.4.

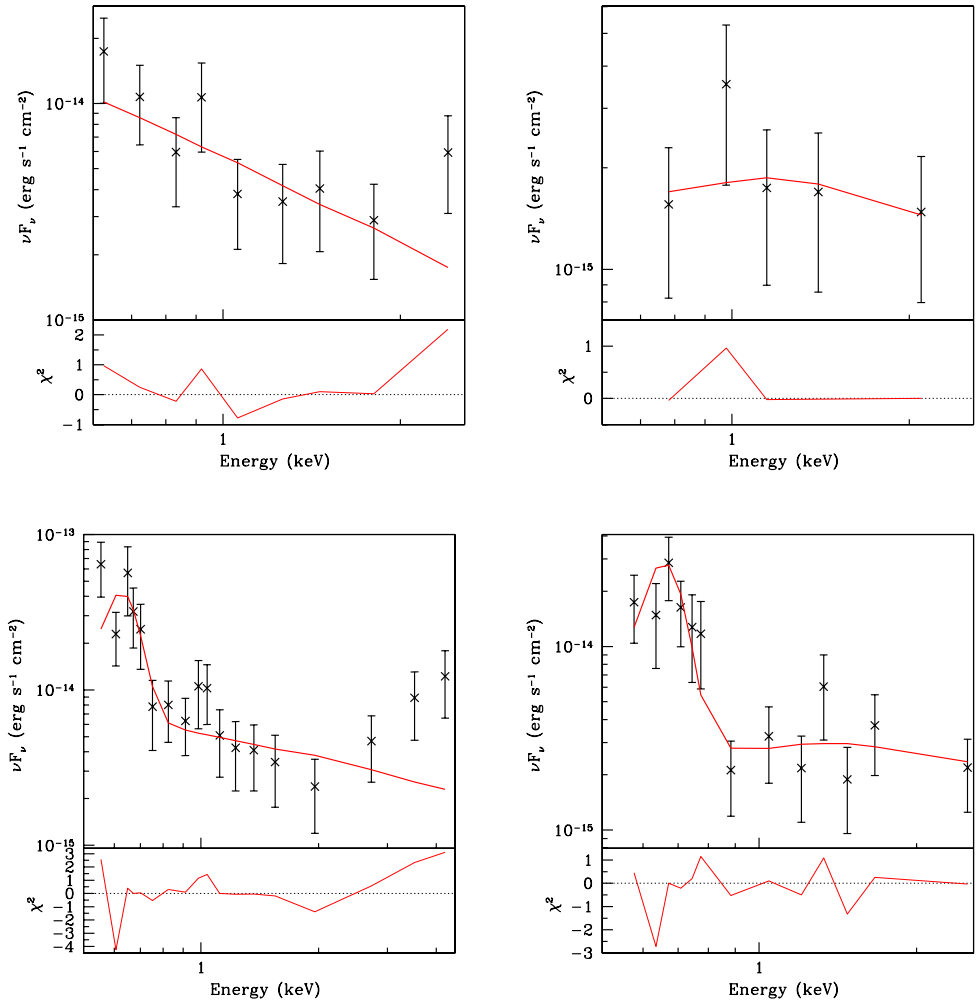

FIGURE 4.4: The bright and faint unfolded spectra of XMMU 122939.7+075333 taken from Obs ID 12888 and 12889 with their respective best fit continuum plus Gaussian model (red line; see Table 4.2 for spectral model fit parameters). The top left panel shows the faint Obs ID 12889 spectrum, the top right panel shows the faint Obs ID 12888 spectrum, the bottom left panel shows the bright Obs ID 12889 spectrum and the bottom right panel shows the bright Obs ID 12888 spectrum. The χ^2 residual values are shown below each spectrum.

4.5.1.3 Joint fits

For the joint fit of Obs ID 12889, 12888 and XMM04 we compared the diskbb or PL continuum model with and without the Gaussian component. We then tested the significance of the line component using an F test.

For the model consisting of a diskbb continuum only, the inner disk temperatures were $0.26^{+0.13}_{-0.08}$ keV, $0.47^{+1.38}_{-0.23}$ and $0.32^{+0.04}_{-0.04}$ keV for Obs ID 12889, 12888 and XMM04 respectively. When the Gaussian component was added to the diskbb continuum model, the inner disk temperature, T_{in} for Obs ID 12889, 12888 and XMM04 were found to be $0.30^{+0.22}_{-0.08}$ keV, $0.73^{+2.44}_{-0.42}$ keV and $0.37^{+0.11}_{-0.05}$ keV respectively. An emission

line component with a line energy of $0.66^{+0.01}_{-0.04}$ keV was found. In this fit, the line width was restricted to 0−0.04 keV and a PW of 6.19×10^{-5} was found. The EWs for Obs ID 12889, 1288 and XMM04 are 0.85 keV, 0.17 keV and 0.10 keV respectively. The reduced χ^2 is 0.88 for the diskbb only model and 0.76 for the Gaussian plus diskbb model. The F test revealed that the emission line is significant, with an F statistic of 8.24 and null hypothesis probability of 4.58×10^{-5}.

The PL continuum only model yielded the following spectral parameters for Obs ID 12889, 12888 and XMM04 respectively: $3.46^{+0.92}_{-0.55}$, $2.75^{+1.45}_{-1.08}$ and $2.71^{+0.21}_{-0.21}$. When the Gaussian component was included in the model, an emission line with an energy of $0.66^{+0.02}_{-0.02}$ keV and a PW of 1.92×10^{-6} $^{+0.04}_{-1.92\times10^{-6}}$ keV was found. The spectral parameters for the continuum for this model are $3.10^{+0.93}_{-0.83}$, $2.30^{+1.06}_{-0.82}$ and $2.54^{+0.24}_{-0.22}$ for Obs ID 12889, 12888 and XMM04 respectively. The EWs are 0.32 keV, 0.10 keV and 0.07 keV for Obs ID 12889, 12888 and XMM04 respectively. The PL only model has a χ^2 of 0.73 whereas the Gaussian plus PL model had a reduced χ^2 of 0.66. The F test results show that the line is significant; the F statistic is 5.91 and the null hypothesis probability is 8.22×10^{-4}.

The Gaussian component is thus highly significant. In both joint fits, the Gaussian component is narrow and unresolved. The emission line seen here is unlikely to be due to reflection from the accretion disk because it is so luminous (see Madej et al., 2010, who find a 40 eV emission line from a Galactic ultracompact X-ray binary.). The emission could, however be caused by either collisional excitation or photoionisation. Due to the low signal-to-noise ratio of our data, we are not able to draw further conclusions about the origin of this spectral feature, except to say that it is consistent with the model that the companion star is a WD.

These results provide strong evidence for soft X-ray line emission from a ULX. We argue that this line emission arises from highly ionised oxygen, which bolsters our theory that the accretion disk of XMMU 122939.7+075333 is rich in oxygen due to the companion star being a WD.

Other ULXs also show soft, line-like X-ray emission. For instance, Caballero-García & Fabian (2010) found that the spectra of NGC 5408 X1 contained line-like emission at ~ 0.6 keV. They suggested that this emission could be due to the presence of highly ionised oxygen and iron around the source. Subsequently, Middleton et al. (2011) showed that this feature is well modelled by an optically thin plasma model component with temperature ~ 0.8 keV. NGC 5204 X-1 was found to have an excess of counts at around 1 keV (Roberts et al., 2006). It was found that this excess could be modelled either as a thermal plasma component with $k\mathrm{T} \sim 0.9$ keV or as a broad Gaussian line with $k\mathrm{T} \sim 0.96$ keV. Stobbart et al. (2006) found that the soft excess in NGC 4395 X-1 could be modelled as a thermal plasma with $k\mathrm{T} = 0.75$ keV.

Emission line excluded				Emission line included			
	Data set				Data set		
Parameter	12889	12888	XMM04	Parameter	12889	12888	XMM04
norm.	$0.36^{+2.22}_{-0.31}$	$0.01^{+1.45}_{-0.01}$	$0.25^{+0.18}_{-0.11}$	norm.	$0.16^{+1.03}_{-0.15}$	$1.63^{+1480}_{-1.62}\times10^{-3}$	$0.12^{+0.11}_{-0.08}$
T_{in} (keV)	$0.26^{+0.13}_{-0.08}$	$0.47^{+1.38}_{-0.23}$	$0.32^{+0.04}_{-0.04}$	T_{in} (keV)	$0.30^{+0.22}_{-0.08}$	$0.73^{+2.44}_{-0.42}$	$0.37^{+0.11}_{-0.05}$
				EW (keV)	0.85	0.17	0.10
χ^2/ν	118.4/134			χ^2/ν	99.6/131		
F statistic value: 8.24				Null hypothesis probability: 4.58×10^{-5}			

TABLE 4.3: The best joint fit diskbb spectral parameters for Obs ID 12889, 12888 and XMM04. The errors shown are the 90% confidence intervals. The PW was restricted to 0−0.04 keV. The emission line energy is $0.66^{+0.01}_{-0.04}$ keV and the PW is 6.19×10^{-5} keV.

Emission line excluded				Emission line included			
	Data set				Data set		
Parameter	12889	12888	XMM04	Parameter	12889	12888	XMM04
norm. ($\times10^{-6}$)	$8.34^{+1.81}_{-1.92}$	$3.71^{+1.16}_{-1.32}$	$14.1^{+1.3}_{-1.3}$	norm. ($\times10^{-6}$)	$7.70^{+1.92}_{-2.15}$	$3.22^{+1.23}_{-1.20}$	$13.0^{+1.4}_{-1.4}$
Γ	$3.46^{+0.92}_{-0.55}$	$2.75^{+1.45}_{-1.08}$	$2.71^{+0.21}_{-0.21}$	Γ	$3.10^{+0.93}_{-0.83}$	$2.30^{+1.06}_{-0.82}$	$2.54^{+0.24}_{-0.22}$
				EW (keV)	0.32	0.10	0.07
χ^2/ν	98.2/134			χ^2/ν	86.5/131		
F statistic value: 5.91				Null hypothesis probability: 8.22×10^{-4}			

TABLE 4.4: The best joint fit PL spectral parameters for Obs ID 12889, 12888 and XMM04. The errors shown are the 90% confidence intervals. The emission line energy is $0.66^{+0.02}_{-0.02}$ keV and the line width is $1.92\times10^{-6}\ ^{+0.04}_{-1.92\times10^{-6}}$ keV.

These spectra also show hints of other features besides the excess at 0.65 keV. Both the Obs ID 12889 and 12888 spectra show suggestive evidence for a hard (>2 keV) excess. Shih et al. (2008) also report a hard excess in in their spectral analysis of the source. This feature may require an additional continuum component in order to fit properly. However, our data do not have enough counts to do this without increasing the degeneracy of the model significantly. There also appears to be an excess of photons at ∼1 keV in the *Chandra* and *XMM* spectra. Narrow spectral features have been seen at these energies for LMC X-4 (Neilsen et al., 2009; Hung et al., 2010). The narrow feature arises from emission from Ne X Lyα (1.02 keV).

The spectral parameters for both the diskbb and PL models and the F test results are are summarised in Table 4.3 and Table 4.4 respectively. The spectra for these joint fits are shown in Fig. 4.5 and Fig. 4.6.

4.5.2 Disk blackbody plus power law spectral model

Roberts et al. (2006); Stobbart et al. (2006) and Roberts (2007) showed that some of the ULX spectra they studied could be modelled using the standard disk blackbody plus power law model used to model the spectra of Galactic binaries, i.e. the soft end of the spectrum was fit by the diskbb component and the hard end was fit by the PL. However, Stobbart et al. (2006) also found that a significant proportion of their sources

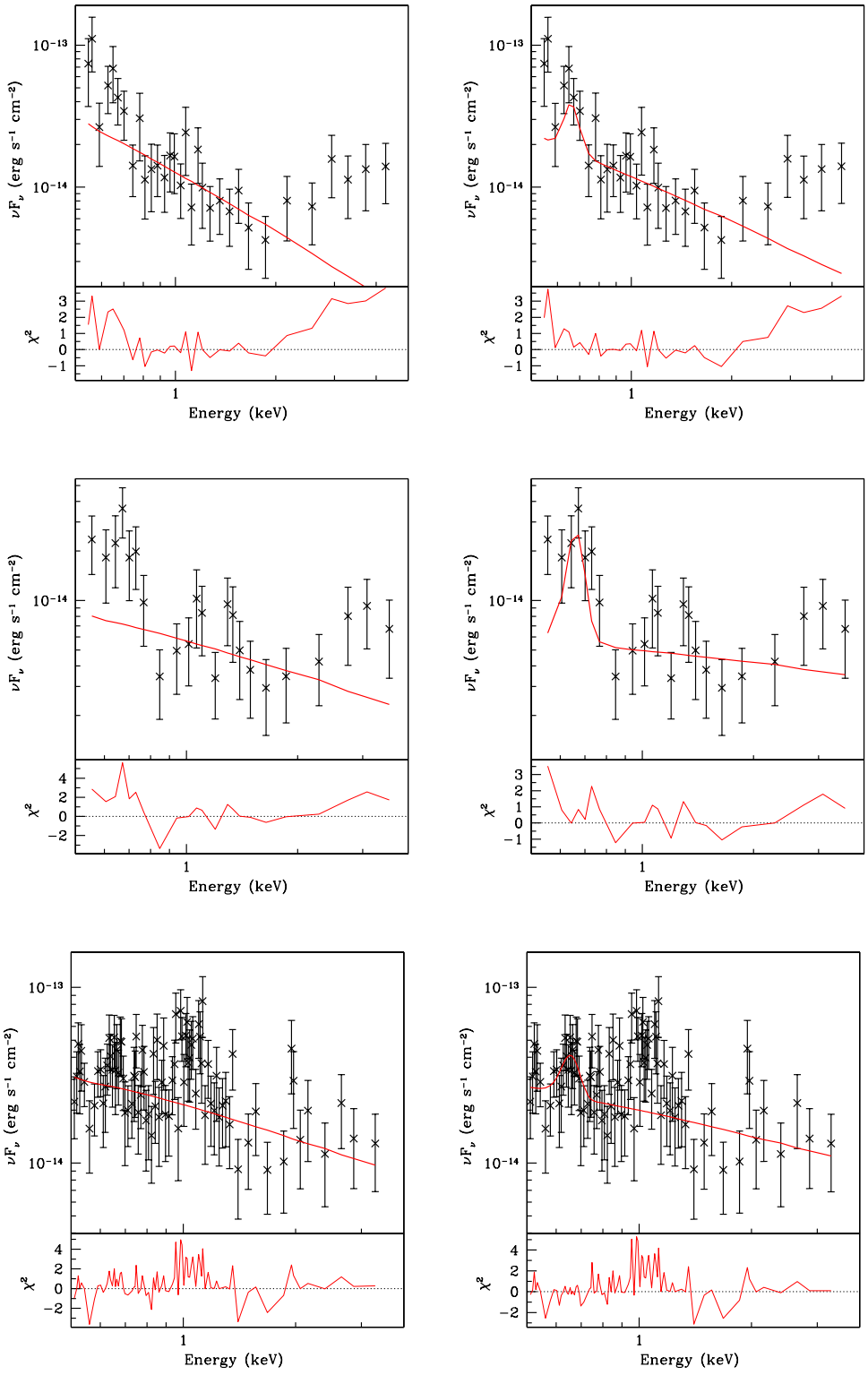

FIGURE 4.5: The unfolded spectra of XMMU 122939.7+075333 taken from Obs ID 12888 and 12889 and XMM04 with a PL continuum model (red line; see Table 4.4 for spectral model fit parameters). The panels on the left hand side show spectra fit without the Gaussian component and the panels right show spectra fit with the Gaussian component. The top panels show the Obs ID 12889 spectra, the middle panels shows the Obs ID 12888 spectra and the bottom panels show the XMM04 spectra. The χ^2 residual values are shown below each spectrum.

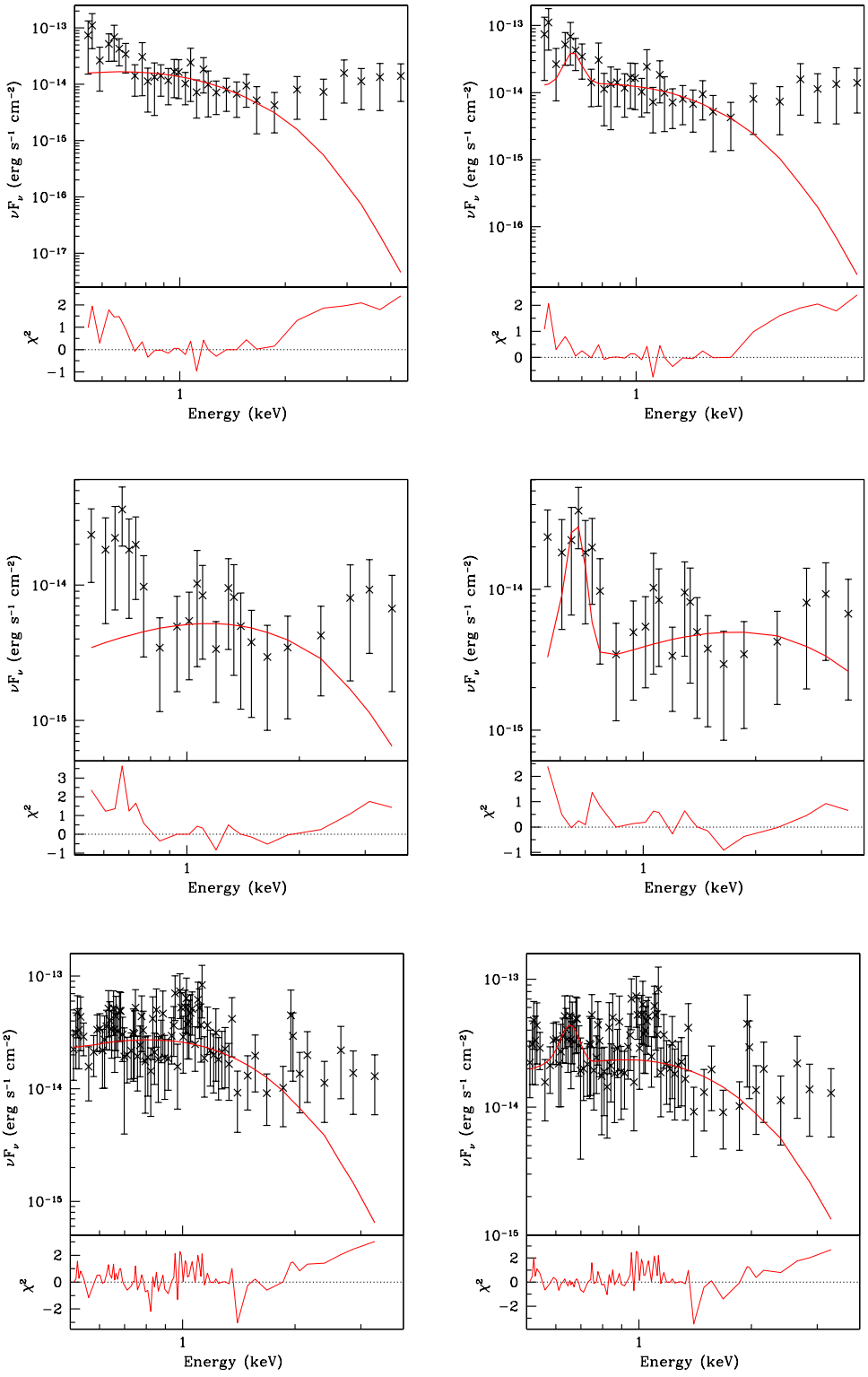

FIGURE 4.6: The unfolded spectra of XMMU 122939.7+075333 taken from Obs ID 12888 and 12889 and XMM04 with a diskbb continuum model (red line; see Table 4.3 for spectral model fit parameters). The panels on the left hand side show spectra fit without the Gaussian component and the panels right show spectra fit with the Gaussian component. The top panels show the Obs ID 12889 spectra, the middle panels shows the Obs ID 12888 spectra and the bottom panels show the XMM04 spectra. The χ^2 residual values are shown below each spectrum.

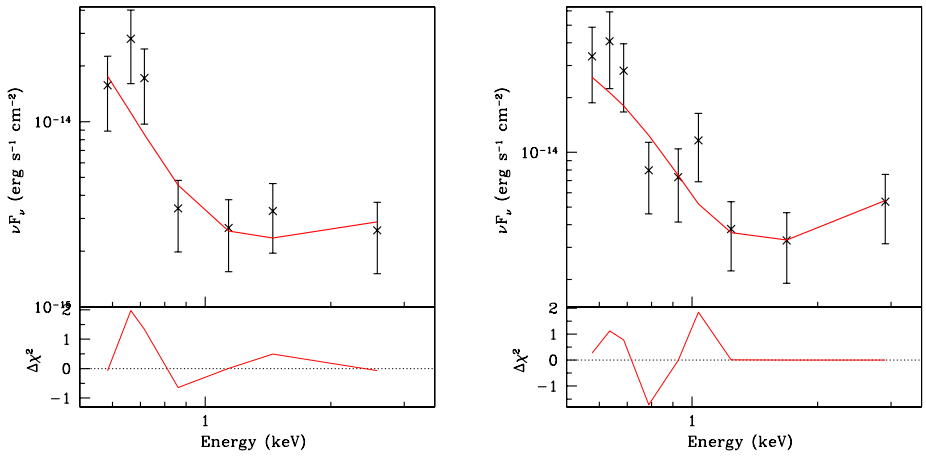

FIGURE 4.7: The bright unfolded spectrum of XMMU 122939.7+075333 taken from Obs ID 12888 (left panel) and 12889 (right panel) with their respective best fit diskbb plus PL model (red line; see Table 4.5 for spectral model fit parameters). The χ^2 residual values are shown below the spectrum.

had spectra that were better fit with an "inverted" model, i.e. a steep PL component fit to the soft end of the spectrum and diskbb component fit for the harder end. In this section we explore whether the disk plus power law model provides a good fit to the spectra of XMMU 122939.7+075333.

4.5.2.1 Bright phase spectra

The bright phase of Obs ID 12888 and 12889 were individually fit with a diskbb plus PL model. For Obs ID 12888, the disk component has an inner temperature, $0.08^{+0.06}_{-0.01}$ keV and the PL component is $\Gamma = 2.06^{+1.50}_{-1.42}$. These parameters are consistent with the system having a cool disk and hard power law component (see e.g. Stobbart et al., 2006). However, while this model produced an acceptable fit to the data with $\chi^2/\nu = 4.49/3$, the fit was much poorer than for the continuum plus Gaussian component model where $\chi^2/\nu = 0.10/2$.

For Obs ID 12889, the bright phase spectrum was best fit with $T_{in} = 0.09^{+0.02}_{-0.03}$ and $\Gamma = 1.80^{+1.87}_{-1.31}$. These parameters are consistent with the source having a cool disk and hard PL component (see e.g. Stobbart et al., 2006). The fit is acceptable ($\chi^2/\nu = 4.9/5$), but not superior to the continuum plus Gaussian component fit ($\chi^2/\nu = 3.83/4$). Thus the diskbb plus PL model is only a viable alternative for Obs ID 12889. The best fit value for T_{in} is low and, using the best fit value L_X, implies a high BH mass of $\sim$7700 $M_\odot$. The results of the spectral fitting are summarised in Table 4.5. The unfolded bright phase spectra are shown in Fig. 4.7.

Spectrum	Model	χ^2/ν	Γ	T_{in} (keV)	L_X (10^{38} erg s^{-1})
12889 bright	diskbb + PL	4.89/5	$1.80^{+1.87}_{-1.31}$	$0.09^{+0.02}_{-0.03}$	$28.4^{+6.93}_{-6.92}$
12888 bright	diskbb + PL	4.49/3	$2.06^{+1.50}_{-1.42}$	$0.08^{+0.06}_{-0.01}$	$16.7^{+4.67}_{-4.68}$

TABLE 4.5: The best fit spectral parameters for the bright phases of Obs ID 12889 and 12888 using the diskbb plus PL spectral model. The luminosity is for the range 0.2–10 keV. The errors shown are the 90% confidence intervals.

Spectrum	χ^2/ν	norm.	T_{in} (keV)	norm. $\times 10^{-6}$	Γ
Obs ID 12888	8.51/19	$225.2^{+5644}_{-222.1}$	$0.09^{+0.02}_{-0.04}$	$1.99^{+1.69}_{-1.32}$	$1.45^{+1.29}_{-1.06}$
Obs ID 12889	9.99/28	$29.0^{+24085}_{-28.3}$	$0.12^{+0.03}_{-0.06}$	$2.76^{+4.50}_{-2.28}$	$1.28^{+1.20}_{-0.96}$
XMM04	61.1/81	$0.55^{+3.94}_{-0.30}$	$0.26^{+0.06}_{-0.07}$	$1.79^{+18626450}_{-1.72}$	$0.60^{+1.92}_{->2.60}$

TABLE 4.6: The best fit spectral parameters for Obs ID 12889, 12888 and XMM04 using the diskbb plus PL spectral model. The errors shown are the 90% confidence intervals.

4.5.2.2 Obs ID 12889 and 12888 and XMM04 full spectra

The disk blackbody plus power law model produced acceptable fits for all three data sets. We note that for our spectra the PL slopes are not well constrained, especially for XMM04. Nevertheless, all three sets of spectral fit parameters were consistent with the source having a cool disk and hard PL component. T_{in} was found to be $0.09^{+0.02}_{-0.04}$, $0.12^{+0.03}_{-0.06}$ and $0.26^{+0.06}_{-0.07}$ for Obs ID 12888, 12889 and XMM04 respectively. The PL slopes were $\Gamma = 1.45^{+1.29}_{-1.06}$, $\Gamma = 1.28^{+1.20}_{-0.96}$ and $\Gamma = 0.60^{+1.92}_{->2.60}$ for Obs ID 12888, 12889 and XMM04 respectively. These parameters are summarised in Table 4.6 and the spectra are shown in Fig. 4.8.

These parameter values are in keeping with the results found for other ULXs (see e.g. Miller et al., 2003; Jenkins et al., 2005; Roberts et al., 2005; Stobbart et al., 2006). The diskbb plus PL model has fit the apparent hard excess much better than the previous models that only include one continuum component (see e.g. Fig. 4.3). We note that the apparent excess of photons at around 1 keV still remains, even with this two continuum component model. The disk blackbody plus power law model therefore provides a good fit to the spectra of XMMU 122939.7+075333, implying that the source is behaving like a typical ULX.

Since the standard ULX spectral model gives statistically acceptable fits to the spectra of XMMU 122939.7+075333, we cannot say that the line plus continuum spectral modelled is preferred over the standard ULX model. We can therefore not distinguish between the scenario where the soft excess is due to highly ionised oxygen or a cool disk component, using these data sets.

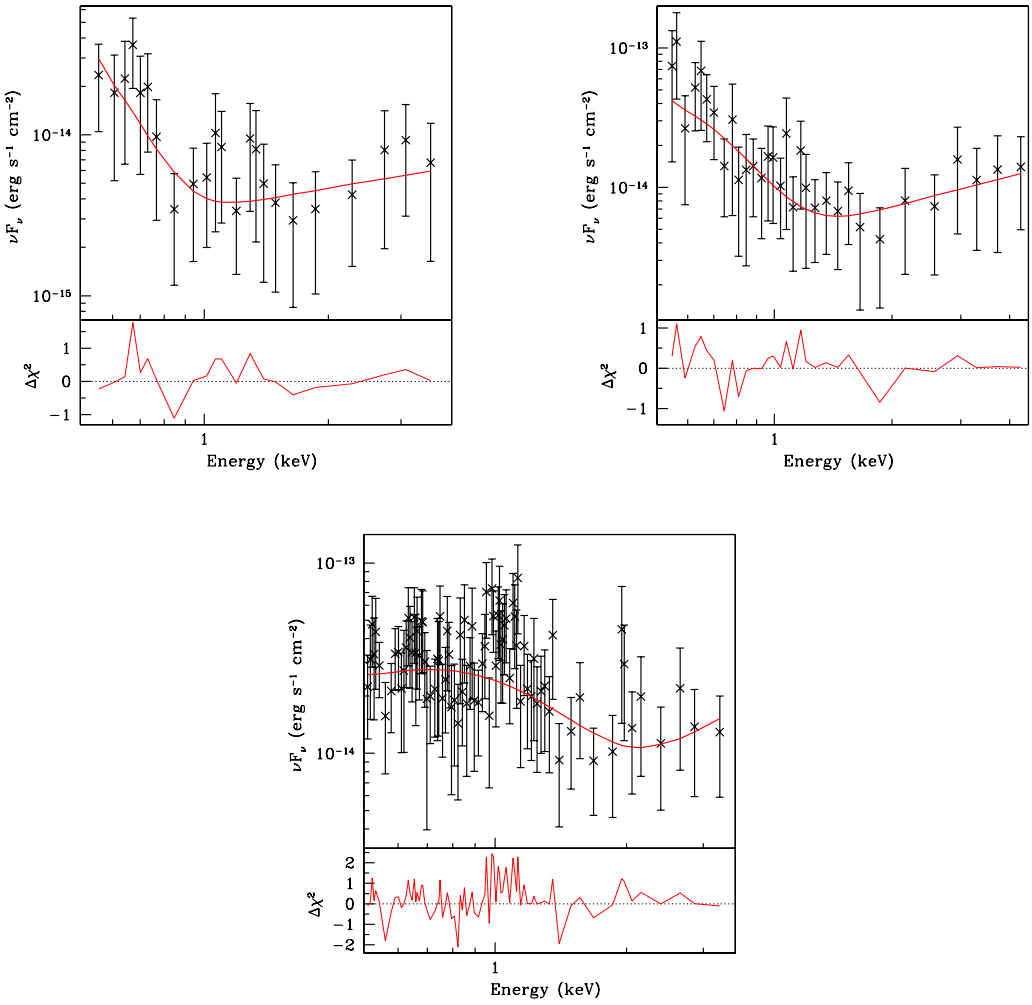

FIGURE 4.8: The unfolded spectra of XMMU 122939.7+075333 taken from Obs ID 12888 (top left panel) and 12889 (top right panel) and XMM04 (bottom panel) with a diskbb plus PL model (red line; see Table 4.5.2 for spectral model fit parameters). The χ^2 residual values are shown below each spectrum.

4.5.3 Varying absorption model

We assume that the difference between the bright and faint phases in Obs ID 12888 and 12889 are due to a variable absorption column, i.e. the underlying continuum is essentially the same and the difference in flux is due to the soft photons being preferentially absorbed in the faint phase. We can test this assumption further by fitting the faint phase spectra using the best fit continuum spectral parameters from the respective bright phase spectra and leaving the absorption free to vary. If our assumption is correct, then the fits should be statistically acceptable and the absorption column should be higher than the Galactic foreground value.

We found that this model provided statistically acceptable fits for both faint spectra. The absorption component of the faint spectrum of Obs ID 12889 was found

to be consistent with zero, with the 90% confidence interval $0 < n_{\rm H} < 1.8 \times 10^{21}\,{\rm cm}^{-2}$ and a best fit value of $3.1{\times}10^{17}\,{\rm cm}^{-2}$. This is consistent with the results of the HR analysis as well as the flux variation for Obs ID 12889. All these results taken together then imply that during this observation, the source did not undergo any significant variation in flux, hardness ratio or absorption column density between the bright and faint phase.

The faint phase spectrum of Obs ID 12888 was found to have a higher absorption value of $2.5{\times}10^{21}\,{\rm cm}^{-2}$ and a 90% confidence interval of $1.6 \times 10^{20} < n_{\rm H} < 9.6 \times 10^{21}\,{\rm cm}^{-2}$. This result is in accord with the findings of the flux variation analysis as well as the HR calculations. It therefore appears that over the course of Obs ID 12888, the source did undergo significant variations in flux, HR and absorption column density between the faint and bright phase. Shih et al. (2008), using bright and faint phase spectra from XMM04, also found that the faint phase could be well modelled by using the best fit spectral parameters for the bright phase and letting the absorption column be free to vary. They found a significantly increased value of nH with this model.

4.6 Conclusions

In this chapter we have shown that XMMU 122939.7+075333 appears to be a persistently luminous X-ray source. The short term, intra-observational flux variability is too rapid to be caused by spectral state changes and can more easily be explained by a changing absorption column. The significant increase in luminosity over a the period of a year (2010 to 2011) is not consistent with the idea that XMMU 122939.7+075333 is a triple system with an inner WD-BH binary.

We also show that source has an excess of soft photons when the source is in a bright phase, which is consistent with previous analysis carried out on this system. The excess of soft X-ray photons can be modelled as emission from O VIII (0.65 keV) from the source. However, the standard spectral model (disk blackbody plus power law component) also gives acceptable fits to the data. Both sets of spectral models suggest that XMMU 122939.7+075333 is indeed BH binary. However, we do not have sufficient evidence to prefer one over the other.

Chapter 5

A Variable Black Hole X-Ray Source in a NGC 1399 Globular Cluster

Declaration

This chapter is based on a published paper of which I am not the first author. I did not write most of the text for the paper. My contribution was primarily in the form of data reduction and analysis. In particular, I wrote paragraphs two and three in §2.3. I analysed the Chandra data set 319, produced Fig. 5.2 and contributed towards the scientific conclusions about the system under investigation by carrying out the spectral analysis on the data. For the purposes of my thesis, I produced and included Fig. 5.3. I also edited and augmented the existing text to create § 5.3.1 and § 5.4.

5.1 Introduction

The high spatial resolution of X-ray telescopes such as *Chandra* and *XMM*-Newton has led to the discovery of large populations of resolved X-ray sources around nearby galaxies. The vast majority of the point sources observed in elliptical galaxies are believed to be low-mass X-ray binaries (LMXBs). Recent studies have established that roughly 40% of these LMXBs are associated with globular clusters (e.g. Kundu et al., 2007; Sivakoff et al., 2007). This over-abundance of LMXBs in globular clusters (GCs), that typically account for less than ∼0.1% of the stellar mass of a galaxy, reflects the importance of stellar dynamical interactions in the dense inner regions of clusters that leads to the enhanced formation of close binaries.

This raises the interesting question of whether some of these LMXBs may possess black hole (BH) accretors. There is much interest in BHs residing in GCs in part because it is often suggested that GCs are among the most likely hosts of intermediate mass black holes (IMBHs), due to the high stellar densities in their central regions (see e.g. Miller & Hamilton, 2002; Maccarone, 2004, and references therein). It is thought that IMBHs in GCs could form via the merger of less massive BHs or that an initially smaller BH increases its mass through accretion from the surrounding dense stellar environment (Miller & Hamilton, 2002). IMBHs could also form from the merger of many massive stars into one very massive star which then collapses into a BH (Portegies Zwart & McMillan, 2002; Gürkan et al., 2004).

On the other hand there have also been suggestions that most black holes are ejected from GCs due to dynamical processes (Sigurdsson & Hernquist, 1993; Kulkarni et al., 1993). The BHs are more massive than a typical cluster star (m$\sim$1 $M_{\odot}$). Thus when the BHs come into energy equipartition with the stars of the cluster, they quickly slow down and settle in to the core of the GC. Once there, the BHs form multiple BH systems. The subsequent dynamical interactions of these binary, triple and quadruple BH systems will cause individual BHs to be flung from the cluster.

One way to detect a black hole in a GC is to search for a characteristic X-ray signature if the BH happens to be accreting from a nearby companion. So far no such accreting BHs have been observed in any of the globular clusters in the Milky Way. But *Chandra* and *XMM* observations have identified a number of GCs in nearby galaxies that host LMXBs that are brighter than the Eddington luminosity for an accreting neutron star (Angelini et al., 2001; Kundu et al., 2002; Kim et al., 2006b). However these bright sources may also represent the superposition of many neutron star LMXBs (e.g. Angelini et al., 2001; Kundu et al., 2007) in globular clusters. Detection of rapid X-ray variability in such sources may be the only definitive way to confirm a black hole accretor with present instruments (e.g. Kalogera et al., 2004).

Maccarone et al. (2007) previously discovered the first black hole accretor in a GC through X-ray variability in RZ 2109, a globular cluster in the bright Virgo cluster galaxy NGC 4472 (see also Shih et al., 2008; Zepf et al., 2008; Maccarone et al., 2010). The identification of a single such candidate opened up many intriguing questions about the ubiquity of such systems. It is possible that the discovery of a BH in the globular cluster RZ 2109 owes to an extraordinarily fortuitous set of circumstances. In this chapter we demonstrate the presence of a black hole in a second extragalactic globular cluster in NGC 1399 through variability in the X-ray flux of a luminous accretor.

NGC 1399 is the giant elliptical galaxy at the centre of the Fornax Cluster. It has a rich and well-studied globular cluster system (e.g. Grillmair et al., 1999; Dirsch et al., 2003) with a bimodal GC metallicity distribution that is typical in such galaxies

(e.g. Kundu & Whitmore, 2001). Many joint optical and X-ray studies of NGC 1399 have showed that it has one of the highest fractions of LMXBs associated with GCs of any galaxy studied to date. As in other galaxies metal-rich clusters are more likely to host LMXBs than metal-poor ones (Angelini et al., 2001; Kim et al., 2006b; Kundu et al., 2007). We describe below the discovery of a black hole in one of the luminous GCs in this galaxy.

5.2 Observations and Results

5.2.1 X-rays

NGC 1399 has been observed multiple times by both the *Chandra* and *XMM*-Newton observatories in the past decade (Table 5.2). This provides an unique opportunity to trace X-ray activity in LMXBs, and in particular those associated with GCs for the purpose of this study.

We downloaded the archival *Chandra* and *XMM*-Newton data of NGC 1399 listed in Table 5.2 and processed it following standard data reduction guidelines using `CIAO v4.0` and `SAS v8.0`, respectively. Intervals of high background were filtered out from the data, and all images were corrected for exposure and vignetting. We adopted the wavelet method of source detection to identify point sources.

We discovered that one of the candidate LMXBs observed during the course of *Chandra* observation 319 displayed rapid X-ray variability on the timescale of ∼10 ks (Fig. 5.1). A literature search reveals that this source has been observed by *ROSAT*-HRI multiple times between 1993 and 1997 and is also listed in the 2*XMM* catalogue as 2*XMM* J033831.7-353058:042943 (Paolillo et al., 2002; Liu & Bregman, 2005; Watson et al., 2009). This object was also identified in Kundu et al. (2007) as X-ray source number 157, CXOKMZJ033831.7-353058 (hereafter, the source). The 5.4×10^{38} ergs s^{-1} X-ray luminosity derived using the average count rate of the source through the entire *Chandra* observation is brighter than the Eddington luminosity of an accreting neutron star (also see §2.4.1 below), suggesting that this may be a black hole candidate. However the source lies outside the HST image of the inner region analysed in Kundu et al. (2007). Thus, we turn to other data sets to check whether this object is associated with a globular cluster.

5.2.2 Optical counterpart

We downloaded F606W band HST-ACS images of NGC 1399 from the archive (HST GO proposal 10129) and created an aligned mosaic of the nine independent pointings of the region around the galaxy. We used the Multidrizzle routine based on the drizzle

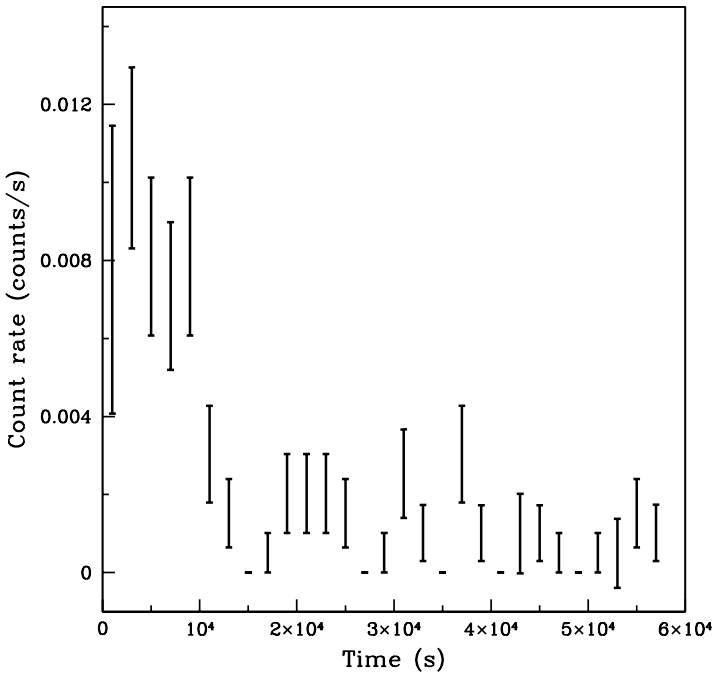

FIGURE 5.1: The *Chandra* ACIS-S3 binned light curve of the globular cluster X-ray source in NGC 1399 from the 2000-1-18 Obs ID 319 observations. Photons in the energy 0.3 to 8.0 keV are included and the count rate is averaged over 2000 s.

code of Fruchter & Hook (2002) for this purpose, taking into account the small errors in the default header values. We aligned the HST mosaic to the USNO-A2.0 astrometric system (Monet & et al., 1998). Next we identified the point sources corresponding to the spectroscopically confirmed GCs studied by Dirsch et al. (2004). The location of the GCs in the HST mosaic image was used to derive more secure positions for these objects. Finally we spatially aligned the X-ray and optical images in the manner described in Maccarone et al. (2003). The rms of the optical and X-ray source matches was $0.2''$.

The variable X-ray source CXOKMZJ033831.7-353058 is coincident with the globular cluster identified as 86:53.0 by Dirsch et al. (2004). The matching radius is only $0.14''$ confirming that this object is located in a GC. It is located almost exactly $4'$ due South of NGC 1399 at RA=03:38:31.7 Dec=-35:30:59.21 (J2000). These coordinates are based on the location of the source in the HST image aligned to the USNO system. The host globular cluster has a magnitude and colour R=22.02±0.03 and C-R=2.04±0.09, where the R band refers to the usual Kron-Cousins photometric system and the C band refers to the Washington photometric system and has $\lambda_{eff} = 3910\,\mathring{A}$ (Canterna, 1976; Dirsch et al., 2004). In the next few sections we examine all the *Chandra* and *XMM*-Newton observations of NGC 1399 which covered the position of the source (Table 5.2).

5.2.3 Short term variability and spectral analysis

We created background-subtracted light curves from the observations in which the source can be detected. As the source is fairly isolated with no obvious X-ray emitters nearby we used an annular region surrounding the object with ∼1:1 area ratio to determine the background-subtracted count rate. Only the first data set, *Chandra* observation 319, revealed a rapid short-term variability (see Fig. 5.1). The count rate declined by an order of magnitude during the first 10 ks. The source remained faint for the rest of the observation and showed no further evidence of measurable variability. To verify that the decline was not due to an instrumental effect we compared the light curves of other X-ray sources in the same CCD (ACIS-S3), and found no similar patterns.

The source light curve was fit with a straight line. This yielded a χ^2 of 127.7 for 23 degrees of freedom. The straight line fit can thus be rejected with greater than 99.9% confidence.

In the rest of this work, we consider the first 9,873 s of *Chandra* Obs ID 319 in which the count rate of the source is either high or declining to be the "bright" phase. The other 46,070 s during which the count rate is at a steady low level is referred to as the "faint" phase.

Spectroscopic analysis of the *Chandra* data was carried out using the Interactive Spectral Interpretation System (ISIS), version 1.4.9-55. Data were binned within ISIS into groups with signal-to-noise of at least 2.0, and all channels with at least this signal-to-noise within the range from 0.3-8.0 keV were included in the fits. Due to the limited count rate we only attempted to fit two standard models which are commonly used to describe the continuum spectra of X-ray binaries, disk blackbody (`DISKBB`) and power-law (`PO`). The foreground absorption was fixed to the Galactic neutral Hydrogen column density (nH) in the direction of NGC 1399, $\sim 1.31\times10^{20}$ cm^{-2} (Dickey & Lockman, 1990).

The data were fit using the Gehrels statistic to define the errors (with the errors set to $1+\sqrt{(N+0.75)}$, where N is the number of counts in the bin) on the individual bins, as this statistic has been shown to provide more reliable fitting to bins with low count numbers. It was found that binning to the more standard signal-to-noise of 5.0 per bin led to too few channels for fitting and binned out real information in the data. The uncertainty estimates for all fits reflect 90% confidence limits.

The results of the spectral fitting of the bright and faint epochs of the *Chandra* 319 observations are summarized in Table 5.1 and plotted in Fig. 5.2. Both the disk blackbody and power law fits reveal a soft spectrum for both time periods, with the PO model providing a marginally better fit. This is consistent with a lum s X-ray binary in a very-high state, where the power law component dominates the luminosity

Disk Blackbody					
Date	Obs. ID/Epoch	kT_{in} (keV)	Norm.	χ^2_ν	Unabsorbed Flux erg cm^{-2} s^{-1}
2000-1-18	Chandra 319 (bright)	$0.29\pm^{0.2}_{0.09}$	$0.17\pm^{2}_{0.2}$	0.44	1.9×10^{-14}
2000-1-18	Chandra 319 (faint)	$0.21\pm^{0.3}_{0.1}$	$0.077\pm^{7}_{0.08}$	0.62	2.1×10^{-15}
2001-1-07	XMM 0055140101	$0.42\pm^{0.3}_{0.2}$	$0.061\pm^{0.6}_{0.06}$	0.26	3.3×10^{-14}
2003-2-13	Chandra 2942	$0.90\pm^{3}_{0.5}$	$7.74\pm^{19000}_{8}\times10^{-4}$	0.66	1.0×10^{-14}
Power Law					
Date	Obs. ID/Epoch	Γ	Norm. $\times10^{-6}$	χ^2_ν	Unabsorbed Flux erg cm^{-2} s^{-1}
2000-1-18	Chandra 319 (bright)	$2.42\pm^{0.7}_{0.6}$	$5.81\pm^{2}_{2}$	0.43	2.8×10^{-14}
2000-1-18	Chandra 319 (faint)	$2.93\pm^{2}_{1}$	$0.55\pm^{0.4}_{0.4}$	0.31	2.8×10^{-15}
2001-1-07	XMM 0055140101	$2.47\pm^{0.9}_{0.6}$	$8.91\pm^{4}_{4}$	0.29	4.2×10^{-14}
2003-2-13	Chandra 2942	$1.33\pm^{1}_{1}$	$2.21\pm^{0.9}_{1}$	0.60	1.9×10^{-14}

TABLE 5.1: Spectral fitting results and flux estimates for the globular cluster X-ray source in NGC 1399

(Nowak, 1995; McClintock & Remillard, 2006). We note here that some of the inordinately large uncertainty estimates in the normalization of the disk blackbody models, for these and other fits listed in Table 5.1, are correlated to the large errors in the temperature, but lead to consistent total luminosity.

There is no statistically significant difference between the spectral properties of the source in the two epochs, other than their difference in brightness. Using the power-law model the X-ray flux of the source in the energy range of 0.3-8.0 keV is estimated to be 2.8×10^{-14} ergs cm^{-2} s^{-1} in the bright phase and 2.8×10^{-15} in the faint phase. Adopting a distance of 20 Mpc (Tonry et al., 2001) this implies an isotropic luminosity of 1.3×10^{39} ergs s^{-1} during the bright epoch and 1.3×10^{38} ergs s^{-1} during the faint one. We note here that the average luminosity quoted in Kundu et al. (2007), and mentioned in §2.1 above was calculated using fixed a spectral index Γ=1.7 for all sources in NGC 1399 due to the difficulty of reliably measuring this parameter for many of the sources superimposed on the bright hot gas in the inner regions.

5.2.4 Long term variability

We searched for the source in all of the *Chandra* and *XMM* data sets listed in Table 5.2. The source was detected in all observations through the middle of 2003 but appears to have subsequently turned off indicating long term variability. The individual observations are briefly discussed below. The luminosity values (0.3–8 keV) are for all *Chandra*, *XMM* and *ROSAT* data shown in Fig. 5.3.

5.2.4.1 *XMM* Observation 0055140101

These *XMM* observations were taken one year after the *Chandra* 319 observations discussed above. The source is located on the edge of the *XMM*-Newton EPIC MOS2 image and is the basis for its detection and listing as 2*XMM* J033831.7-353058:042943

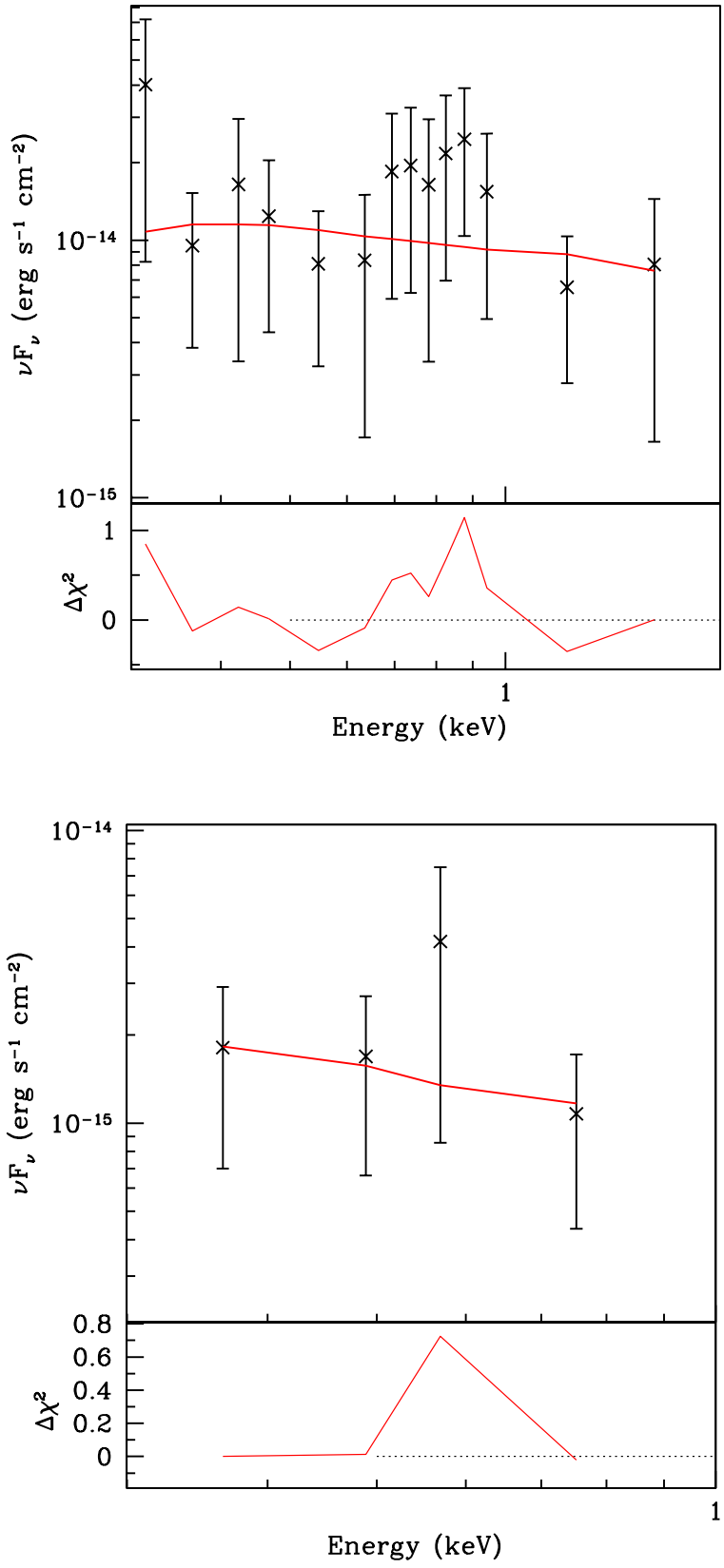

FIGURE 5.2: The energy density distribution of CXOKMZJ033831.7-353058 during the bright (top) and faint (bottom) phase of the *Chandra* Obs ID 319 observations. The best fit power law models and residuals are also shown. There is no obvious difference between the faint and bright epochs of the spectrum.

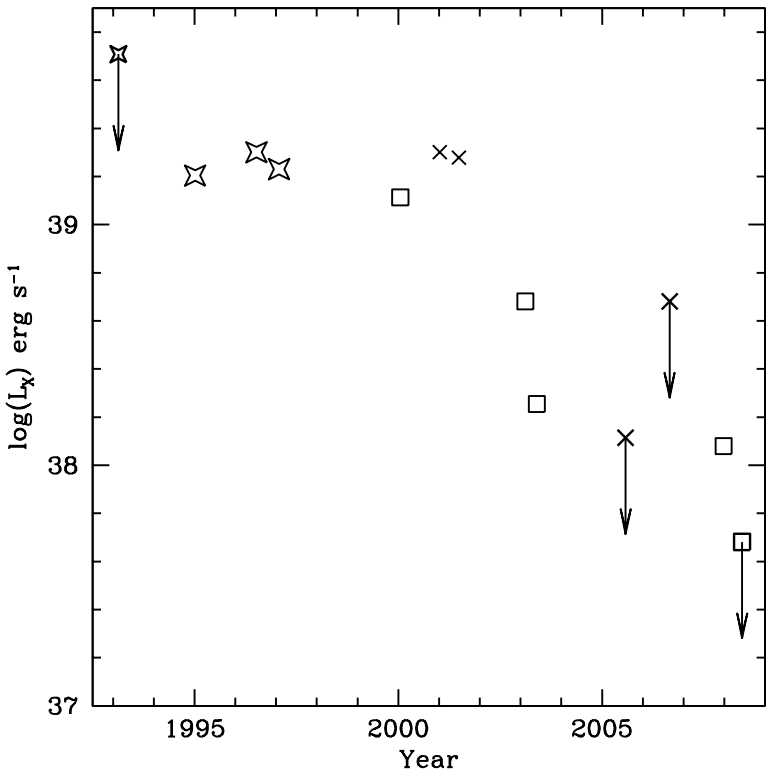

FIGURE 5.3: The long term light curve of CXOKMZJ033831.7-353058 showing the 0.3–8 keV luminosities. The squares, crosses and stars represent *Chandra*, *XMM* and *ROSAT* data respectively. The data point for *Chandra* 319 is from the bright phase spectrum.

Date	Observatory	Obs ID	Instrument	Exposure Time	Detection
2000-01-18	Chandra	319	ACIS-S3	55.9 ks[1]	yes
2001-01-07	XMM	0055140101[2]	EPIC-MOS2	47 ks	yes
2001-06-27	XMM	0012830101	EPIC-MOS2 & PN	10 ks	yes
2003-02-13	Chandra	2942	ACIS-S3	29.4 ks	yes
2003-05-26	Chandra	4172	ACIS-I3	44.5 ks	yes
2003-05-28	Chandra	4174	ACIS-I0	45.7 ks	yes
2005-07-30	XMM	0304940101	EPIC-MOS2, PN	20 ks	no
2006-08-23	XMM	0400620101	EPIC *all*[3]	73 ks	no
2007-12-24	Chandra	9798	ACIS-S3	18.3 ks	no
2007-12-27	Chandra	9799	ACIS-S3	21.3 ks	no
2008-06-08	Chandra	9530	ACIS-S3	59.3 ks	yes[4]

TABLE 5.2: *Chandra* and *XMM-Newton* Observations of the globular cluster X-ray source in NGC 1399

[1]bright:9.8 ks; faint:46.1 ks

[2]2XMM catalogue (Watson et al., 2009)

[3]MOS1, MOS2 & PN cameras.

[4]The luminosity of this marginal detection is lower than the upper limits implied in the previous non-detections, and is in the range of typical neutron star accretors. See text for details.

in the second *XMM*-Newton Serendipitous Source Catalogue (2*XMM*; Watson et al., 2009). We followed standard data reduction guidelines using `SAS v8.0`. As in the *Chandra* analysis we used an annular region surrounding the object with ∼1:1 area ratio to account for the background.

We fit the *XMM* data of the source in XSPEC 11.0 using the Gehrels statistic, without binning channels. Within the uncertainties the spectral properties of the source are indistinguishable from the *Chandra* 319 observations (Table 5.1). The flux, $F_X \simeq 4.2\times10^{-14}$ ergs cm^{-2} s^{-1} for the power law fit, is similar to the level of the bright phase of the *Chandra* 319 observations. Thus the source regained its luminosity within a year of the short term variability observed in the earlier *Chandra* data. This translates to an isotropic luminosity of $L_X \simeq 2\times10^{39}$ ergs s^{-1}, which is slightly brighter than the estimate from the bright phase of *Chandra* Obs ID 319, but consistent with previous *ROSAT* estimates (Liu & Bregman, 2005). However, we note that the short timescale variation in *Chandra* Obs ID 319 occurred at the very beginning of the observation leaving open the possibility that the source was in fact brighter immediately prior to this observation. Thus we consider the $L_X \simeq 2\times10^{39}$ ergs s^{-1} luminosity from this *XMM* observation to be a fairer estimate of the peak brightness of this source.

5.2.4.2 *XMM* Observation 0012830101

The source was detected in the 10 ks *XMM* Newton observations of NGC 1399 on 2001-06-27 (Obs ID 0012830101). Given the short exposure and consequently low counts we do not attempt to fit the spectrum. The 2*XMM* flux of this source is estimated to be 4.1×10^{-14} ergs cm^{-2} s^{-1}, which implies an isotropic luminosity of $L_X \simeq 1.9\times10^{39}$ ergs s^{-1}. Thus the source appears to have remained as bright as observed in the previous *XMM* observation obtained 6 months before.

5.2.4.3 *Chandra* Observation 2942

The source was in the field of view of the *Chandra* ACIS observation of NGC 1404, taken roughly three years after the *Chandra* 319 observation. At this time, the spectrum was harder than at earlier epochs (Table 5.1). The X-ray flux in the 0.3-8.0 keV band from the power law fit is 1.9×10^{-14} erg cm^{-2} s^{-1}, a factor of ∼2 lower than the previous epoch. However, the harder spectrum and the kT≃0.9 keV estimate suggests that the source may have undergone a state transition to a high/soft state as observed in stellar mass black holes (Nowak, 1995; McClintock & Remillard, 2006) and may be better described by a disk blackbody model. The flux estimate of $F_X \simeq 1\times10^{-14}$ erg cm^{-2} s^{-1} from a disk blackbody fit implies a luminosity of 4.8×10^{38} ergs s^{-1}, and a factor of 4 decline in the brightness from the previous *XMM* epoch.

5.2.4.4 *Chandra* Observations 4172 & 4174

Both of these observations were part of the Fornax Cluster survey. The source was in the field of view of the *Chandra* ACIS I3 (4172) or I0 (4174) chips. Although it was detected by CIAO's source detection tool, the count rate in each case was too low (3.06×10^{-4} and 1.39×10^{-4} cts/s) to derive meaningful result by fitting the spectrum. Instead we determined the X-ray flux using the simulation tool `PIMMS` by assuming that the spectral properties were unchanged since the *Chandra* observation 2942. The X-ray flux in the 0.3-8.0 keV range is $\simeq3.7\times10^{-15}$ erg cm^{-2} s^{-1}. Thus the luminosity of the source has dropped by another factor of 2 to 1.8×10^{38} ergs s^{-1} luminosity since the *Chandra* 2942 observation.

5.2.4.5 *XMM* Observations 0304940101 & 0400620101

The source is not detected in the *XMM*-Newton observations 0304940101 and 0400620101. Neither automated routines nor a careful visual inspection revealed any evidence of an object at or near the location of the source. The measured count rate at the position of the source is indistinguishable from that of the nearby background. Using the *XMM* FLIX tool we estimate an upper limit of 2.7×10^{-15} ergs cm^{-2} s^{-1} on July 30, 2005 and 1×10^{-14} ergs cm^{-2} s^{-1} on Aug 23, 2006. Thus the source was fainter than $L_X \leq 4.8\times10^{38}$ ergs s^{-1} at this time.

5.2.4.6 *Chandra* Observations 9798 & 9799

We also investigate the two *Chandra* observations 9798 and 9799 aimed at SN2007on. Since they were taken only three days apart, it makes sense to combine the results from the analyses of the two data sets to get one flux value/upper limit. The black hole candidate is 4.9′ off axis in these observations, but is undetected in both. We attempt to estimate an upper limit on the flux by determining how many photons are within 2″ of its location. In observation 9798 we find 4 photons from 0.5 to 8.0 keV within that radius, with an expectation value of $0.96 \pm .03$ photons estimated by looking at an off-axis background region. In observation 9799 we find 7 photons, with an expectation value of 1.24 ± 0.03. The source is thus marginally detected when the two observations together are considered – there is only a 2×10^{-5} probability that 11 photons will be detected given a background expectation value of 2.2 photons.

One can then calculate the luminosity of the source during these two observations, given that the source is marginally detected, with 11 photons seen in 40 ks. This translates to a count rate of 2.8×10^{-4} photons s^{-1}. Assuming the spectrum was unchanged since the *Chandra* 2942 observations this corresponds to a flux limit of 2.6×10^{-15} erg cm^{-2} s^{-1} and a 0.3–8 keV luminosity of 1.2×10^{38} erg s^{-1}.

5.2.4.7 *Chandra* Observation 9530

The source was in the field of view of the *Chandra* 9530 observation of NGC 1399 obtained on 2008-06-08. No object is detected at the location of the source with the probability of false detection set to 10^{-6}. However there is a marginal detection when the false source probability is relaxed to 10^{-4}. This yields 13 background subtracted counts during the course of this 60 ks observation. Although the number of counts is insufficient to fit a spectrum, we can estimate the luminosity by comparing the count rate to previous *Chandra* observations. If the source had a soft spectrum similar to that observed on 2001-1-18 then scaling the count rate to the *Chandra* 319 observations yields a luminosity of $L_X \leq 4.1 \times 10^{37}$ ergs s^{-1}. If on the other hand it retained the harder spectral shape of the 2003-2-13 *Chandra* 2942 detection, scaling the count rate to that observation estimates a luminosity of $L_X \leq 4.8 \times 10^{37}$ ergs s^{-1}. Thus, irrespective of the details of the spectrum the source was $L_X \leq 4.8 \times 10^{37}$ ergs s^{-1} or fainter at this epoch. This is fainter than the upper limit of the luminosities derived from the previous observations in which the source was not detected, and confirms that it faded since the 2003 *Chandra* detection. We also note that a luminosity of $L_X \leq 4.8 \times 10^{37}$ ergs s^{-1} is typical of bright neutron star accretors. There is a high probability of such an object being associated with a high mass, metal-rich globular cluster such as the one being studied here (Kundu et al., 2007). Thus the black hole accretor itself may in face be fainter than the luminosity estimated from the *Chandra* 9530 observation.

5.3 Discussion and Analysis

We have confirmed that the X-ray source previously identified as CXOKMZJ033831.7-353058 (Kundu et al., 2007) and 2*XMM* J033831.7-353058:042943 (Watson et al., 2009) is associated with the spectroscopically confirmed globular cluster 86:53.0 (Dirsch et al., 2004) in NGC 1399. We have examined the X-ray activity of the source over a period of 8 years using archival *Chandra* and *XMM*-Newton data.

Between Jan 2000 and Feb 2003 the X-ray luminosity of the source was above 10^{39} ergs s^{-1}, based on an estimated distance of 20 Mpc to NGC 1399 (Tonry et al., 2001). Earlier *ROSAT* observations sampling various epochs between 1993 and 1997 estimated a similar luminosity of $2{\times}10^{39}$ ergs s^{-1} (Liu & Bregman, 2005). This is well beyond the Eddington luminosity of spherical accretion on to a neutron star and places the source into the category of an ultra luminous X-ray source.

During the course of the first *Chandra* observation in this analysis (Obs ID 319 in Jan 2000) the source revealed a rapid short-term decline in the count rate within 10 ks, demonstrating that the source is not a superposition of multiple neutron star

binaries and confirming that it is a black hole. After RZ 2109 in NGC 4472 (Maccarone et al., 2007) this is only the second BH X-ray accretor positively identified through short term variations in the count rate. Curiously both sources revealed roughly order of magnitude declines over similar time periods of $\simeq$10 ks.

But the parallels appear to end there. The decline in the count rate in RZ 2109 was primarily in the soft X-ray band, indicating a change in the X-ray spectrum consistent with foreground absorption and not a variation in the inherent X-ray luminosity of the source (Shih et al., 2008). On the other hand there is no statistical difference in the spectrum of CXOKMZJ033831.7-353058 between the bright and faint phases in the *Chandra* 319 observations (Table 5.1 and Fig. 5.2). This suggests that either the luminosity of the source changed during the course of the *Chandra* 319 observation or that a portion of the X-ray emitting region was obscured by an eclipsing event.

The NGC 1399 BH also reveals long term variability. Other than a portion of the *Chandra* Obs ID 319 integration the source remained brighter than 10^{39} ergs s^{-1} from the 1993 *ROSAT* observations through the 2001 *XMM*-Newton observations. Thereafter it became progressively fainter. It was not detected in *XMM* and *Chandra* observations between 2005 and 2007. An $L_X \leq 4.8 \times 10^{37}$ ergs s^{-1} source was marginally detected in a deeper 2008-06-08 *Chandra* observation. However such a luminosity is typical of bright neutron star accretors and there is a high probability of such an object being associated with the host globular cluster of this source. The black hole accretor itself may in fact be even fainter than $L_X = 4.8 \times 10^{37}$ ergs s^{-1} at this point.

The *Chandra* 2942 observation from 2003 which showed the first clear evidence of a long term decline in the luminosity has a spectral index of Γ=1.3, considerably harder than the Γ=2.4-2.9 spectrum at earlier epochs. This suggests that the source underwent a state transition from a very-high state where the power law component dominates to a high/soft state where the emission is primarily thermal (Nowak, 1995; McClintock & Remillard, 2006). Such state changes accompanying luminosity variations in a GC BH points to some interesting issues about identifying and quantifying BHs in globular clusters.

BH candidates in nearby galaxies (and their GC systems) are identified on the basis of their higher luminosities and softer spectra as compared to NS accretors. However, the hardening of the spectrum of CXOKMZJ033831.7-353058 as it faded places both its luminosity and its spectrum in the range of typical neutron star LMXBs ($L_X \leq 10^{38}$ergs s^{-1}, $\Gamma \simeq 1.7$) in the latter epochs of our survey. Thus an unrecognised fraction of the LMXBs in GCs tagged as neutron star systems in snapshot observations of extragalactic systems are likely BH accretors.

The long term variability of CXOKMZJ033831.7-353058 itself provides strong evidence that the source is a black hole. The source was consistently in the ultraluminous regime for at least a decade prior to 2003, before fading relatively rapidly within a span of less than two years. If this object were a superposition of multiple close to Eddington limited neutron star LMXBs it is highly unlikely that they would all conspire to change luminosity within such a short time period. Moreover, given the fact that this is similar to the light travel time across the core of a typical cluster (where neutron star LMXBs are expected to reside) the degree of coincidence required is even more unlikely. The fact that a confirmed X-ray bright black hole system in a GC undergoes physical changes similar to those seen in stellar mass BHs in the MW on the timescales of years is encouraging in terms of identifying and studying the demographics of BHs in GCs. It indicates that BHs can be securely identified by monitoring on month-to-year scales without requiring fortuitous occurrences of short term variations within a single observation.

There have been previous attempts to detect BHs in elliptical galaxies by such monitoring (e.g. Irwin, 2006; Brassington et al., 2008). However, the only likely BHs identified using this technique (Fabbiano et al., 2006; Sivakoff et al., 2008) have been field sources that are not associated with GCs. It is particularly interesting that Irwin (2006), who studied NGC 1399 using a subset of this data set, did not recognize the transient nature of CXOKMZJ033831.7-353058. The luminosity of the source varied by about an order of magnitude between the (bright phase of the) *Chandra* 319 observations and *Chandra* 4172 observations that bookend the Irwin (2006) analysis. This can likely be attributed averaging across the short term variation in the first epoch which leads to an underestimate of the consistently higher luminosities observed over a decade. We note that the luminosity quoted in our own Kundu et al. (2007) study similarly underestimated the brightness of CXOKMZJ033831.7-353058 in the *Chandra* 319 integration for the same reason. Given that at least four accreting BH systems in elliptical galaxies (Fabbiano et al., 2006; Maccarone et al., 2007; Brassington et al., 2010, and this source) are known to show short term X-ray flux variability (accompanied by spectral changes in some cases) this strongly argues that careful analysis of both short and long term variations of potential BH candidates must be carried out in concert if more BHs are to be identified by this method.

5.3.1 Black hole hosting globular clusters

There are now several GCs known to host BHs or that are strong candidates: RZ 2109 (Maccarone et al., 2007), the subject of this work 86:53.0, another system in NGC 4472 (Maccarone et al., 2011), a second NGC 1399 GC (Irwin et al., 2009), a GC in NGC 3379 (Brassington et al., 2008, 2010) and a Milky Way GC, M 22, which hosts two BHs (we note that the BHs in M 22 were identified using radio interferometry rather than X-ray observations; Strader et al., 2012). The properties of these globular

clusters, such as optical photometry data, are briefly discussed. Where possible, mass estimates are also included. These data are summarised in Table 5.3 (see also Table 2 in Maccarone et al., 2011). Colour-magnitude diagrams for these GCs are shown in Fig. 5.4.

RZ 2109 is a blue, metal-poor cluster in NGC 4472, with B–R=1.06±0.03 (Rhode & Zepf, 2001) and [Fe/H]=-1.7 dex (Maccarone et al., 2007). RZ 2109 is also one of the most luminous, and hence most massive GCs in NGC 4472, having V=20.99±0.01 (Rhode & Zepf, 2001) and M=2×10^6 $M_\odot$ (Zepf et al., 2008). In quantitative terms RZ 2109 is about 2.6 magnitudes brighter than the peak of the globular cluster luminosity function.

86:53.0 in NGC 1399 has a colour of C-R=2.04±0.09 (C=24.06±0.08, R=22.02±0.03) (Dirsch et al., 2004). This places it at the reddest, and hence the most metal-rich end of the metal-rich subpopulation of GCs (Dirsch et al., 2004). Based on the calibration of Lee et al. (2008) this translates to a supersolar metallicity of [Fe/H]$\simeq$ +0.2 dex. While 86:53.0 is also among the largest GCs in NGC 1399, unlike RZ 2109, it is not at the tail end of the luminosity function. 86:53.0 in NGC 1399 is only 1.3 magnitudes brighter than the peak. In other words 86:53.0 is about one-third the mass of RZ 2109.

The second BH hosting GC in NGC 4472 (henceforth called RZ 2064) is one of the reddest clusters in the NGC 4472 system, having B–R=1.44±0.05 (Rhode & Zepf, 2001) which translates to a metallicity of [Fe/H]=+0.5 dex (Maccarone et al., 2011, and references therein). RZ 2064 has a V band magnitude of V=21.55±0.02 (Rhode & Zepf, 2001), which, at the distance of NGC 4472 (d=16 Mpc Macri et al., 1999) and using the mass-to-light ratio $(M/L)_V$=2 adopted in Zepf et al. (2008) (see also Anders et al., 2003; Bruzual & Charlot, 2003), gives the GC mass of 9.9×10^5 $M_\odot$. RZ 2064 is therefore quite different from RZ 2109 as it is less luminous and massive than RZ 2109, but has a much higher metallicity.

Conversely, the second GC to host a BH in NGC 1399 (henceforth called KMZ 320) is quite similar to 86:53.0. It has a B–I colour of 2.25±0.02 (B=23.23±0.01, I=20.97±0.01), making it one of the reddest GCs in the NGC 1399 GC system (Kundu et al., 2007). KMZ 320 has a supersolar metallicity of [Fe/H]$\simeq$ +0.5 dex (Maccarone et al., 2011, and references therein). Grillmair et al. (1999) surveyed the GC system of NGC 1399 (also using the *Hubble Space Telescope*) and converted B band magnitudes to V band using $(B-V) = 0.347(B-I) + 0.163$. Using this conversion formula, we find that KMZ 320 has V=22.28±0.01. Using a distance to NGC 1399 of 20 Mpc, and mass-to-light ratio of two, we calculate KMZ 320 has a mass of 7.6×10^5 $M_\odot$, similar to that of 86:53:0.

In NGC 3379, the BH hosting cluster (henceforth called KMZ 57) was found to have V=21.82±0.01 and a V–I colour of 1.13±0.01 (Kundu et al., 2007). The mean

Source	M_V	Colour	metallicity [Fe/H]	mass (10^5 $M_\odot$)
RZ 2109	V=20.99	B–R=1.06	–1.7	20
86:53:0	R=22.02	C-R=2.04	+0.2	6.67
RZ 2064	V=21.55	B–R=1.44	+0.5	9.9
KMZ 320	V=22.28	B–I=2.25	+0.5	7.6
KMZ 57	V=21.82	V–I=1.13	–0.5	3.4
M 22	V=5.1	B–V=0.68	–1.7	3.8

TABLE 5.3: Properties of the black hole hosting globular clusters.

V–I colours for NGC 3379 are 1.10–1.12; thus this system is only slightly redder than average for a GC in NGC 3379 . This cluster is one of the brighter clusters in the system. KMZ 57 has a metallicity of –0.5 dex (Maccarone et al., 2011, and references therein). Using a distance to NGC 3379 of 10.6 Mpc (Tonry et al., 2001), we estimate the mass of the cluster to be 3.4×10^5 $M_\odot$.

M 22 hosts not one, but two BHs. It is a blue, metal poor GC with B–V=0.68 and [Fe/H]=–1.7 dex (Harris, 1996). M 22 has an absolute V band magnitude of -8.5 and a V band mass-to-light ratio of 1.87. Thus we estimate its mass to be 3.8×10^5 $M_\odot$.

Thus there are two blue and four red GCs that are known to host BHs. Given the very small size of the sample of BH hosting GCs, one cannot draw any firm conclusions about what GC properties influence whether a cluster will host a BH. However, it is interesting to note that even with only six GCs, the metal-rich clusters out number the metal-poor system by two to one. We know from other studies of GCs have shown that red GCs are more than three times as likely to host an LMXB as blue GCs (e.g. Jordán et al., 2004; Kim et al., 2006b; Sivakoff et al., 2007; Kim et al., 2009). As the number of BH hosting GCs increases, it would be interesting to see whether the red to blue BH GC ratio is the same as that of the LMXB hosting GCs.

Another feature of accreting BHs in globular clusters may be the presence of optical emission lines. The optical spectrum of RZ 2109 reveals broad, $\simeq$2000 km s^{-1} wide, bright [O III] emission associated with the BH (Zepf et al., 2008). Irwin et al. (2009) argue that another ultraluminous X-ray source in a globular cluster in the inner region of NGC 1399 is a black hole on the basis of $\simeq$75 km s^{-1} [O III] and [N II] lines. An optical spectrum of 86:53:0 taken with the SOAR optical telescope in 2009 shows no evidence of emission lines. A previous 2-hour Magellan/IMACS optical spectrum of this globular cluster taken in November 2006 (Jimmy Irwin, private communication) also reveals no emission lines. However we note, on the basis of our X-ray monitoring, that the X-ray source had faded considerably before either set of optical spectra were obtained.

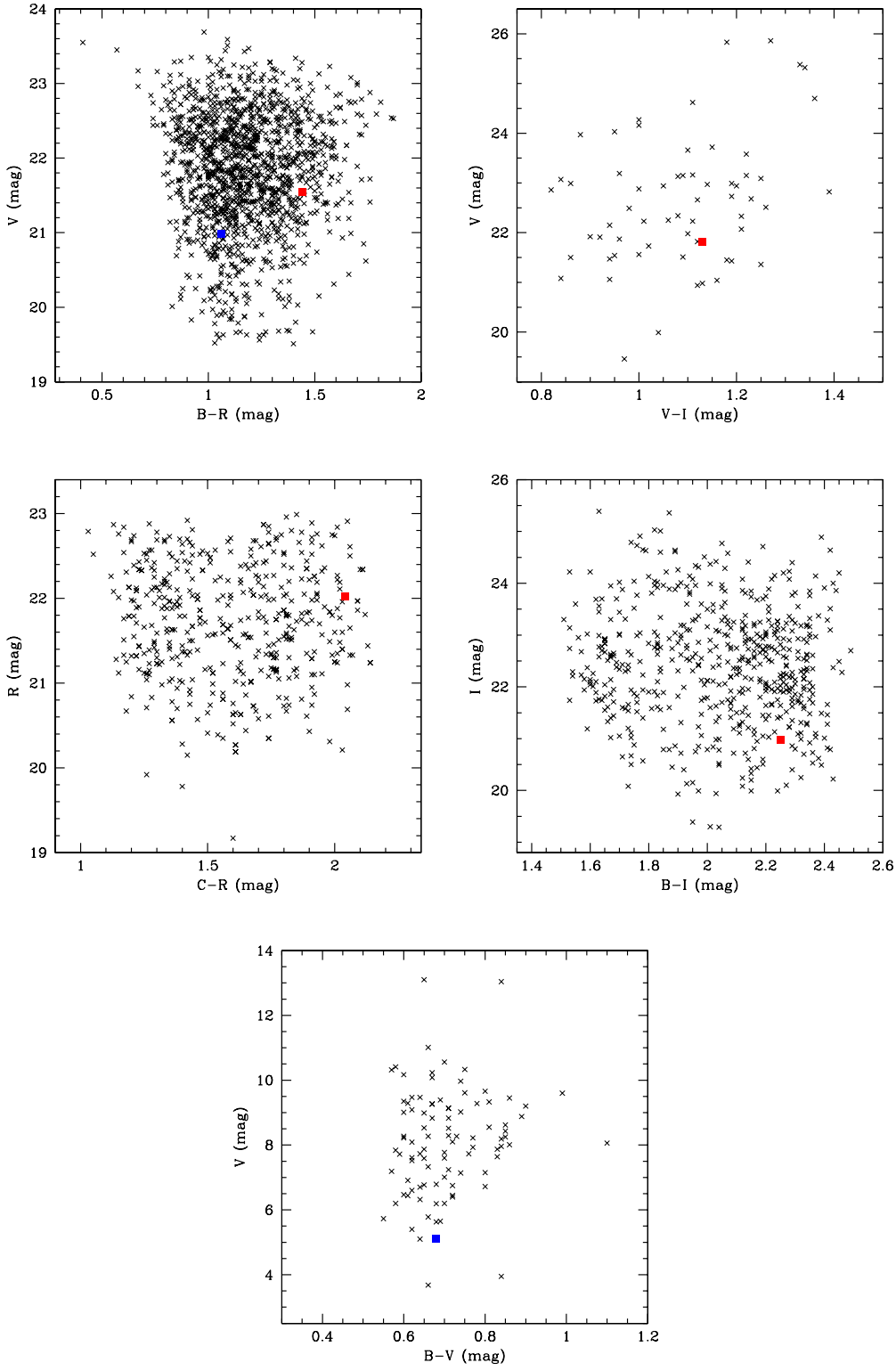

FIGURE 5.4: The colour-magnitude diagrams for black hole hosting globular clusters in their respective host galaxies. The filled squares indicate the data point for the BH hosting GCs. The data for these diagrams is taken from the same sources as the photometric parameters listed in the text. For the plot of NGC 4472 shown in the top left panel, the red square corresponds to RZ 2064 and the blue square corresponds to RZ 2109. The data for NGC 3379 is in the top right panel. The NGC 1399 data for 86:53:0 and KMZ 320 are in the middle left and right panels respectively. The data for M 22 (bottom panel) is for resolved globular clusters in the Milky Way only (Harris, 1996).

5.4 Conclusions

We have discovered an accreting black hole (BH) in a spectroscopically confirmed globular cluster (GC) in NGC 1399 through monitoring of its X-ray activity. The source, CXOKMZJ033831.7-353058, with a peak luminosity of $L_X \simeq 2\times10^{39}$ergs s^{-1}, reveals an order of magnitude change in the count rate within $\simeq$10 ks in a *Chandra* observation. The BH resides in a metal-rich [Fe/H]$\simeq$0.2 globular cluster. After RZ 2109 in NGC 4472 this was only the second black-hole X-ray source in a GC confirmed via rapid X-ray variability. Unlike RZ 2109, the X-ray spectrum of this BH source did not change during the period of rapid variability.

In addition to the short-term variability the source also exhibits long-term variability. After being bright for at least a decade since 1993 within a span of 2 years it became progressively fainter, and eventually undetectable, or marginally detectable, in deep *Chandra* and *XMM* observations. The source also became harder as it faded. The characteristics of the long term variability in itself provide sufficient evidence to identify the source as a BH.

Our discovery of the second confirmed BH accretor in a globular cluster on the basis of X-ray variability, and the subsequent discovery of other such systems, indicates that the discovery of RZ 2109 in NGC 4472 was not due to a particularly fortuitous configuration in that system and provides encouraging evidence that more such BHs can be identified by monitoring the X-ray activity. Further studies of, for example, temporal variability of luminous X-ray sources in nearby galaxies are needed to establish reliable statistics on the ubiquity of black holes in globular clusters.

Chapter 6

Concluding Remarks and Future Work

6.1 Concluding Remarks

In this thesis I have explored various aspects of X-ray binaries. I have investigated both individual sources as well as studying global properties of an ensemble of systems. I have helped to discover new and interesting objects and delved more deeply into the nature of already known sources.

6.1.1 The M 82 transient source

Given its location in the central region of a starburst galaxy and its relatively high radio emission, the transient M 82 source is most likely a high mass X-ray binary. The lack of detected X-ray emission (99% confidence level upper limit, $L_X \sim 2 \times 10^{37}\,\mathrm{erg\,s^{-1}}$) suggests that this system is unlikely to be a normal HMXB and hints at a more peculiar nature.

6.1.2 Black hole X-ray binaries in globular clusters

We discovered an accreting black hole binary in a globular cluster of NGC 1399 by analysing its X-ray variability. This discovery demonstrates that such systems are not exceedingly rare and has helped to overturn the long-held belief that stellar mass black holes formed in GCs would be ejected via dynamical interactions (Sigurdsson & Hernquist, 1993; Kulkarni et al., 1993). Subsequently, other black hole binary systems in globular clusters have also been observed (see Irwin et al., 2009; Brassington et al., 2010; Maccarone et al., 2011; Strader et al., 2012).

The first black hole binary to be discovered in a globular cluster, XMMU 122939.7+075333, was studied in great detail. The source was not found to undergo any spectral state changes and appears to be persistently luminous over a period of 11 years. More interestingly, the source also shows possible evidence for soft (0.65 keV) X-ray line-like emission from highly ionised oxygen.

6.1.3 The X-ray binaries of NGC 4472

The X-ray binary population of NGC 4472 was studied using recent deep *Chandra* data. This survey revealed nearly 100 new X-ray sources in the galaxy, for total of 242 sources. The number of LMXBs found residing in GCs is 81, nearly three times as many as observed using the shallower observations of Kundu et al. (2002). This larger sample of X-ray binaries allows for a more robust analysis of its X-ray properties.

There appears to be no significant difference between the X-ray luminosity functions of the GC and field LMXB populations, in keeping with the results found by (Kundu et al., 2002). In addition, we found that red GCs were four times more likely to host an LMXB than blue GCs. This is slightly higher than the ratios found by other studies of GC LMXB populations Kundu et al. (2002); Kim et al. (2006b, 2009).

However, our analysis did provide tentative evidence that red LMXB host GCs are more centrally located than blue ones. Kim et al. (2006b) also found similar results for their study of GCs in elliptical galaxies. They suggested that GCs closer to the galactic centre have higher rates of the dynamical processes that lead to LMXB formation, which would explain why red GCs are more likely to host a LMXB than blues GCs.

6.2 Future Work

Future research topics are outlined below. Some of these projects will require the procurement of additional data, both in the X-rays and at other wavelengths. However, much of the proposed research can be carried out with data that is already available.

6.2.1 M 82 radio transient

We have suggested that the transient radio source in M 82 could be an exotic extragalactic microquasar similar to SS 433, an unusual Galactic microquasar (e.g. Margon, 1984). In addition to its interesting X-ray, radio and optical properties, SS 433 has several bright, highly Doppler shifted infrared emission lines (Paschen α and Brackett γ to B 15; Thompson et al., 1979).

We would like to establish whether the M 82 transient source has any such infrared emission lines as they could be used as a diagnostic tool to verify its nature. The presence of such lines will strengthen the case that the source is an extragalactic SS 433-like microquasar as well as provide information on the kinematics of the system.

To this end, Fraser et al. (2009) used archival *HST* near infrared (NIR) data taken in 1998 and compared it to *Gemini* North NIR data taken in June 2009. They found no difference between the NIR images taken before and after the transient switches on. They calculated a a $3\,\sigma$ upper limit for the absolute K band magnitude of $\mathrm{M_K} = -5$.

Subsequently, more NIR *HST* data (taken between November 2009 and January 2010) has become available. We will use these data to search for an IR counterpart to the M 82 and use the results to guide further investigations into the source.

6.2.2 NGC 4472 X-ray binary population

6.2.2.1 Luminous X-ray sources in NGC 4472

The study of the LMXB population of NGC 4472 has also revealed 16 sources with $\mathrm{L_{X,0.5-5\,keV}} \gtrsim 2.5{\times}10^{38}\,\mathrm{erg\,s^{-1}}$ in the combined 380 ks data set. These sources have a sufficient number of counts in the individual data sets to allow for deeper investigation into their spectral and temporal properties. One of these sources is the globular cluster black hole system, CXOU 1229410+075744 discovered by Maccarone et al. (2011). We hope that the study of these bright sources will reveal more such interesting sources as well as shedding light on the bright XRB population of the galaxy.

6.2.2.2 Transients in NGC 4472

The four data sets used in our analysis of NGC 4472 span 11 years. We thus have an opportunity to search for transient X-ray sources in the galaxy. Preliminary analysis has already revealed several transient candidates.

6.2.3 Soft X-ray line emission from XMMU 122939.7+075333

The spectral analysis of XMMU 122939.7+075333 revealed soft X-ray line-like emission. We hope to gain a better understanding of XMMU 122939.7+075333 by studying the soft X-ray spectrum in more detail. For example, the presence or absence of emission or absorption features in the soft X-ray regime could reveal more about the ionisation state of the emission region, constrain the ionisation mechanism and provide

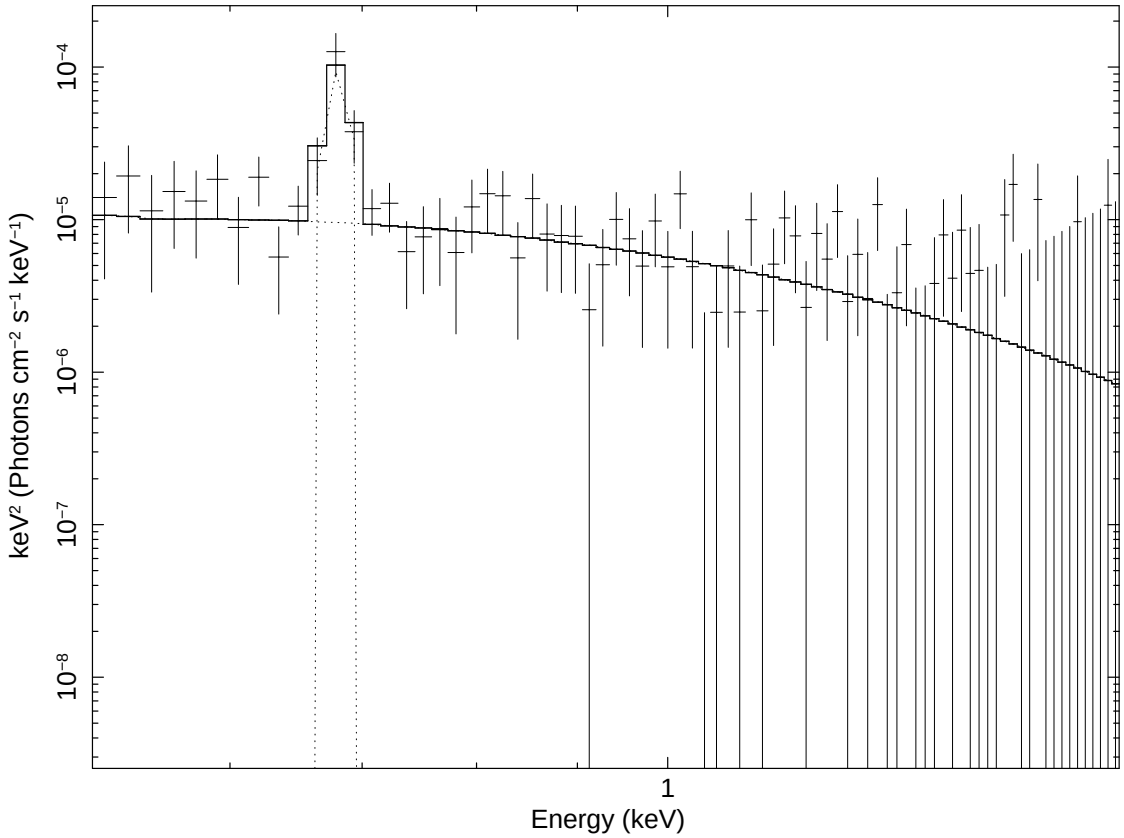

FIGURE 6.1: A simulated spectrum of XMMU 122939.7+075333 using the *Chandra* LETG response files. The exposure time is 500 ks and a disk blackbody plus Gaussian component model was used as input.

insight into the chemical abundances in the system. To this end, we require more detailed X-ray observations with both increased signal-to-noise and spectral resolution.

In order to distinguish whether the soft X-ray excess seen in XMMU 122939.7+075333 is due to an actual emission line, we need better spectral resolution in the soft X-ray regime than can be achieved by the imaging instruments on X-ray satellites. To this end, I have carried out a spectral simulation using the *Chandra* Low Energy Transmission Grating (LETG) response matrices. We set the exposure time to 500 ks and used the disk blackbody plus Gaussian line spectral model outputs for Obs ID 12888 as inputs for the simulation.

The resultant spectrum is shown in Fig. 6.1. This plot shows that a spectral line with the same parameters derived in § 4 will be detectable using the LETG. The fit was also carried out without the Gaussian component. χ^2/ν is 8.85/9 and 30.7/12 for disk blackbody plus Gaussian and disk blackbody model only respectively. The Gaussian line therefore appears to be at least marginally significant. Moreover, such an observation should also be able to detect the continuum below 0.6 keV, which will allow for better parametrisation of the soft excess.

6.2.4 Using X-ray binaries to study the Universe

In this section we discuss the how the outcomes of X-ray binary studies can be used to shed light on the unanswered questions about stellar evolution. We also discuss how the findings of XRBs studies can be used to probe the contents of the Universe.

The results of the study of the XRBs in NGC 4472 can be compared to the XRB populations of the Milky Way (e.g. The Galactic Bulge Survey; Jonker et al., 2011) and other galaxies (and their GC systems) (e.g. Kundu et al., 2002; Kim et al., 2006b; Brassington et al., 2008; Zhang et al., 2011). Doing so will allow us to determine how factors such as metallicity, environment, dark matter content and star formation rate of the host galaxy influence XRB properties like formation rate, spatial distribution and luminosity.

In addition to comparing the findings of observational studies of XRBs to each other, these results can also be compared to the output from binary population synthesis model predictions (see e.g. Zhang et al., 2004; Li et al., 2006; Bogomazov & Lipunov, 2008; Zhu et al., 2012, and references therein). These data starved frameworks for binary evolution are poorly constrained and require observational data to make them more robust and accurate. The following is a non-exhaustive list of parameters and areas of uncertainties in binary population synthesis models: the initial distribution of binary periods, the initial distribution of mass ratios, neutron star kicks, uncertainties in actual stellar evolution, the poorly understood common envelope phase in binaries which appears to be necessary to reproduce the observations. These parameters could be constrained with the results of our research into XRBs, such as X-ray luminosity functions, spatial distribution of sources, etc.

Maccarone et al. (2005) found five LMXBs in the Sculptor dwarf spheroidal galaxy. Using this finding, Dehnen & King (2006) showed that in order for a low mass galaxy such as Sculptor to contain a population of LMXBs, it must be surrounded by an extended dark matter halo more than two orders of magnitude more massive than the observed stellar mass of the galaxy. The presence of dark matter halos around dwarf spheroidal galaxies has important implications for cold dark matter cosmology models as it would help to solve the "missing satellite" problem (see e.g. Mashchenko et al., 2005). Thus the results of XRB research can be used to shed light on the location and distribution of dark matter in the Universe, which is one of the most fundamental issues in astrophysics today.

The BH in RZ 2109 (Maccarone et al., 2007) was used to constrain theoretical models of the very nature of our Universe. In theoretical physics, the large disparity between the characteristic properties of the weak and gravitational forces is called the hierarchy problem (see e.g. Arkani-Hamed et al., 1998). A solution to this problem is that Universe contains large scale extra dimensions. The size of these extra dimensions

can be constrained if the age of BHs in the Universe is well determined. The fact that a BH resides in a GC places strong constraints on its age. Gnedin et al. (2009) used this well constrained age of the BH in RZ 2109 to determine that the upper limit of the size of extra dimensions in our Universe is $\lesssim 3 \times 10^{-6}$ m, an order of magnitude lower than previous estimates. This upper limit can be further refined by using the data from the other BHs now known to reside in GCs, including the source discussed in § 5 (see also Irwin et al., 2009; Brassington et al., 2010; Maccarone et al., 2011; Strader et al., 2012).

The study of binary stellar systems has wide ranging applications. X-ray binaries, in particular, are powerful tools that can be used to reveal the nature of the Universe.

Appendix A

Source data for the X-ray point source population of NGC 4472

TABLE A.1: the table of X-ray fluxes of the sources within 3.7′ of the galaxy centre. The fluxes are in units of erg s^{-1} cm $^{-2}$. The PL and diskbb subscripts denote the spectral model conversion factor used to calculate the flux. The "err" designation denotes flux errors. The flag column identifies sources that are interesting and/ or for which caution must be used when analysing the source properties. The key is as follows: bkg = source in an area of high background, c = *wavdetect* has misidentified or not detected the source in one of the observations, cg = the source is in or very close to a chip gap in one of the observations and GC = the source is associated with a globular cluster.

RA	DEC	Flux$_{PL}$	Flux$_{PL}$ err	Flux$_{PL}$	Flux$_{PL}$ err	Flux$_{diskbb}$	Flux$_{diskbb}$ err	Flux$_{diskbb}$	Flux$_{diskbb}$ err	Flag
degrees	degrees	0.5–05 keV	0.5–5 keV	0.5–2 keV	0.5–2 keV	0.5–5 keV	0.5–5 keV	0.5–2 keV	0.5–2 keV	
187.49977	8.02063	1.456E-14	1.724E-15	7.641E-15	9.052E-16	1.536E-14	1.829E-15	6.248E-15	7.436E-16	
187.49804	8.02989	9.137E-16	2.96E-16	4.795E-16	1.553E-16	9.639E-16	3.125E-16	3.921E-16	1.271E-16	
187.49757	7.99843	1.097E-15	2.586E-16	5.759E-16	1.357E-16	1.158E-15	2.732E-16	4.709E-16	1.111E-16	
187.49175	7.96768	2.955E-15	7.334E-16	1.551E-15	3.849E-16	3.118E-15	7.746E-16	1.268E-15	3.151E-16	
187.4915	7.96826	1.831E-15	3.881E-16	9.61E-16	2.037E-16	1.932E-15	4.101E-16	7.858E-16	1.668E-16	
187.49098	7.99121	1.57E-15	3.028E-16	8.242E-16	1.589E-16	1.657E-15	3.201E-16	6.739E-16	1.302E-16	
187.49021	7.9924	1.708E-15	3.068E-16	8.962E-16	1.611E-16	1.801E-15	3.245E-16	7.328E-16	1.32E-16	GC
187.4864	7.95771	1.174E-14	1.4E-15	6.161E-15	7.35E-16	1.238E-14	1.485E-15	5.038E-15	6.037E-16	
187.48501	8.00251	2.698E-15	4.041E-16	1.416E-15	2.121E-16	2.847E-15	4.278E-16	1.158E-15	1.74E-16	
187.48483	8.00848	4.122E-15	5.459E-16	2.163E-15	2.866E-16	4.348E-15	5.784E-16	1.769E-15	2.352E-16	GC
187.48422	8.01345	1.04E-15	2.815E-16	5.456E-16	1.478E-16	1.097E-15	2.973E-16	4.462E-16	1.209E-16	
187.48301	7.95625	2.273E-15	4.133E-16	1.193E-15	2.169E-16	2.398E-15	4.37E-16	9.755E-16	1.777E-16	GC
187.48287	8.00096	1.573E-15	2.989E-16	8.256E-16	1.569E-16	1.66E-15	3.16E-16	6.751E-16	1.285E-16	GC
187.48118	8.04989	1.093E-15	2.851E-16	5.736E-16	1.496E-16	1.153E-15	3.011E-16	4.691E-16	1.225E-16	
187.47628	8.01613	2.624E-15	3.811E-16	1.377E-15	2.001E-16	2.768E-15	4.035E-16	1.126E-15	1.641E-16	
187.47602	8.00271	4.855E-15	6.329E-16	2.548E-15	3.323E-16	5.122E-15	6.707E-16	2.084E-15	2.727E-16	GC
187.47566	7.95535	5.978E-15	7.763E-16	3.137E-15	4.076E-16	6.306E-15	8.227E-16	2.565E-15	3.345E-16	
187.47488	8.04315	1.475E-15	2.801E-16	7.742E-16	1.47E-16	1.556E-15	2.961E-16	6.331E-16	1.204E-16	
187.47378	7.99391	6.018E-15	7.739E-16	3.158E-15	4.063E-16	6.348E-15	8.203E-16	2.582E-15	3.335E-16	
187.47378	8.04469	3.28E-15	4.665E-16	1.721E-15	2.449E-16	3.46E-15	4.94E-16	1.408E-15	2.009E-16	
187.47234	8.00724	3.509E-15	4.779E-16	1.842E-15	2.509E-16	3.702E-15	5.062E-16	1.506E-15	2.058E-16	GC
187.47229	8.0526	3.172E-15	4.433E-16	1.665E-15	2.327E-16	3.346E-15	4.695E-16	1.361E-15	1.909E-16	GC
187.47228	8.01491	2.586E-15	3.796E-16	1.357E-15	1.993E-16	2.728E-15	4.019E-16	1.11E-15	1.634E-16	
187.47223	7.99779	3.614E-15	5.01E-16	1.896E-15	2.63E-16	3.812E-15	5.306E-16	1.551E-15	2.158E-16	GC
187.47144	7.95663	1.26E-15	3.092E-16	6.613E-16	1.623E-16	1.329E-15	3.266E-16	5.407E-16	1.329E-16	

RA	DEC	Flux$_{PL}$	Flux$_{PL}$ err	Flux$_{PL}$	Flux$_{PL}$ err	Flux$_{diskbb}$	Flux$_{diskbb}$ err	Flux$_{diskbb}$	Flux$_{diskbb}$ err	Flag
degrees	degrees	0.5–05 keV	0.5–5 keV	0.5–2 keV	0.5–2 keV	0.5–5 keV	0.5–5 keV	0.5–2 keV	0.5–2 keV	
187.47109	7.94715	1.176E-15	3.361E-16	6.171E-16	1.764E-16	1.24E-15	3.549E-16	5.046E-16	1.443E-16	
187.47044	7.99158	2.182E-15	4.974E-16	1.145E-15	2.611E-16	2.302E-15	5.255E-16	9.362E-16	2.137E-16	
187.47031	7.99906	4.211E-15	5.677E-16	2.21E-15	2.98E-16	4.442E-15	6.014E-16	1.807E-15	2.446E-16	
187.47021	7.96514	1.267E-15	3.667E-16	6.651E-16	1.925E-16	1.337E-15	3.872E-16	5.439E-16	1.575E-16	
187.47006	7.97202	2.931E-15	4.851E-16	1.538E-15	2.546E-16	3.092E-15	5.132E-16	1.258E-15	2.087E-16	GC
187.46972	8.03225	1.378E-14	1.615E-15	7.229E-15	8.478E-16	1.453E-14	1.713E-15	5.911E-15	6.965E-16	
187.46969	7.95261	1.781E-15	3.5E-16	9.348E-16	1.837E-16	1.879E-15	3.7E-16	7.644E-16	1.505E-16	GC
187.46921	8.01933	1.955E-15	3.068E-16	1.026E-15	1.61E-16	2.062E-15	3.246E-16	8.388E-16	1.32E-16	GC
187.46914	8.00449	1.652E-15	3.607E-16	8.671E-16	1.893E-16	1.743E-15	3.811E-16	7.09E-16	1.55E-16	GC
187.46883	8.00051	3.138E-15	4.583E-16	1.647E-15	2.406E-16	3.31E-15	4.853E-16	1.347E-15	1.973E-16	GC
187.46816	7.99314	3.255E-15	9.312E-16	1.708E-15	4.888E-16	3.434E-15	9.833E-16	1.397E-15	4.0E-16	
187.46788	8.01287	8.142E-16	2.197E-16	4.273E-16	1.153E-16	8.589E-16	2.32E-16	3.494E-16	9.436E-17	
187.46582	7.99676	3.14E-15	9.443E-16	1.648E-15	4.956E-16	3.312E-15	9.97E-16	1.347E-15	4.055E-16	GC
187.46582	8.03906	1.484E-15	3.375E-16	7.787E-16	1.771E-16	1.565E-15	3.566E-16	6.368E-16	1.45E-16	cg
187.46556	7.99996	4.169E-15	5.689E-16	2.188E-15	2.987E-16	4.398E-15	6.026E-16	1.789E-15	2.45E-16	GC
187.46548	7.9732	2.556E-15	4.065E-16	1.342E-15	2.134E-16	2.697E-15	4.301E-16	1.097E-15	1.749E-16	
187.46543	7.99196	1.386E-15	3.23E-16	7.272E-16	1.695E-16	1.462E-15	3.412E-16	5.946E-16	1.388E-16	GC
187.46507	8.00083	3.991E-15	1.047E-15	2.095E-15	5.497E-16	4.211E-15	1.106E-15	1.713E-15	4.499E-16	
187.46489	7.96636	2.547E-15	4.604E-16	1.337E-15	2.417E-16	2.687E-15	4.868E-16	1.093E-15	1.98E-16	
187.46478	7.95126	2.514E-15	4.854E-16	1.32E-15	2.548E-16	2.653E-15	5.131E-16	1.079E-15	2.087E-16	
187.46394	7.98809	2.077E-15	3.7E-16	1.09E-15	1.942E-16	2.191E-15	3.913E-16	8.914E-16	1.591E-16	GC
187.4634	8.05763	3.522E-15	9.376E-16	1.848E-15	4.921E-16	3.715E-15	9.901E-16	1.511E-15	4.027E-16	
187.46323	7.97408	1.036E-15	2.63E-16	5.438E-16	1.38E-16	1.093E-15	2.778E-16	4.446E-16	1.13E-16	
187.46315	8.04035	7.277E-15	9.138E-16	3.819E-15	4.797E-16	7.677E-15	9.687E-16	3.123E-15	3.939E-16	
187.46276	7.99645	3.37E-15	1.04E-15	1.768E-15	5.46E-16	3.555E-15	1.098E-15	1.446E-15	4.468E-16	GC
187.46225	7.98736	1.485E-15	3.464E-16	7.791E-16	1.818E-16	1.566E-15	3.66E-16	6.371E-16	1.489E-16	GC
187.462	8.00271	9.517E-15	1.144E-15	4.995E-15	6.005E-16	1.004E-14	1.213E-15	4.084E-15	4.932E-16	GC
187.46196	8.03652	2.067E-15	3.602E-16	1.085E-15	1.891E-16	2.18E-15	3.81E-16	8.869E-16	1.549E-16	
187.46183	7.9715	1.946E-15	3.683E-16	1.021E-15	1.933E-16	2.053E-15	3.893E-16	8.352E-16	1.583E-16	
187.46169	8.04609	1.037E-15	1.994E-16	5.444E-16	1.047E-16	1.094E-15	2.108E-16	4.451E-16	8.575E-17	
187.46132	8.01972	1.18E-15	2.378E-16	6.195E-16	1.248E-16	1.245E-15	2.513E-16	5.066E-16	1.022E-16	GC
187.46106	7.96407	2.045E-15	4.903E-16	1.073E-15	2.573E-16	2.157E-15	5.179E-16	8.774E-16	2.107E-16	

RA	DEC	Flux$_{PL}$	Flux$_{PL}$ err	Flux$_{PL}$	Flux$_{PL}$ err	Flux$_{diskbb}$	Flux$_{diskbb}$ err	Flux$_{diskbb}$	Flux$_{diskbb}$ err	Flag
degrees	degrees	0.5–05 keV	0.5–5 keV	0.5–2 keV	0.5–2 keV	0.5–5 keV	0.5–5 keV	0.5–2 keV	0.5–2 keV	
187.46101	8.00652	6.626E-16	2.395E-16	3.477E-16	1.257E-16	6.99E-16	2.528E-16	2.843E-16	1.028E-16	
187.46063	7.98888	3.413E-15	4.957E-16	1.791E-15	2.602E-16	3.601E-15	5.249E-16	1.465E-15	2.134E-16	
187.46004	8.00379	9.209E-15	1.108E-15	4.833E-15	5.817E-16	9.715E-15	1.175E-15	3.952E-15	4.778E-16	GC
187.45957	8.00999	1.863E-15	3.416E-16	9.778E-16	1.793E-16	1.966E-15	3.612E-16	7.996E-16	1.469E-16	
187.4594	7.97335	1.956E-15	3.712E-16	1.027E-15	1.949E-16	2.064E-15	3.925E-16	8.395E-16	1.596E-16	
187.45886	8.02188	1.453E-15	2.754E-16	7.628E-16	1.446E-16	1.533E-15	2.912E-16	6.237E-16	1.184E-16	
187.45878	7.99547	7.625E-15	9.791E-16	4.002E-15	5.14E-16	8.044E-15	1.038E-15	3.272E-15	4.22E-16	GC
187.45789	7.99961	1.864E-15	5.43E-16	9.785E-16	2.85E-16	1.967E-15	5.734E-16	8.001E-16	2.332E-16	bkg
187.45758	8.00714	1.066E-15	2.568E-16	5.596E-16	1.348E-16	1.125E-15	2.713E-16	4.576E-16	1.103E-16	
187.45639	7.98617	1.284E-15	3.313E-16	6.738E-16	1.739E-16	1.355E-15	3.499E-16	5.51E-16	1.423E-16	
187.45636	7.99033	1.616E-15	4.871E-16	8.479E-16	2.556E-16	1.704E-15	5.143E-16	6.934E-16	2.092E-16	bkg, GC
187.45612	7.99293	1.864E-15	4.042E-16	9.78E-16	2.121E-16	1.966E-15	4.271E-16	7.997E-16	1.737E-16	GC
187.45608	8.05566	8.278E-16	1.866E-16	4.344E-16	9.792E-17	8.732E-16	1.971E-16	3.552E-16	8.017E-17	
187.45568	7.96479	5.577E-15	7.49E-16	2.927E-15	3.932E-16	5.883E-15	7.936E-16	2.393E-15	3.227E-16	GC
187.45552	8.00358	1.52E-14	1.788E-15	7.979E-15	9.389E-16	1.604E-14	1.897E-15	6.524E-15	7.713E-16	
187.4555	8.03852	1.231E-15	2.732E-16	6.458E-16	1.434E-16	1.298E-15	2.886E-16	5.281E-16	1.174E-16	GC
187.45524	8.02964	1.959E-15	3.115E-16	1.028E-15	1.635E-16	2.067E-15	3.296E-16	8.408E-16	1.34E-16	
187.45509	8.05476	1.243E-15	3.058E-16	6.523E-16	1.605E-16	1.311E-15	3.23E-16	5.334E-16	1.314E-16	c
187.45507	8.0155	7.233E-16	2.621E-16	3.796E-16	1.376E-16	7.63E-16	2.766E-16	3.104E-16	1.125E-16	GC
187.45461	8.0076	8.406E-16	2.178E-16	4.411E-16	1.143E-16	8.867E-16	2.301E-16	3.607E-16	9.358E-17	GC
187.45438	7.99198	1.516E-15	4.455E-16	7.954E-16	2.338E-16	1.599E-15	4.703E-16	6.504E-16	1.913E-16	
187.45426	7.98095	1.501E-14	1.764E-15	7.878E-15	9.259E-16	1.584E-14	1.871E-15	6.442E-15	7.606E-16	
187.45416	7.99612	2.813E-15	4.659E-16	1.476E-15	2.446E-16	2.968E-15	4.929E-16	1.207E-15	2.005E-16	
187.45379	7.97948	1.727E-15	4.344E-16	9.066E-16	2.28E-16	1.822E-15	4.588E-16	7.413E-16	1.866E-16	GC
187.45375	8.01616	4.868E-16	2.097E-16	2.555E-16	1.101E-16	5.136E-16	2.213E-16	2.089E-16	9.004E-17	
187.45308	8.02145	1.113E-15	3.36E-16	5.843E-16	1.764E-16	1.175E-15	3.548E-16	4.778E-16	1.443E-16	
187.45261	7.9984	2.158E-15	4.141E-16	1.133E-15	2.174E-16	2.277E-15	4.378E-16	9.261E-16	1.781E-16	
187.45261	7.98706	1.902E-15	4.375E-16	9.983E-16	2.296E-16	2.007E-15	4.622E-16	8.163E-16	1.88E-16	
187.4525	7.99542	5.879E-15	8.373E-16	3.085E-15	4.395E-16	6.202E-15	8.866E-16	2.523E-15	3.605E-16	
187.45198	8.00991	1.552E-15	4.797E-16	8.146E-16	2.518E-16	1.638E-15	5.065E-16	6.661E-16	2.06E-16	bkg
187.45187	8.03341	9.416E-16	1.997E-16	4.942E-16	1.048E-16	9.933E-16	2.11E-16	4.041E-16	8.582E-17	
187.45155	8.00554	8.559E-16	3.339E-16	4.492E-16	1.752E-16	9.03E-16	3.524E-16	3.673E-16	1.434E-16	

RA	DEC	Flux$_{PL}$	Flux$_{PL}$ err	Flux$_{PL}$	Flux$_{PL}$ err	Flux$_{diskbb}$	Flux$_{diskbb}$ err	Flux$_{diskbb}$	Flux$_{diskbb}$ err	Flag
degrees	degrees	0.5–05 keV	0.5–5 keV	0.5–2 keV	0.5–2 keV	0.5–5 keV	0.5–5 keV	0.5–2 keV	0.5–2 keV	
187.45135	7.99231	3.511E-15	5.81E-16	1.842E-15	3.05E-16	3.703E-15	6.147E-16	1.507E-15	2.5E-16	
187.45113	8.00454	2.894E-15	1.093E-15	1.519E-15	5.735E-16	3.053E-15	1.153E-15	1.242E-15	4.692E-16	
187.45073	8.01639	1.485E-15	2.708E-16	7.794E-16	1.422E-16	1.567E-15	2.864E-16	6.373E-16	1.165E-16	
187.45034	7.99476	1.437E-15	4.375E-16	7.539E-16	2.296E-16	1.515E-15	4.619E-16	6.165E-16	1.879E-16	GC
187.45009	7.97628	6.514E-16	2.471E-16	3.419E-16	1.297E-16	6.872E-16	2.608E-16	2.795E-16	1.061E-16	GC
187.45006	7.98558	1.544E-15	3.654E-16	8.101E-16	1.918E-16	1.628E-15	3.86E-16	6.624E-16	1.57E-16	
187.44982	8.00233	8.39E-15	1.359E-15	4.403E-15	7.136E-16	8.851E-15	1.438E-15	3.6E-15	5.849E-16	bkg, GC
187.44947	7.99776	3.187E-15	7.794E-16	1.673E-15	4.091E-16	3.362E-15	8.233E-16	1.368E-15	3.349E-16	bkg
187.44946	8.01021	3.441E-15	5.418E-16	1.806E-15	2.844E-16	3.631E-15	5.734E-16	1.477E-15	2.332E-16	
187.44942	7.99556	1.316E-15	4.345E-16	6.906E-16	2.28E-16	1.388E-15	4.586E-16	5.647E-16	1.866E-16	
187.44941	7.98863	2.181E-15	4.321E-16	1.145E-15	2.268E-16	2.301E-15	4.567E-16	9.36E-16	1.858E-16	GC
187.44936	7.99283	2.546E-15	4.878E-16	1.336E-15	2.56E-16	2.686E-15	5.156E-16	1.093E-15	2.097E-16	
187.4492	8.00554	1.08E-15	4.194E-16	5.667E-16	2.201E-16	1.139E-15	4.427E-16	4.634E-16	1.801E-16	bkg
187.44894	7.99055	4.138E-15	5.985E-16	2.172E-15	3.142E-16	4.365E-15	6.337E-16	1.776E-15	2.577E-16	GC
187.44881	7.98298	1.431E-15	3.816E-16	7.51E-16	2.003E-16	1.51E-15	4.03E-16	6.141E-16	1.639E-16	
187.44873	8.02852	1.283E-15	2.503E-16	6.736E-16	1.314E-16	1.354E-15	2.645E-16	5.508E-16	1.076E-16	
187.44868	8.02199	1.486E-15	2.958E-16	7.798E-16	1.553E-16	1.568E-15	3.127E-16	6.377E-16	1.272E-16	
187.44867	8.0074	7.787E-15	9.761E-16	4.087E-15	5.124E-16	8.215E-15	1.035E-15	3.342E-15	4.207E-16	
187.44849	7.97868	1.056E-15	2.766E-16	5.542E-16	1.452E-16	1.114E-15	2.921E-16	4.531E-16	1.188E-16	
187.44765	8.00222	1.468E-14	1.999E-15	7.706E-15	1.049E-15	1.549E-14	2.117E-15	6.301E-15	8.609E-16	
187.44753	7.98658	1.101E-15	3.518E-16	5.777E-16	1.846E-16	1.161E-15	3.714E-16	4.724E-16	1.511E-16	GC
187.44716	8.01575	1.035E-15	2.408E-16	5.43E-16	1.264E-16	1.092E-15	2.544E-16	4.44E-16	1.035E-16	GC
187.4465	8.038	7.056E-16	2.272E-16	3.703E-16	1.193E-16	7.444E-16	2.399E-16	3.028E-16	9.758E-17	
187.44648	7.97605	1.775E-15	3.485E-16	9.316E-16	1.829E-16	1.873E-15	3.684E-16	7.617E-16	1.498E-16	GC
187.44604	8.03101	7.591E-16	1.834E-16	3.984E-16	9.629E-17	8.008E-16	1.938E-16	3.257E-16	7.882E-17	cg
187.44602	8.00373	1.909E-14	2.279E-15	1.002E-14	1.197E-15	2.014E-14	2.417E-15	8.192E-15	9.829E-16	
187.44598	7.99539	1.244E-15	4.573E-16	6.527E-16	2.4E-16	1.312E-15	4.827E-16	5.337E-16	1.964E-16	
187.44595	7.97969	5.781E-15	7.478E-16	3.034E-15	3.926E-16	6.099E-15	7.925E-16	2.481E-15	3.222E-16	GC
187.44517	7.98295	1.698E-15	3.643E-16	8.91E-16	1.912E-16	1.791E-15	3.85E-16	7.286E-16	1.566E-16	
187.44418	7.99237	2.183E-15	4.252E-16	1.146E-15	2.232E-16	2.303E-15	4.494E-16	9.37E-16	1.828E-16	
187.44399	7.99015	1.972E-15	3.845E-16	1.035E-15	2.018E-16	2.081E-15	4.064E-16	8.464E-16	1.653E-16	
187.44364	7.99437	1.596E-15	4.416E-16	8.377E-16	2.318E-16	1.684E-15	4.663E-16	6.85E-16	1.897E-16	

RA	DEC	Flux$_{PL}$	Flux$_{PL}$ err	Flux$_{PL}$	Flux$_{PL}$ err	Flux$_{diskbb}$	Flux$_{diskbb}$ err	Flux$_{diskbb}$	Flux$_{diskbb}$ err	Flag
degrees	degrees	0.5–05 keV	0.5–5 keV	0.5–2 keV	0.5–2 keV	0.5–5 keV	0.5–5 keV	0.5–2 keV	0.5–2 keV	
187.44349	8.01867	1.4E-15	3.691E-16	7.345E-16	1.937E-16	1.476E-15	3.898E-16	6.006E-16	1.586E-16	
187.44335	8.02061	9.575E-16	2.925E-16	5.025E-16	1.535E-16	1.01E-15	3.088E-16	4.109E-16	1.256E-16	
187.44327	7.96177	1.513E-15	3.766E-16	7.939E-16	1.977E-16	1.596E-15	3.978E-16	6.492E-16	1.618E-16	
187.44317	8.02419	3.127E-15	4.345E-16	1.641E-15	2.281E-16	3.299E-15	4.602E-16	1.342E-15	1.871E-16	GC
187.44288	7.97872	2.145E-15	3.947E-16	1.126E-15	2.072E-16	2.263E-15	4.174E-16	9.204E-16	1.697E-16	
187.44288	8.02239	9.685E-16	2.28E-16	5.083E-16	1.197E-16	1.022E-15	2.408E-16	4.156E-16	9.796E-17	
187.4425	7.99815	2.877E-14	3.436E-15	1.51E-14	1.804E-15	3.035E-14	3.644E-15	1.234E-14	1.482E-15	
187.44231	7.98961	3.307E-15	5.058E-16	1.736E-15	2.655E-16	3.489E-15	5.354E-16	1.419E-15	2.177E-16	GC
187.44205	8.02309	1.151E-15	2.418E-16	6.039E-16	1.269E-16	1.214E-15	2.555E-16	4.938E-16	1.039E-16	GC
187.44202	7.98761	1.379E-14	1.642E-15	7.238E-15	8.622E-16	1.455E-14	1.742E-15	5.918E-15	7.082E-16	
187.44131	8.02414	5.759E-15	7.224E-16	3.022E-15	3.793E-16	6.075E-15	7.659E-16	2.471E-15	3.114E-16	GC
187.44093	8.00475	4.389E-15	8.924E-16	2.303E-15	4.684E-16	4.63E-15	9.432E-16	1.883E-15	3.836E-16	
187.44087	7.98851	2.841E-15	5.138E-16	1.491E-15	2.697E-16	2.997E-15	5.433E-16	1.219E-15	2.21E-16	
187.44078	7.96204	2.823E-15	5.147E-16	1.482E-15	2.702E-16	2.978E-15	5.442E-16	1.211E-15	2.213E-16	GC
187.4406	7.9692	3.141E-15	4.772E-16	1.648E-15	2.505E-16	3.313E-15	5.051E-16	1.348E-15	2.054E-16	
187.44054	8.02476	2.578E-15	3.766E-16	1.353E-15	1.977E-16	2.719E-15	3.987E-16	1.106E-15	1.621E-16	c
187.44023	7.99462	1.036E-15	3.306E-16	5.437E-16	1.735E-16	1.093E-15	3.49E-16	4.446E-16	1.42E-16	GC
187.44004	7.99341	7.402E-16	2.678E-16	3.885E-16	1.406E-16	7.809E-16	2.827E-16	3.177E-16	1.15E-16	GC
187.43988	8.02479	2.353E-15	3.58E-16	1.235E-15	1.879E-16	2.483E-15	3.789E-16	1.01E-15	1.541E-16	c
187.43985	8.0164	6.022E-15	7.613E-16	3.161E-15	3.997E-16	6.353E-15	8.07E-16	2.584E-15	3.281E-16	
187.43968	8.03374	3.105E-15	4.284E-16	1.629E-15	2.249E-16	3.275E-15	4.537E-16	1.332E-15	1.845E-16	
187.43941	7.99174	2.559E-15	4.791E-16	1.343E-15	2.515E-16	2.7E-15	5.065E-16	1.098E-15	2.06E-16	
187.4392	7.98576	2.349E-15	5.288E-16	1.233E-15	2.775E-16	2.478E-15	5.587E-16	1.008E-15	2.272E-16	
187.43919	7.98781	1.87E-15	4.258E-16	9.813E-16	2.235E-16	1.973E-15	4.499E-16	8.024E-16	1.83E-16	
187.4391	7.99342	1.712E-15	3.853E-16	8.983E-16	2.022E-16	1.806E-15	4.071E-16	7.346E-16	1.656E-16	GC
187.439	8.0046	7.377E-15	9.98E-16	3.872E-15	5.239E-16	7.782E-15	1.057E-15	3.166E-15	4.299E-16	
187.43899	7.99449	2.037E-15	4.138E-16	1.069E-15	2.172E-16	2.149E-15	4.373E-16	8.741E-16	1.779E-16	GC
187.43893	8.00817	1.986E-15	3.847E-16	1.042E-15	2.019E-16	2.095E-15	4.067E-16	8.521E-16	1.654E-16	
187.43846	8.02502	4.56E-16	1.961E-16	2.393E-16	1.029E-16	4.811E-16	2.069E-16	1.957E-16	8.417E-17	
187.43825	7.94748	1.69E-15	4.533E-16	8.871E-16	2.379E-16	1.783E-15	4.788E-16	7.254E-16	1.947E-16	
187.43823	8.01061	4.851E-16	2.33E-16	2.546E-16	1.223E-16	5.117E-16	2.459E-16	2.082E-16	1.0E-16	bkg
187.43763	7.99741	3.476E-15	5.127E-16	1.824E-15	2.692E-16	3.667E-15	5.428E-16	1.492E-15	2.207E-16	GC

RA	DEC	Flux$_{PL}$	Flux$_{PL}$ err	Flux$_{PL}$	Flux$_{PL}$ err	Flux$_{diskbb}$	Flux$_{diskbb}$ err	Flux$_{diskbb}$	Flux$_{diskbb}$ err	Flag
degrees	degrees	0.5–05 keV	0.5–5 keV	0.5–2 keV	0.5–2 keV	0.5–5 keV	0.5–5 keV	0.5–2 keV	0.5–2 keV	
187.43755	8.03682	1.953E-15	3.235E-16	1.025E-15	1.698E-16	2.061E-15	3.422E-16	8.383E-16	1.392E-16	
187.43733	8.01012	9.528E-16	3.289E-16	5.0E-16	1.726E-16	1.005E-15	3.472E-16	4.089E-16	1.412E-16	bkg
187.4368	8.0013	1.961E-15	3.695E-16	1.029E-15	1.94E-16	2.068E-15	3.907E-16	8.414E-16	1.589E-16	
187.43675	8.05909	1.082E-15	2.89E-16	5.676E-16	1.517E-16	1.141E-15	3.052E-16	4.641E-16	1.241E-16	
187.4361	8.00019	4.432E-15	6.117E-16	2.326E-15	3.212E-16	4.676E-15	6.48E-16	1.902E-15	2.635E-16	
187.43583	7.95621	2.789E-15	5.128E-16	1.464E-15	2.692E-16	2.942E-15	5.422E-16	1.197E-15	2.205E-16	
187.43494	8.03965	9.25E-16	3.232E-16	4.855E-16	1.696E-16	9.758E-16	3.412E-16	3.97E-16	1.388E-16	
187.43483	7.99499	9.399E-16	3.097E-16	4.933E-16	1.626E-16	9.915E-16	3.27E-16	4.033E-16	1.33E-16	GC
187.43415	8.01161	3.25E-15	4.72E-16	1.705E-15	2.478E-16	3.428E-15	4.997E-16	1.395E-15	2.032E-16	GC
187.43395	8.05697	1.141E-15	3.083E-16	5.99E-16	1.618E-16	1.204E-15	3.256E-16	4.898E-16	1.324E-16	
187.43375	7.97804	6.339E-15	8.32E-16	3.327E-15	4.368E-16	6.688E-15	8.817E-16	2.72E-15	3.585E-16	GC
187.43343	8.02091	1.92E-15	6.929E-16	1.008E-15	3.636E-16	2.026E-15	7.313E-16	8.241E-16	2.975E-16	GC
187.43332	7.99764	5.769E-15	7.61E-16	3.028E-15	3.995E-16	6.086E-15	8.064E-16	2.476E-15	3.279E-16	GC
187.43302	8.04708	9.812E-15	1.741E-15	5.149E-15	9.141E-16	1.035E-14	1.842E-15	4.211E-15	7.49E-16	
187.43289	8.05309	6.225E-16	2.126E-16	3.267E-16	1.116E-16	6.567E-16	2.244E-16	2.672E-16	9.127E-17	
187.43269	7.96569	3.056E-15	6.56E-16	1.604E-15	3.443E-16	3.223E-15	6.932E-16	1.311E-15	2.819E-16	GC
187.43259	7.99911	1.524E-15	3.262E-16	8.0E-16	1.712E-16	1.608E-15	3.447E-16	6.542E-16	1.402E-16	GC
187.43248	7.9543	4.081E-15	5.936E-16	2.142E-15	3.116E-16	4.305E-15	6.285E-16	1.751E-15	2.556E-16	
187.43245	7.95842	1.884E-15	4.218E-16	9.886E-16	2.214E-16	1.987E-15	4.456E-16	8.084E-16	1.812E-16	
187.43237	8.01162	2.423E-15	4.0E-16	1.272E-15	2.1E-16	2.556E-15	4.232E-16	1.04E-15	1.721E-16	
187.43185	8.01442	3.082E-15	4.394E-16	1.617E-15	2.307E-16	3.251E-15	4.653E-16	1.323E-15	1.892E-16	
187.43142	7.98188	1.251E-15	3.454E-16	6.566E-16	1.813E-16	1.32E-15	3.647E-16	5.369E-16	1.484E-16	
187.43135	7.99651	9.206E-15	1.133E-15	4.832E-15	5.946E-16	9.712E-15	1.201E-15	3.951E-15	4.883E-16	
187.43102	8.03289	3.245E-15	1.372E-15	1.703E-15	7.203E-16	3.423E-15	1.448E-15	1.392E-15	5.892E-16	
187.43047	8.06057	2.408E-15	3.556E-16	1.264E-15	1.867E-16	2.54E-15	3.765E-16	1.033E-15	1.531E-16	
187.43035	8.04347	3.949E-15	1.056E-15	2.072E-15	5.543E-16	4.166E-15	1.115E-15	1.695E-15	4.536E-16	cg
187.42999	7.98177	8.768E-16	3.016E-16	4.601E-16	1.583E-16	9.249E-16	3.184E-16	3.762E-16	1.295E-16	
187.42988	8.00911	1.635E-15	3.318E-16	8.582E-16	1.741E-16	1.725E-15	3.507E-16	7.018E-16	1.426E-16	
187.42951	8.01101	4.92E-15	6.426E-16	2.582E-15	3.374E-16	5.19E-15	6.81E-16	2.111E-15	2.769E-16	GC
187.42938	8.03832	5.656E-16	2.037E-16	2.968E-16	1.069E-16	5.966E-16	2.15E-16	2.427E-16	8.744E-17	
187.42923	7.98238	1.66E-15	4.276E-16	8.711E-16	2.244E-16	1.751E-15	4.516E-16	7.123E-16	1.837E-16	
187.42922	7.95775	1.853E-15	4.776E-16	9.726E-16	2.507E-16	1.955E-15	5.044E-16	7.953E-16	2.052E-16	

RA	DEC	Flux$_{PL}$	Flux$_{PL}$ err	Flux$_{PL}$	Flux$_{PL}$ err	Flux$_{diskbb}$	Flux$_{diskbb}$ err	Flux$_{diskbb}$	Flux$_{diskbb}$ err	Flag
degrees	degrees	0.5–05 keV	0.5–5 keV	0.5–2 keV	0.5–2 keV	0.5–5 keV	0.5–5 keV	0.5–2 keV	0.5–2 keV	
187.42911	7.97957	2.741E-15	4.239E-16	1.439E-15	2.225E-16	2.892E-15	4.486E-16	1.176E-15	1.824E-16	GC
187.42765	8.04481	1.107E-15	2.893E-16	5.812E-16	1.518E-16	1.168E-15	3.055E-16	4.752E-16	1.243E-16	cg
187.42639	8.00218	2.382E-14	2.741E-15	1.25E-14	1.439E-15	2.512E-14	2.908E-15	1.022E-14	1.182E-15	GC
187.42624	8.02524	8.389E-16	2.54E-16	4.403E-16	1.333E-16	8.85E-16	2.682E-16	3.6E-16	1.091E-16	
187.42603	7.95057	1.932E-14	2.25E-15	1.014E-14	1.181E-15	2.038E-14	2.387E-15	8.29E-15	9.707E-16	
187.42509	8.00396	3.428E-15	9.751E-16	1.799E-15	5.118E-16	3.616E-15	1.03E-15	1.471E-15	4.188E-16	
187.42509	7.98477	2.247E-15	5.916E-16	1.179E-15	3.105E-16	2.371E-15	6.248E-16	9.643E-16	2.541E-16	
187.42493	7.98013	8.643E-15	1.066E-15	4.536E-15	5.595E-16	9.118E-15	1.13E-15	3.709E-15	4.594E-16	
187.4247	8.02168	1.214E-15	5.16E-16	6.369E-16	2.708E-16	1.28E-15	5.446E-16	5.208E-16	2.215E-16	
187.42371	7.97253	2.651E-15	5.299E-16	1.391E-15	2.781E-16	2.797E-15	5.6E-16	1.138E-15	2.278E-16	
187.4236	8.00046	1.141E-15	3.101E-16	5.989E-16	1.628E-16	1.204E-15	3.275E-16	4.897E-16	1.332E-16	GC
187.4235	8.01364	1.252E-15	2.448E-16	6.57E-16	1.285E-16	1.321E-15	2.587E-16	5.372E-16	1.052E-16	GC
187.42342	8.01731	2.819E-15	4.042E-16	1.479E-15	2.122E-16	2.974E-15	4.28E-16	1.21E-15	1.74E-16	
187.42342	8.01238	1.763E-15	3.018E-16	9.252E-16	1.584E-16	1.86E-15	3.192E-16	7.565E-16	1.298E-16	GC
187.42336	8.00398	9.616E-15	1.175E-15	5.047E-15	6.171E-16	1.014E-14	1.246E-15	4.127E-15	5.068E-16	GC
187.42334	8.01633	4.788E-15	6.26E-16	2.513E-15	3.287E-16	5.051E-15	6.634E-16	2.055E-15	2.698E-16	
187.42306	7.97556	3.503E-15	5.104E-16	1.839E-15	2.679E-16	3.696E-15	5.404E-16	1.503E-15	2.197E-16	
187.42266	7.98455	5.573E-15	7.268E-16	2.925E-15	3.816E-16	5.879E-15	7.702E-16	2.392E-15	3.132E-16	
187.42255	7.98166	4.623E-15	6.389E-16	2.426E-15	3.354E-16	4.877E-15	6.767E-16	1.984E-15	2.752E-16	
187.42249	8.03555	1.296E-15	2.427E-16	6.799E-16	1.274E-16	1.367E-15	2.566E-16	5.56E-16	1.044E-16	
187.42242	7.95737	4.764E-15	6.814E-16	2.5E-15	3.577E-16	5.026E-15	7.216E-16	2.044E-15	2.934E-16	
187.42164	7.99188	1.541E-15	3.508E-16	8.085E-16	1.841E-16	1.625E-15	3.706E-16	6.611E-16	1.508E-16	
187.42092	8.00086	3.262E-15	4.767E-16	1.712E-15	2.503E-16	3.441E-15	5.048E-16	1.4E-15	2.053E-16	GC
187.42092	8.0487	1.13E-15	2.425E-16	5.932E-16	1.273E-16	1.192E-15	2.562E-16	4.851E-16	1.042E-16	GC
187.42088	7.96233	5.111E-14	5.779E-15	2.683E-14	3.034E-15	5.392E-14	6.133E-15	2.193E-14	2.493E-15	GC
187.42039	7.99527	4.636E-15	6.212E-16	2.433E-15	3.261E-16	4.891E-15	6.582E-16	1.989E-15	2.676E-16	
187.41845	8.04004	1.038E-15	2.243E-16	5.446E-16	1.177E-16	1.095E-15	2.37E-16	4.453E-16	9.639E-17	
187.4175	7.9957	2.842E-15	4.442E-16	1.492E-15	2.332E-16	2.998E-15	4.701E-16	1.22E-15	1.912E-16	GC
187.41745	7.9748	3.895E-15	1.231E-15	2.044E-15	6.463E-16	4.109E-15	1.3E-15	1.671E-15	5.288E-16	GC
187.41707	7.99093	7.935E-15	9.778E-16	4.164E-15	5.133E-16	8.371E-15	1.037E-15	3.405E-15	4.215E-16	GC
187.41536	7.98263	1.332E-15	3.337E-16	6.992E-16	1.751E-16	1.406E-15	3.525E-16	5.718E-16	1.434E-16	GC
187.41524	7.99126	1.669E-15	3.863E-16	8.76E-16	2.027E-16	1.761E-15	4.081E-16	7.163E-16	1.66E-16	GC

RA	DEC	Flux$_{PL}$	Flux$_{PL}$ err	Flux$_{PL}$	Flux$_{PL}$ err	Flux$_{diskbb}$	Flux$_{diskbb}$ err	Flux$_{diskbb}$	Flux$_{diskbb}$ err	Flag
degrees	degrees	0.5–05 keV	0.5–5 keV	0.5–2 keV	0.5–2 keV	0.5–5 keV	0.5–5 keV	0.5–2 keV	0.5–2 keV	
187.4145	8.02878	3.725E-15	5.157E-16	1.955E-15	2.707E-16	3.929E-15	5.462E-16	1.598E-15	2.221E-16	
187.41433	8.01041	1.964E-15	3.362E-16	1.031E-15	1.765E-16	2.072E-15	3.556E-16	8.428E-16	1.446E-16	
187.41324	7.98868	5.07E-15	6.782E-16	2.661E-15	3.56E-16	5.348E-15	7.185E-16	2.176E-15	2.922E-16	GC
187.41314	7.99475	2.744E-15	4.254E-16	1.44E-15	2.233E-16	2.895E-15	4.502E-16	1.178E-15	1.831E-16	GC
187.41275	7.95364	3.945E-15	6.239E-16	2.07E-15	3.275E-16	4.162E-15	6.602E-16	1.693E-15	2.685E-16	GC
187.41118	7.96551	4.998E-15	7.051E-16	2.623E-15	3.702E-16	5.272E-15	7.468E-16	2.145E-15	3.037E-16	GC
187.41049	8.04092	9.766E-16	2.477E-16	5.125E-16	1.3E-16	1.03E-15	2.617E-16	4.191E-16	1.064E-16	
187.41046	7.99152	1.844E-15	6.811E-16	9.68E-16	3.575E-16	1.946E-15	7.189E-16	7.915E-16	2.924E-16	GC
187.40974	8.00833	4.488E-15	5.954E-16	2.355E-15	3.126E-16	4.735E-15	6.308E-16	1.926E-15	2.565E-16	
187.40946	8.00356	1.139E-15	2.684E-16	5.978E-16	1.408E-16	1.202E-15	2.835E-16	4.889E-16	1.153E-16	GC
187.40914	8.04296	3.241E-15	4.739E-16	1.701E-15	2.488E-16	3.419E-15	5.017E-16	1.391E-15	2.04E-16	
187.40886	7.97714	4.37E-15	6.995E-16	2.293E-15	3.672E-16	4.61E-15	7.401E-16	1.875E-15	3.01E-16	
187.40746	7.97934	9.39E-15	1.173E-15	4.928E-15	6.156E-16	9.905E-15	1.243E-15	4.029E-15	5.055E-16	GC
187.40731	8.01271	4.215E-15	5.721E-16	2.212E-15	3.003E-16	4.446E-15	6.06E-16	1.809E-15	2.464E-16	
187.40654	8.02118	1.26E-15	2.856E-16	6.61E-16	1.499E-16	1.329E-15	3.018E-16	5.405E-16	1.227E-16	
187.40084	7.96944	2.097E-15	5.37E-16	1.101E-15	2.818E-16	2.212E-15	5.672E-16	9.0E-16	2.307E-16	
187.40001	8.04156	1.133E-15	3.287E-16	5.946E-16	1.725E-16	1.195E-15	3.47E-16	4.862E-16	1.412E-16	
187.39989	8.01516	1.817E-15	3.279E-16	9.536E-16	1.721E-16	1.917E-15	3.467E-16	7.798E-16	1.41E-16	
187.39635	7.99997	1.587E-15	4.386E-16	8.326E-16	2.302E-16	1.674E-15	4.632E-16	6.809E-16	1.884E-16	
187.39564	8.01346	4.682E-15	6.13E-16	2.457E-15	3.218E-16	4.939E-15	6.496E-16	2.009E-15	2.641E-16	
187.3938	8.00892	2.03E-14	2.345E-15	1.065E-14	1.231E-15	2.141E-14	2.488E-15	8.71E-15	1.012E-15	GC
187.39363	7.98102	2.415E-14	2.781E-15	1.268E-14	1.46E-15	2.548E-14	2.951E-15	1.036E-14	1.2E-15	GC
187.38648	7.98249	9.36E-15	1.17E-15	4.912E-15	6.141E-16	9.874E-15	1.24E-15	4.017E-15	5.042E-16	
187.38616	7.98217	1.31E-14	1.754E-15	6.876E-15	9.21E-16	1.382E-14	1.859E-15	5.622E-15	7.558E-16	
187.38539	7.98108	4.655E-15	9.364E-16	2.443E-15	4.915E-16	4.911E-15	9.897E-16	1.998E-15	4.025E-16	c, GC

Appendix B

X-ray and optical data for the globular cluster sources in NGC 4472

TABLE B.1: The X-ray and optical properties of the GC LMXBs. The X-ray flux and luminosity are for the 0.5–5 keV range. The X, RZ and VCS subscripts denote the RA and DEC for X-ray, RZ01 and VCS observations respectively. z and g are the magnitudes of the sources in the VCS catalogue and B, V and R are the magnitudes of the RZ01 catalogue. The designation "err" denotes parameter error values.

RA_X	DEC_X	$Flux_{PL}$	$Flux_{PL}$ err	Flag	RA_{VCS}	DEC_{VCS}	z	z err	g	g err	g-z	RA_{RZ}	DEC_{RZ}	V	B-V	V-R	B-R	B err	V err	R err
degrees	degrees	0.5–5 keV	0.5–5 keV		degrees	degrees						degrees	degrees							
187.42088	7.96233	5.111E-14	5.779E-15									187.42096	7.96246	21.55	0.85	0.59	1.44	0.05	0.02	0.02
187.39363	7.98102	2.415E-14	2.781E-15		187.39368	7.98105	20.13	0.02	21.24	0.01	1.12									
187.42639	8.00218	2.382E-14	2.741E-15		187.42631	8.00214	19.57	0.01	21.0	0.01	1.43	187.42647	8.00233	20.55	0.82	0.55	1.37	0.02	0.01	0.01
187.3938	8.00892	2.03E-14	2.345E-15		187.39382	8.00896	22.18	0.04	23.11	0.08	0.93									
187.42336	8.00398	9.616E-15	1.175E-15		187.42325	8.00392	21.84	0.03	23.38	0.02	1.53	187.42337	8.0041	22.88	1.21	0.55	1.76	0.26	0.07	0.09
187.462	8.00271	9.517E-15	1.144E-15		187.4619	8.00269	22.7	0.02	24.12	0.03	1.42									
187.40746	7.97934	9.39E-15	1.173E-15									187.40752	7.97947	22.03	0.75	0.49	1.24	0.06	0.03	0.04
187.46004	8.00379	9.209E-15	1.108E-15		187.45994	8.00374	20.16	0.02	21.71	0.03	1.55	187.46008	8.00396	21.2	0.88	0.56	1.43	0.05	0.02	0.03
187.44982	8.00233	8.39E-15	1.359E-15	bkg	187.44972	8.00222	19.41	0.02	20.82	0.03	1.41									
187.41707	7.99093	7.935E-15	9.778E-16		187.41699	7.99086	20.44	0.02	22.06	0.03	1.62									
187.45878	7.99547	7.625E-15	9.791E-16		187.45878	7.99539	20.6	0.01	21.75	0.02	1.15	187.45892	7.9956	21.3	0.76	0.51	1.26	0.04	0.03	0.03
187.43375	7.97804	6.339E-15	8.32E-16		187.43367	7.97794	22.84	0.06	24.45	0.04	1.62									
187.44595	7.97969	5.781E-15	7.478E-16		187.44588	7.97961	20.85	0.02	22.27	0.03	1.43									
187.43332	7.99764	5.769E-15	7.61E-16		187.43324	7.99757	22.26	0.02	23.61	0.04	1.35									
187.44131	8.02414	5.759E-15	7.224E-16		187.4412	8.02413	23.73	0.34	25.09	0.08	1.37									
187.45568	7.96479	5.577E-15	7.49E-16									187.45572	7.96497	20.82	0.71	0.52	1.23	0.02	0.01	0.01
187.41324	7.98868	5.07E-15	6.782E-16		187.41309	7.98874	19.91	0.01	21.29	0.02	1.38	187.41327	7.98894	20.88	0.79	0.57	1.36	0.03	0.01	0.01
187.41118	7.96551	4.998E-15	7.051E-16									187.41133	7.96565	22.94	0.84	0.42	1.26	0.15	0.07	0.09
187.42951	8.01101	4.92E-15	6.426E-16		187.42931	8.01097	20.45	0.01	21.5	0.02	1.05	187.42945	8.01116	21.13	0.68	0.45	1.13	0.03	0.02	0.02
187.47602	8.00271	4.855E-15	6.329E-16									187.47611	8.00288	21.34	0.55	0.46	1.01	0.04	0.02	0.02
187.38539	7.98108	4.655E-15	9.364E-16	c	187.38533	7.98115	22.8	0.06	24.24	0.04	1.44									
187.46556	7.99996	4.169E-15	5.689E-16		187.46546	7.99993	19.36	0.01	20.8	0.01	1.44									
187.44894	7.99055	4.138E-15	5.985E-16		187.44886	7.99043	21.74	0.02	23.23	0.03	1.49									
187.48483	8.00848	4.122E-15	5.459E-16									187.48489	8.00865	21.86	0.95	0.6	1.55	0.06	0.02	0.03
187.41275	7.95364	3.945E-15	6.239E-16									187.41284	7.95371	21.43	0.86	0.55	1.41	0.04	0.02	0.02
187.41745	7.9748	3.895E-15	1.231E-15									187.41765	7.97499	22.62	0.66	0.47	1.13	0.1	0.05	0.07
187.47223	7.99779	3.614E-15	5.01E-16									187.47231	7.99785	21.98	0.53	0.3	0.83	0.05	0.03	0.05
187.47234	8.00724	3.509E-15	4.779E-16		187.47224	8.0072	19.08	0.02	20.54	0.02	1.47	187.47238	8.00741	20.03	0.86	0.56	1.42	0.01	0.01	0.01
187.43763	7.99741	3.476E-15	5.127E-16		187.43756	7.99727	20.82	0.02	22.37	0.02	1.55									
187.46276	7.99645	3.37E-15	1.04E-15		187.46286	7.99632	19.81	0.01	21.28	0.03	1.48	187.46303	7.99654	20.98	0.88	0.57	1.45	0.03	0.02	0.02
187.44231	7.98961	3.307E-15	5.058E-16		187.44223	7.98957	23.22	0.41	23.76	0.05	0.54									
187.42092	8.00086	3.262E-15	4.767E-16		187.42084	8.00083	20.9	0.02	22.29	0.02	1.4	187.42101	8.00103	21.89	0.73	0.54	1.28	0.07	0.03	0.04
187.43415	8.01161	3.25E-15	4.72E-16		187.43405	8.01159	19.95	0.01	21.38	0.02	1.43									
187.47229	8.0526	3.172E-15	4.433E-16									187.47238	8.05279	22.01	0.76	0.58	1.34	0.06	0.03	0.03
187.46582	7.99676	3.14E-15	9.443E-16		187.46584	7.99667	22.4	0.02	23.93	0.03	1.53									
187.46883	8.00051	3.138E-15	4.583E-16		187.46873	8.00045	22.63	0.05	24.2	0.03	1.57									
187.44317	8.02419	3.127E-15	4.345E-16		187.44308	8.02404	23.48	0.05	24.68	0.03	1.2									
187.43269	7.96569	3.056E-15	6.56E-16									187.43294	7.96593	20.59	0.87	0.54	1.4	0.02	0.01	0.01

RA_X	DEC_X	$Flux_{PL}$	$Flux_{PL}$ err	Flag	RA_{VCS}	DEC_{VCS}	z	z err	g	g err	g-z	RA_{RZ}	DEC_{RZ}	V	B-V	V-R	B-R	B err	V err	R err
degrees	degrees	0.5–5 keV	0.5–5 keV		degrees	degrees						degrees	degrees							
187.47006	7.97202	2.931E-15	4.851E-16									187.4701	7.97213	20.97	0.83	0.59	1.42	0.03	0.01	0.01
187.4175	7.9957	2.842E-15	4.442E-16		187.41742	7.99564	19.92	0.01	21.23	0.01	1.31	187.4176	7.99583	20.82	0.8	0.56	1.35	0.02	0.01	0.01
187.44078	7.96204	2.823E-15	5.147E-16									187.44091	7.96226	21.41	0.97	0.59	1.55	0.05	0.02	0.02
187.41314	7.99475	2.744E-15	4.254E-16		187.41307	7.9947	21.61	0.02	23.05	0.02	1.44									
187.42911	7.97957	2.741E-15	4.239E-16		187.42901	7.97948	20.36	0.02	21.72	0.02	1.36	187.42918	7.97969	21.23	0.85	0.44	1.29	0.04	0.02	0.02
187.48301	7.95625	2.273E-15	4.133E-16									187.48301	7.95649	20.74	0.93	0.58	1.51	0.02	0.01	0.01
187.44941	7.98863	2.181E-15	4.321E-16		187.4494	7.98857	20.5	0.03	21.85	0.03	1.35	187.44954	7.98879	21.62	0.59	0.48	1.07	0.06	0.03	0.04
187.46394	7.98809	2.077E-15	3.7E-16									187.46397	7.98823	21.99	0.85	0.54	1.39	0.08	0.03	0.04
187.43899	7.99449	2.037E-15	4.138E-16		187.43886	7.99442	21.95	0.02	23.6	0.03	1.65									
187.46921	8.01933	1.955E-15	3.068E-16		187.46911	8.01926	22.85	0.03	24.32	0.05	1.47									
187.43343	8.02091	1.92E-15	6.929E-16		187.43337	8.0209	21.12	0.02	22.78	0.02	1.66									
187.45612	7.99293	1.864E-15	4.042E-16		187.45606	7.99289	20.88	0.02	22.31	0.02	1.42									
187.41046	7.99152	1.844E-15	6.811E-16		187.41033	7.99147	21.39	0.03	22.83	0.02	1.44									
187.46969	7.95261	1.781E-15	3.5E-16									187.46981	7.95284	21.82	0.64	0.42	1.06	0.05	0.03	0.03
187.44648	7.97605	1.775E-15	3.485E-16		187.44634	7.97604	20.59	0.02	22.25	0.03	1.66	187.4465	7.97625	21.69	0.83	0.56	1.39	0.06	0.03	0.03
187.42342	8.01238	1.763E-15	3.018E-16		187.42335	8.01232	20.62	0.02	22.05	0.02	1.44									
187.45379	7.97948	1.727E-15	4.344E-16		187.45386	7.97938	21.2	0.01	22.7	0.02	1.5									
187.4391	7.99342	1.712E-15	3.853E-16		187.43902	7.9934	20.43	0.01	21.88	0.02	1.45									
187.49021	7.9924	1.708E-15	3.068E-16									187.49016	7.99268	21.44	0.61	0.51	1.12	0.03	0.02	0.02
187.41524	7.99126	1.669E-15	3.863E-16		187.4151	7.99117	21.43	0.02	22.61	0.02	1.18									
187.46914	8.00449	1.652E-15	3.607E-16		187.46901	8.00449	20.67	0.01	22.12	0.01	1.45	187.46917	8.00467	21.77	0.8	0.55	1.35	0.06	0.03	0.03
187.45636	7.99033	1.616E-15	4.871E-16	bkg	187.45633	7.99025	20.55	0.01	22.05	0.03	1.5	187.45652	7.99047	21.81	0.88	0.65	1.52	0.08	0.03	0.04
187.48287	8.00096	1.573E-15	2.989E-16									187.48287	8.00112	21.89	0.92	0.57	1.49	0.07	0.03	0.03
187.43259	7.99911	1.524E-15	3.262E-16		187.43251	7.99904	20.42	0.01	21.61	0.02	1.2									
187.46225	7.98736	1.485E-15	3.464E-16		187.46202	7.98729	21.62	0.03	23.22	0.03	1.6									
187.45034	7.99476	1.437E-15	4.375E-16		187.45024	7.99478	19.37	0.01	20.62	0.02	1.25									
187.46543	7.99196	1.386E-15	3.23E-16		187.46522	7.9919	22.49	0.02	23.9	0.03	1.41									
187.41536	7.98263	1.332E-15	3.337E-16		187.41523	7.98275	23.42	0.3	24.74	0.13	1.32									
187.4235	8.01364	1.252E-15	2.448E-16		187.4234	8.01364	21.3	0.02	22.33	0.02	1.04	187.42356	8.01384	22.06	0.46	0.34	0.8	0.07	0.04	0.06
187.4555	8.03852	1.231E-15	2.732E-16									187.45559	8.03869	20.59	0.86	0.59	1.45	0.02	0.01	0.01
187.46132	8.01972	1.18E-15	2.378E-16		187.46133	8.01967	22.69	0.02	24.33	0.04	1.65									
187.44205	8.02309	1.151E-15	2.418E-16		187.44214	8.02292	22.12	0.46	23.53	0.04	1.41									
187.4236	8.00046	1.141E-15	3.101E-16		187.42352	8.00044	19.84	0.02	21.51	0.02	1.67	187.42369	8.00065	21.01	0.95	0.61	1.57	0.04	0.02	0.02
187.40946	8.00356	1.139E-15	2.684E-16		187.40924	8.00342	21.22	0.02	22.62	0.02	1.4									
187.42092	8.0487	1.13E-15	2.425E-16		187.42075	8.0488	21.73	0.02	23.31	0.03	1.59									
187.44753	7.98658	1.101E-15	3.518E-16		187.44736	7.98646	21.26	0.02	22.64	0.02	1.39	187.44752	7.98668	22.47	0.63	0.36	0.99	0.12	0.06	0.08
187.44023	7.99462	1.036E-15	3.306E-16		187.44014	7.99453	21.83	0.04	23.06	0.02	1.23									
187.44716	8.01575	1.035E-15	2.408E-16		187.44701	8.01579	20.41	0.02	21.62	0.02	1.2	187.44718	8.01601	21.41	0.66	0.55	1.21	0.05	0.03	0.03
187.43483	7.99499	9.399E-16	3.097E-16		187.43471	7.99488	21.88	0.03	23.53	0.03	1.65									
187.45461	8.0076	8.406E-16	2.178E-16		187.45449	8.00753	22.08	0.03	23.42	0.04	1.34									
187.44004	7.99341	7.402E-16	2.678E-16		187.44	7.99333	22.62	0.04	24.06	0.05	1.44									
187.45507	8.0155	7.233E-16	2.621E-16		187.45493	8.01541	20.37	0.01	21.87	0.02	1.49	187.4551	8.01561	21.54	0.73	0.57	1.3	0.05	0.03	0.03
187.45009	7.97628	6.514E-16	2.471E-16		187.44992	7.97634	20.41	0.02	21.7	0.02	1.29	187.45009	7.97657	21.37	0.71	0.43	1.14	0.04	0.02	0.03

Bibliography

Anders, P., Fritze-von Alvensleben, U., & de Grijs, R. 2003, Ap&SS, 284, 937

Angelini, L., Loewenstein, M., & Mushotzky, R. F. 2001, ApJ, 557, L35

Arkani-Hamed, N., Dimopoulos, S., & Dvali, G. 1998, Physics Letters B, 429, 263

Begelman, M. C. 2002, ApJ, 568, L97

Begelman, M. C., King, A. R., & Pringle, J. E. 2006, MNRAS, 370, 399

Beswick, R. J., Riley, J. D., Marti-Vidal, I., Pedlar, A., Muxlow, T. W. B., McDonald, A. R., Wills, K. A., Fenech, D., & Argo, M. K. 2006, MNRAS, 369, 1221

Bildsten, L. & Deloye, C. J. 2004, ApJ, 607, L119

Bland, J. & Tully, B. 1988, Nature, 334, 43

Bogomazov, A. I. & Lipunov, V. M. 2008, Astronomy Reports, 52, 299

Branch, D., Livio, M., Yungelson, L. R., Boffi, F. R., & Baron, E. 1995, PASP, 107, 1019

Brassington, N. J., Fabbiano, G., Blake, S., Zezas, A., Angelini, L., Davies, R. L., Gallagher, J., Kalogera, V., Kim, D.-W., King, A. R., Kundu, A., Trinchieri, G., & Zepf, S. 2010, ApJ, 725, 1805

Brassington, N. J., Fabbiano, G., Kim, D.-W., Zezas, A., Zepf, S., Kundu, A., Angelini, L., Davies, R. L., Gallagher, J., Kalogera, V., Fragos, T., King, A. R., Pellegrini, S., & Trinchieri, G. 2008, ApJS, 179, 142

—. 2009, ApJS, 181, 605

Bravo, E., Domínguez, I., Badenes, C., Piersanti, L., & Straniero, O. 2010, ApJ, 711, L66

Brinchmann, J., Charlot, S., White, S. D. M., Tremonti, C., Kauffmann, G., Heckman, T., & Brinkmann, J. 2004, MNRAS, 351, 1151

Brocksopp, C., Fender, R. P., McCollough, M., Pooley, G. G., Rupen, M. P., Hjellming, R. M., de la Force, C. J., Spencer, R. E., Muxlow, T. W. B., Garrington, S. T., & Trushkin, S. 2002, MNRAS, 331, 765

Brodie, J. P. & Strader, J. 2006, ARA&A, 44, 193

Brunthaler, A., Menten, K. M., Reid, M. J., Henkel, C., Bower, G. C., & Falcke, H. 2009, The Astronomer's Telegram, 2078, 1

Bruzual, G. & Charlot, S. 2003, MNRAS, 344, 1000

Caballero-García, M. D. & Fabian, A. C. 2010, MNRAS, 402, 2559

Calvelo, D. E., Fender, R. P., Russell, D. M., Gallo, E., Corbel, S., Tzioumis, A. K., Bell, M. E., Lewis, F., & Maccarone, T. J. 2010, MNRAS, 409, 839

Canterna, R. 1976, AJ, 81, 228

Chaty, S. 2011, in Astronomical Society of the Pacific Conference Series, Vol. 447, Evolution of Compact Binaries, ed. L. Schmidtobreick, M. R. Schreiber, & C. Tappert, 29

Cherepashchuk, A. M. 1981, MNRAS, 194, 761

Clark, G. W. 1975, ApJ, 199, L143

Colbert, E. J. M., Heckman, T. M., Ptak, A. F., Strickland, D. K., & Weaver, K. A. 2004, ApJ, 602, 231

Colbert, E. J. M. & Mushotzky, R. F. 1999, ApJ, 519, 89

Colbert, E. J. M. & Ptak, A. F. 2002, ApJS, 143, 25

Coleiro, A. & Chaty, S. 2013, ApJ, 764, 185

Corbel, S., Nowak, M. A., Fender, R. P., Tzioumis, A. K., & Markoff, S. 2003, A&A, 400, 1007

Côté, P., Blakeslee, J. P., Ferrarese, L., Jordán, A., Mei, S., Merritt, D., Milosavljević, M., Peng, E. W., Tonry, J. L., & West, M. J. 2004, ApJS, 153, 223

Côté, P., McLaughlin, D. E., Cohen, J. G., & Blakeslee, J. P. 2003, ApJ, 591, 850

Crampton, D., Cowley, A. P., & Hutchings, J. B. 1980, ApJ, 235, L131

Davis, D. S. & Mushotzky, R. F. 2004, ApJ, 604, 653

Dehnen, W. & King, A. 2006, MNRAS, 367, L29

Dewangan, G. C., Griffiths, R. E., & Rao, A. R. 2006, ApJ, 641, L125

Dewangan, G. C., Miyaji, T., Griffiths, R. E., & Lehmann, I. 2004, ApJ, 608, L57

Di Stefano, R. & Kong, A. K. H. 2003, ApJ, 592, 884

—. 2004, ApJ, 609, 710

Di Stefano, R., Kong, A. K. H., Greiner, J., Primini, F. A., Garcia, M. R., Barmby, P., Massey, P., Hodge, P. W., Williams, B. F., Murray, S. S., Curry, S., & Russo, T. A. 2004, ApJ, 610, 247

Dickey, J. M. & Lockman, F. J. 1990, ARA&A, 28, 215

Dirsch, B., Richtler, T., Geisler, D., Forte, J. C., Bassino, L. P., & Gieren, W. P. 2003, AJ, 125, 1908

Dirsch, B., Richtler, T., Geisler, D., Gebhardt, K., Hilker, M., Alonso, M. V., Forte, J. C., Grebel, E. K., Infante, L., Larsen, S., Minniti, D., & Rejkuba, M. 2004, AJ, 127, 2114

Dubner, G. M., Holdaway, M., Goss, W. M., & Mirabel, I. F. 1998, AJ, 116, 1842

Dufour, P. 2011, Stars with Unusual Compositions: Carbon and Oxygen in Cool White Dwarfs, ed. D. W. Hoard, 53–88

Ebisawa, K., Życki, P., Kubota, A., Mizuno, T., & Watarai, K.-y. 2003, ApJ, 597, 780

Esin, A. A., McClintock, J. E., Drake, J. J., Garcia, M. R., Haswell, C. A., Hynes, R. I., & Muno, M. P. 2001, ApJ, 555, 483

Esin, A. A., McClintock, J. E., & Narayan, R. 1997, ApJ, 489, 865

Fabbiano, G. 2006, ARA&A, 44, 323

Fabbiano, G., Kim, D.-W., Fragos, T., Kalogera, V., King, A. R., Angelini, L., Davies, R. L., Gallagher, J. S., Pellegrini, S., Trinchieri, G., Zepf, S. E., & Zezas, A. 2006, ApJ, 650, 879

Fabbiano, G. & White, N. E. 2006, Compact stellar X-ray sources in normal galaxies, ed. W. H. G. Lewin & M. van der Klis, 475–506

Fabian, A. C., Pringle, J. E., & Rees, M. J. 1975, MNRAS, 172, 15P

Fabian, A. C. & Rees, M. J. 1979, MNRAS, 187, 13P

Fabrika, S. 2004, Astrophysics and Space Physics Reviews, 12, 1

Fabrika, S. & Mescheryakov, A. 2001, in IAU Symposium, Vol. 205, Galaxies and their Constituents at the Highest Angular Resolutions, ed. R. T. Schilizzi, 268

Falcke, H., Körding, E., & Markoff, S. 2004, A&A, 414, 895

Farrell, S. A., Webb, N. A., Barret, D., Godet, O., & Rodrigues, J. M. 2009, Nature, 460, 73

Feldman, P. A., Purton, C. R., Stiff, T., & Kwok, S. 1978, IAU Circ., 3258, 1

Fender, R. 2006, Jets from X-ray binaries, ed. W. H. G. Lewin & M. van der Klis, 381–419

Fender, R., Corbel, S., Tzioumis, T., Tingay, S., Brocksopp, C., & Gallo, E. 2002, The Astronomer's Telegram, 107, 1

Fender, R. P., Belloni, T. M., & Gallo, E. 2004, MNRAS, 355, 1105

Fenech, D. M., Muxlow, T. W. B., Beswick, R. J., Pedlar, A., & Argo, M. K. 2008, MNRAS, 391, 1384

Feng, H. & Kaaret, P. 2006, ApJ, 653, 536

Feng, H. & Soria, R. 2011, New A Rev., 55, 166

Fiedler, R. L., Johnston, K. J., Spencer, J. H., Waltman, E. B., Florkowski, S. R., Matsakis, D. N., Josties, F. J., Angerhofer, P. E., Klepczynski, W. J., & McCarthy, D. D. 1987, AJ, 94, 1244

Frank, J., King, A., & Raine, D. J. 2002, Accretion Power in Astrophysics: Third Edition

Fraser, M., Smartt, S. J., Crockett, M., Mattila, S., Stephens, A. G.-Y. A., & Roth, K. 2009, The Astronomer's Telegram, 2131, 1

Freedman, W. L., Hughes, S. M., Madore, B. F., Mould, J. R., Lee, M. G., Stetson, P., Kennicutt, R. C., Turner, A., Ferrarese, L., Ford, H., Graham, J. A., Hill, R., Hoessel, J. G., Huchra, J., & Illingworth, G. D. 1994, ApJ, 427, 628

Frontera, F., Amati, L., Zdziarski, A. A., Belloni, T., Del Sordo, S., Masetti, N., Orlandini, M., & Palazzi, E. 2003, ApJ, 592, 1110

Fruchter, A. S. & Hook, R. N. 2002, PASP, 114, 144

Gallo, E., Fender, R. P., Miller-Jones, J. C. A., Merloni, A., Jonker, P. G., Heinz, S., Maccarone, T. J., & van der Klis, M. 2006, MNRAS, 370, 1351

Gallo, E., Fender, R. P., & Pooley, G. G. 2003, MNRAS, 344, 60

Gehrels, N. 1986, ApJ, 303, 336

Giacconi, R., Branduardi, G., Briel, U., Epstein, A., Fabricant, D., Feigelson, E., Forman, W., Gorenstein, P., Grindlay, J., Gursky, H., Harnden, F. R., Henry, J. P., Jones, C., Kellogg, E., Koch, D., Murray, S., Schreier, E., Seward, F., Tananbaum, H., Topka, K., Van Speybroeck, L., Holt, S. S., Becker, R. H., Boldt, E. A., Serlemitsos, P. J., Clark, G., Canizares, C., Markert, T., Novick, R., Helfand, D., & Long, K. 1979, ApJ, 230, 540

Giacconi, R., Gorenstein, P., Gursky, H., & Waters, J. R. 1967, ApJ, 148, L119

Giacconi, R. & Gursky, H., eds. 1974, Astrophysics and Space Science Library, Vol. 43, X-ray astronomy

Giacconi, R., Gursky, H., Paolini, F. R., & Rossi, B. B. 1962, Physical Review Letters, 9, 439

Gilfanov, M. 2004, MNRAS, 349, 146

Gladstone, J. C., Roberts, T. P., & Done, C. 2009, MNRAS, 397, 1836

Gnedin, O. Y., Maccarone, T. J., Psaltis, D., & Zepf, S. E. 2009, ApJ, 705, L168

Gorenstein, P., Fabricant, D., Topka, K., Harnden, Jr., F. R., & Tucker, W. H. 1978, ApJ, 224, 718

Grillmair, C. J., Forbes, D. A., Brodie, J. P., & Elson, R. A. W. 1999, AJ, 117, 167

Grimm, H.-J., Gilfanov, M., & Sunyaev, R. 2002, A&A, 391, 923

—. 2003, Chinese Journal of Astronomy and Astrophysics Supplement, 3, 257

Grindlay, J. E. 1987, in IAU Symposium, Vol. 125, The Origin and Evolution of Neutron Stars, ed. D. J. Helfand & J.-H. Huang, 173–184

Gürkan, M. A., Freitag, M., & Rasio, F. A. 2004, ApJ, 604, 632

Hachisu, I., Kato, M., & Nomoto, K. 2010, ApJ, 724, L212

Hannikainen, D., Wu, K., Campbell-Wilson, D., Hunstead, R., Lovell, J., McIntyre, V., Reynolds, J., Soria, R., & Tzioumis, T. 2001, in ESA Special Publication, Vol. 459, Exploring the Gamma-Ray Universe, ed. A. Gimenez, V. Reglero, & C. Winkler, 291–294

Harmon, B. A., Wilson, C. A., Zhang, S. N., Paciesas, W. S., Fishman, G. J., Hjellming, R. M., Rupen, M. P., Scott, D. M., Briggs, M. S., & Rubin, B. C. 1995, Nature, 374, 703

Harris, W. E. 1996, AJ, 112, 1487

Hasinger, G. & van der Klis, M. 1989, A&A, 225, 79

Heger, A. & Woosley, S. E. 2002, ApJ, 567, 532

Heintz, W. D. 1978, Geophysics and Astrophysics Monographs, 15

Helfand, D. J. 1984, PASP, 96, 913

Herschel, W. 1802, Royal Society of London Philosophical Transactions Series I, 92, 477

—. 1803, Royal Society of London Philosophical Transactions Series I, 93, 339

Hills, J. G. 1976, MNRAS, 175, 1P

Hillwig, T. C. & Gies, D. R. 2008, ApJ, 676, L37

Hjellming, R. M. & Johnston, K. J. 1981, ApJ, 246, L141

Hjellming, R. M. & Rupen, M. P. 1995, Nature, 375, 464

Homan, J., Belloni, T., Wijnands, R., van der Klis, M., Swank, J., Smith, E., Pereira, D., & Markwardt, C. 2007a, The Astronomer's Telegram, 1144, 1

Homan, J., van der Klis, M., Fridriksson, J. K., Remillard, R. A., Wijnands, R., Méndez, M., Lin, D., Altamirano, D., Casella, P., Belloni, T. M., & Lewin, W. H. G. 2010, ApJ, 719, 201

Homan, J., van der Klis, M., Wijnands, R., Belloni, T., Fender, R., Klein-Wolt, M., Casella, P., Méndez, M., Gallo, E., Lewin, W. H. G., & Gehrels, N. 2007b, ApJ, 656, 420

Homan, J., Wijnands, R., Altamirano, D., & Belloni, T. 2007c, The Astronomer's Telegram, 1165, 1

Humphrey, P. J., Fabbiano, G., Elvis, M., Church, M. J., & Bałucińska-Church, M. 2003, MNRAS, 344, 134

Hung, L.-W., Hickox, R. C., Boroson, B. S., & Vrtilek, S. D. 2010, ApJ, 720, 1202

Hut, P., McMillan, S., Goodman, J., Mateo, M., Phinney, E. S., Pryor, C., Richer, H. B., Verbunt, F., & Weinberg, M. 1992, PASP, 104, 981

Hut, P. & Paczynski, B. 1984, ApJ, 284, 675

Irwin, J., Bregman, J., & Brink, T. 2009, in Bulletin of the American Astronomical Society, Vol. 41, American Astronomical Society Meeting Abstracts #213, #437.07

Irwin, J. A. 2006, MNRAS, 371, 1903

Irwin, J. A., Brink, T. G., Bregman, J. N., & Roberts, T. P. 2010, ApJ, 712, L1

Irwin, M. J., Belokurov, V., Evans, N. W., Ryan-Weber, E. V., de Jong, J. T. A., Koposov, S., Zucker, D. B., Hodgkin, S. T., Gilmore, G., Prema, P., Hebb, L., Begum, A., Fellhauer, M., Hewett, P. C., Kennicutt, Jr., R. C., Wilkinson, M. I., Bramich, D. M., Vidrih, S., Rix, H.-W., Beers, T. C., Barentine, J. C., Brewington, H., Harvanek, M., Krzesinski, J., Long, D., Nitta, A., & Snedden, S. A. 2007, ApJ, 656, L13

Ivanova, N., Chaichenets, S., Fregeau, J., Heinke, C. O., Lombardi, Jr., J. C., & Woods, T. E. 2010, ApJ, 717, 948

Ivanova, N., Fragos, T., Kim, D.-W., Fabbiano, G., Avendano Nandez, J. L., Lombardi, J. C., Sivakoff, G. R., Voss, R., & Jordán, A. 2012, ApJ, 760, L24

Ivanova, N., Rasio, F. A., Lombardi, Jr., J. C., Dooley, K. L., & Proulx, Z. F. 2005, ApJ, 621, L109

Jenkins, L. P., Roberts, T. P., Warwick, R. S., Kilgard, R. E., & Ward, M. J. 2004, MNRAS, 349, 404

—. 2005, MNRAS, 357, 401

Jonker, P. G., Bassa, C. G., Nelemans, G., Steeghs, D., Torres, M. A. P., Maccarone, T. J., Hynes, R. I., Greiss, S., Clem, J., Dieball, A., Mikles, V. J., Britt, C. T., Gossen, L., Collazzi, A. C., Wijnands, R., In't Zand, J. J. M., Méndez, M., Rea, N., Kuulkers, E., Ratti, E. M., van Haaften, L. M., Heinke, C., Özel, F., Groot, P. J., & Verbunt, F. 2011, ApJS, 194, 18

Jordán, A., Côté, P., Ferrarese, L., Blakeslee, J. P., Mei, S., Merritt, D., Milosavljević, M., Peng, E. W., Tonry, J. L., & West, M. J. 2004, ApJ, 613, 279

Jordán, A., Peng, E. W., Blakeslee, J. P., Côté, P., Eyheramendy, S., Ferrarese, L., Mei, S., Tonry, J. L., & West, M. J. 2009, ApJS, 180, 54

Juett, A. M. 2005, ApJ, 621, L25

Kahabka, P. 2006, Advances in Space Research, 38, 2836

Kahabka, P. & van den Heuvel, E. P. J. 1997, ARA&A, 35, 69

Kajava, J. J. E. & Poutanen, J. 2009, MNRAS, 398, 1450

Kalogera, V., King, A. R., & Rasio, F. A. 2004, ApJ, 601, L171

Kalogera, V. & Webbink, R. F. 1998, ApJ, 493, 351

Kim, D.-W. & Fabbiano, G. 2004, ApJ, 611, 846

Kim, D.-W., Fabbiano, G., Brassington, N. J., Fragos, T., Kalogera, V., Zezas, A., Jordán, A., Sivakoff, G. R., Kundu, A., Zepf, S. E., Angelini, L., Davies, R. L., Gallagher, J. S., Juett, A. M., King, A. R., Pellegrini, S., Sarazin, C. L., & Trinchieri, G. 2009, ApJ, 703, 829

Kim, D.-W., Fabbiano, G., Kalogera, V., King, A. R., Pellegrini, S., Trinchieri, G., Zepf, S. E., Zezas, A., Angelini, L., Davies, R. L., & Gallagher, J. S. 2006a, ApJ, 652, 1090

Kim, E., Kim, D.-W., Fabbiano, G., Lee, M. G., Park, H. S., Geisler, D., & Dirsch, B. 2006b, ApJ, 647, 276

King, A. R. 2003, ArXiv Astrophysics e-prints

—. 2009, MNRAS, 393, L41

King, A. R., Davies, M. B., Ward, M. J., Fabbiano, G., & Elvis, M. 2001, ApJ, 552, L109

King, A. R., Taam, R. E., & Begelman, M. C. 2000, ApJ, 530, L25

Kirk, J. G. & Trumper, J. E. 1983, in Accretion-Driven Stellar X-ray Sources, ed. W. H. G. Lewin & E. P. J. van den Heuvel, 261–285

Kobayashi, Y., Kubota, A., Nakazawa, K., Takahashi, T., & Makishima, K. 2003, PASJ, 55, 273

Kong, A. K. H. & Chiang, Y.-K. 2009, The Astronomer's Telegram, 2080, 1

Körding, E., Falcke, H., & Markoff, S. 2002, A&A, 382, L13

Kozai, Y. 1962, AJ, 67, 591

Krishan, V. & Mahajan, S. M. 2008, in Turbulence, Dynamos, Accretion Disks, Pulsars and Collective Plasma Processes, ed. S. S. Hasan, R. T. Gangadhara, & V. Krishan, 233

Kronberg, P. P., Biermann, P., & Schwab, F. R. 1981, ApJ, 246, 751

Kronberg, P. P. & Sramek, R. A. 1985, Science, 227, 28

Kubota, A., Makishima, K., & Done, C. 2004, Progress of Theoretical Physics Supplement, 155, 19

Kubota, A., Makishima, K., & Ebisawa, K. 2001, ApJ, 560, L147

Kulkarni, S. R., Hut, P., & McMillan, S. 1993, Nature, 364, 421

Kundu, A., Maccarone, T. J., & Zepf, S. E. 2002, ApJ, 574, L5

—. 2007, ApJ, 662, 525

Kundu, A., Maccarone, T. J., Zepf, S. E., & Puzia, T. H. 2003, ApJ, 589, L81

Kundu, A. & Whitmore, B. C. 2001, AJ, 121, 2950

Kuulkers, E., Fender, R. P., Spencer, R. E., Davis, R. J., & Morison, I. 1999, MNRAS, 306, 919

Kuulkers, E. & van der Klis, M. 1995, A&A, 303, 801

Lada, C. J. 2006, ApJ, 640, L63

Lasota, J.-P. 2001, New A Rev., 45, 449

Lee, H. M. 1995, MNRAS, 272, 605

Lee, M. G., Park, H. S., Kim, E., Hwang, H. S., Kim, S. C., & Geisler, D. 2008, ApJ, 682, 135

Li, Z.-M., Zhang, F.-H., & Han, Z.-W. 2006, Chinese J. Astron. Astrophys., 6, 669

Liu, J. 2011, ApJS, 192, 10

Liu, J.-F. & Bregman, J. N. 2005, ApJS, 157, 59

Liu, Q. Z. & Mirabel, I. F. 2005, A&A, 429, 1125

Liu, Q. Z., van Paradijs, J., & van den Heuvel, E. P. J. 2000, A&AS, 147, 25

—. 2001, A&A, 368, 1021

—. 2005, A&A, 442, 1135

—. 2006, A&A, 455, 1165

—. 2007, A&A, 469, 807

Long, K. S., Helfand, D. J., & Grabelsky, D. A. 1981, ApJ, 248, 925

Long, K. S. & van Speybroeck, L. P. 1983, in Accretion-Driven Stellar X-ray Sources, ed. W. H. G. Lewin & E. P. J. van den Heuvel, 141

Lumb, D. H., Schartel, N., & Jansen, F. A. 2012, Optical Engineering, 51, 011009

Maccarone, T. J. 2004, MNRAS, 351, 1049

Maccarone, T. J., Kundu, A., & Zepf, S. E. 2003, ApJ, 586, 814

—. 2004, ApJ, 606, 430

Maccarone, T. J., Kundu, A., Zepf, S. E., Piro, A. L., & Bildsten, L. 2005, MNRAS, 364, L61

Maccarone, T. J., Kundu, A., Zepf, S. E., & Rhode, K. L. 2007, Nature, 445, 183

—. 2010, MNRAS, 409, L84

—. 2011, MNRAS, 410, 1655

Macri, L. M., Huchra, J. P., Stetson, P. B., Silbermann, N. A., Freedman, W. L., Kennicutt, R. C., Mould, J. R., Madore, B. F., Bresolin, F., Ferrarese, L., Ford, H. C., Graham, J. A., Gibson, B. K., Han, M., Harding, P., Hill, R. J., Hoessel, J. G., Hughes, S. M. G., Kelson, D. D., Illingworth, G. D., Phelps, R. L., Prosser, C. F., Rawson, D. M., Saha, A., Sakai, S., & Turner, A. 1999, ApJ, 521, 155

Madej, O. K., Jonker, P. G., Fabian, A. C., Pinto, C., Verbunt, F., & de Plaa, J. 2010, MNRAS, 407, L11

Maraschi, L., Treves, A., & van den Heuvel, E. P. J. 1976, Nature, 259, 292

Margon, B. 1984, ARA&A, 22, 507

Margon, B., Ford, H. C., Katz, J. I., Kwitter, K. B., Ulrich, R. K., Stone, R. P. S., & Klemola, A. 1979, ApJ, 230, L41

Markoff, S., Falcke, H., & Fender, R. 2001, A&A, 372, L25

Mashchenko, S., Couchman, H. M. P., & Sills, A. 2005, ApJ, 624, 726

McClintock, J. E. & Remillard, R. A. 2006, Black hole binaries, ed. W. H. G. Lewin & M. van der Klis, 157–213

McDonald, A. R., Muxlow, T. W. B., Wills, K. A., Pedlar, A., & Beswick, R. J. 2002, MNRAS, 334, 912

Merloni, A., Heinz, S., & di Matteo, T. 2003, MNRAS, 345, 1057

Middleton, M. J., Roberts, T. P., Done, C., & Jackson, F. E. 2011, MNRAS, 411, 644

Miller, J. M. 2005, Ap&SS, 300, 227

Miller, J. M., Fabbiano, G., Miller, M. C., & Fabian, A. C. 2003, ApJ, 585, L37

Miller, J. M., Zezas, A., Fabbiano, G., & Schweizer, F. 2004, ApJ, 609, 728

Miller, M. C. & Hamilton, D. P. 2002, MNRAS, 330, 232

Mineo, S., Gilfanov, M., & Sunyaev, R. 2012, MNRAS, 419, 2095

Mitsuda, K., Inoue, H., Koyama, K., Makishima, K., Matsuoka, M., Ogawara, Y., Suzuki, K., Tanaka, Y., Shibazaki, N., & Hirano, T. 1984, PASJ, 36, 741

Mitsuda, K., Inoue, H., Nakamura, N., & Tanaka, Y. 1989, PASJ, 41, 97

Monet, D. & et al. 1998, VizieR Online Data Catalog, 1252, 0

Muxlow, T. W. B., Beswick, R. J., Garrington, S. T., Pedlar, A., Fenech, D. M., Argo, M. K., van Eymeren, J., Ward, M., Zezas, A., & Brunthaler, A. 2010, MNRAS, 404, L109

Muxlow, T. W. B., Beswick, R. J., Pedlar, A., Fenech, D., Argo, M. K., Ward, M. J., & Zezas, A. 2009, The Astronomer's Telegram, 2073, 1

Muxlow, T. W. B., Pedlar, A., Wilkinson, P. N., Axon, D. J., Sanders, E. M., & de Bruyn, A. G. 1994, MNRAS, 266, 455

Narayan, R. 1996, ApJ, 462, 136

Neilsen, J., Lee, J. C., Nowak, M. A., Dennerl, K., & Vrtilek, S. D. 2009, ApJ, 696, 182

Nowak, M. A. 1995, PASP, 107, 1207

Okajima, T., Ebisawa, K., & Kawaguchi, T. 2006, ApJ, 652, L105

Pakull, M. W., Soria, R., & Motch, C. 2010, Nature, 466, 209

Paolillo, M., Fabbiano, G., Peres, G., & Kim, D.-W. 2002, ApJ, 565, 883

Paragi, Z., Fejes, I., Vermeulen, R. C., Schilizzi, R. T., Spencer, R. E., & Stirling, A. M. 2001, in IAU Symposium, Vol. 205, Galaxies and their Constituents at the Highest Angular Resolutions, ed. R. T. Schilizzi, 266

Peacock, M. B., Zepf, S. E., Kundu, A., Maccarone, T. J., Rhode, K. L., Salzer, J. J., Waters, C. Z., Ciardullo, R., Gronwall, C., & Stern, D. 2012, ApJ, 759, 126

Popham, R. & Sunyaev, R. 2001, ApJ, 547, 355

Portegies Zwart, S. F., Dewi, J., & Maccarone, T. 2004, MNRAS, 355, 413

Portegies Zwart, S. F. & McMillan, S. L. W. 2002, ApJ, 576, 899

Poutanen, J., Lipunova, G., Fabrika, S., Butkevich, A. G., & Abolmasov, P. 2007, MNRAS, 377, 1187

Predehl, P., Burwitz, V., Paerels, F., & Trümper, J. 2000, A&A, 357, L25

Pringle, J. E. 1981, ARA&A, 19, 137

Proga, D., Stone, J. M., & Drew, J. E. 1998, MNRAS, 295, 595

Psaltis, D., Lamb, F. K., & Miller, G. S. 1995, ApJ, 454, L137

Quataert, E. & Narayan, R. 1999, ApJ, 520, 298

Rappaport, S. & van den Heuvel, E. P. J. 1982, in IAU Symposium, Vol. 98, Be Stars, ed. M. Jaschek & H.-G. Groth, 327–344

Rappaport, S. A., Podsiadlowski, P., & Pfahl, E. 2005, MNRAS, 356, 401

Remillard, R. A. & McClintock, J. E. 2006, ARA&A, 44, 49

Rhode, K. L. & Zepf, S. E. 2001, AJ, 121, 210

Ripamonti, E. & Mapelli, M. 2012, MNRAS, 423, 1144

Roberts, T. P. 2007, Ap&SS, 311, 203

Roberts, T. P., Fabbiano, G., Luo, B., Kim, D.-W., Strader, J., Middleton, M. J., Brodie, J. P., Fragos, T., Gallagher, J. S., Kalogera, V., King, A. R., & Zezas, A. 2012, ApJ, 760, 135

Roberts, T. P., Kilgard, R. E., Warwick, R. S., Goad, M. R., & Ward, M. J. 2006, MNRAS, 371, 1877

Roberts, T. P., Warwick, R. S., Ward, M. J., Goad, M. R., & Jenkins, L. P. 2005, MNRAS, 357, 1363

Roberts, T. P., Warwick, R. S., Ward, M. J., & Murray, S. S. 2002, MNRAS, 337, 677

Rodriguez, J., Hannikainen, D. C., Shaw, S. E., Pooley, G., Corbel, S., Tagger, M., Mirabel, I. F., Belloni, T., Cabanac, C., Cadolle Bel, M., Chenevez, J., Kretschmar, P., Lehto, H. J., Paizis, A., Varnière, P., & Vilhu, O. 2008, ApJ, 675, 1436

Romero, G. E., Torres, D. F., Kaufman Bernadó, M. M., & Mirabel, I. F. 2003, A&A, 410, L1

Rosswog, S., Ramirez-Ruiz, E., & Hix, W. R. 2009, ApJ, 695, 404

Sarazin, C. L., Irwin, J. A., & Bregman, J. N. 2000, ApJ, 544, L101

—. 2001, ApJ, 556, 533

Scaife, A. M. M. & Heald, G. H. 2012, MNRAS, 423, L30

Seaquist, E. R., Gregory, P. C., & Crane, P. C. 1978, IAU Circ., 3256, 2

Shakura, N. I. & Sunyaev, R. A. 1973, A&A, 24, 337

Shih, I. C., Maccarone, T. J., Kundu, A., & Zepf, S. E. 2008, MNRAS, 386, 2075

Shklovsky, I. S. 1967, ApJ, 148, L1

Sigurdsson, S. & Hernquist, L. 1993, Nature, 364, 423

Silk, J. & Arons, J. 1975, ApJ, 200, L131

Sivakoff, G. R., Jordán, A., Sarazin, C. L., Blakeslee, J. P., Côté, P., Ferrarese, L., Juett, A. M., Mei, S., & Peng, E. W. 2007, ApJ, 660, 1246

Sivakoff, G. R., Kraft, R. P., Jordán, A., Juett, A. M., Evans, D. A., Forman, W. R., Hardcastle, M. J., Sarazin, C. L., Birkinshaw, M., Brassington, N. J., Croston, J. H., Harris, W. E., Jones, C., Murray, S. S., Raychaudhury, S., Woodley, K. A., & Worrall, D. M. 2008, ApJ, 677, L27

Soria, R., Baldi, A., Risaliti, G., Fabbiano, G., King, A., La Parola, V., & Zezas, A. 2007, MNRAS, 379, 1313

Soria, R., Pakull, M. W., Broderick, J. W., Corbel, S., & Motch, C. 2010, MNRAS, 409, 541

Soulie, E. 1997, in Astronomical Society of the Pacific Conference Series, Vol. 130, The Third Pacific Rim Conference on Recent Development on Binary Star Research, ed. K.-C. Leung, 291

Steele, M. M., Zepf, S. E., Kundu, A., Maccarone, T. J., Rhode, K. L., & Salzer, J. J. 2011, ApJ, 739, 95

Stephenson, C. B. & Sanduleak, N. 1977, ApJS, 33, 459

Stevens, J. A., Hannikainen, D. C., Wu, K., Hunstead, R. W., & McKay, D. J. 2003, MNRAS, 342, 623

Stobbart, A.-M., Roberts, T. P., & Wilms, J. 2006, MNRAS, 368, 397

Strader, J., Chomiuk, L., Maccarone, T. J., Miller-Jones, J. C. A., & Seth, A. C. 2012, Nature, 490, 71

Strickland, D. K., Ponman, T. J., & Stevens, I. R. 1997, A&A, 320, 378

Swartz, D. A., Ghosh, K. K., Tennant, A. F., & Wu, K. 2004, ApJS, 154, 519

Swartz, D. A., Soria, R., & Tennant, A. F. 2008, ApJ, 684, 282

Taam, R. E. & van den Heuvel, E. P. J. 1986, ApJ, 305, 235

Tanaka, Y., Inoue, H., & Holt, S. S. 1994, PASJ, 46, L37

Tauris, T. M. & van den Heuvel, E. P. J. 2006, Formation and evolution of compact stellar X-ray sources, ed. W. H. G. Lewin & M. van der Klis, 623–665

Tavani, M., Bulgarelli, A., Piano, G., Sabatini, S., Striani, E., Evangelista, Y., Trois, A., Pooley, G., Trushkin, S., Nizhelskij, N. A., McCollough, M., Koljonen, K. I. I., Pucella, G., Giuliani, A., Chen, A. W., Costa, E., Vittorini, V., Trifoglio, M., Gianotti, F., Argan, A., Barbiellini, G., Caraveo, P., Cattaneo, P. W., Cocco, V., Contessi, T., D'Ammando, F., Del Monte, E., de Paris, G., Di Cocco, G., di Persio, G., Donnarumma, I., Feroci, M., Ferrari, A., Fuschino, F., Galli, M., Labanti, C., Lapshov, I., Lazzarotto, F., Lipari, P., Longo, F., Mattaini, E., Marisaldi, M., Mastropietro, M., Mauri, A., Mereghetti, S., Morelli, E., Morselli, A., Pacciani, L., Pellizzoni, A., Perotti, F., Picozza, P., Pilia, M., Prest, M., Rapisarda, M., Rappoldi, A., Rossi, E., Rubini, A., Scalise, E., Soffitta, P., Vallazza, E., Vercellone, S., Zambra, A., Zanello, D., Pittori, C., Verrecchia, F., Giommi, P., Colafrancesco, S., Santolamazza, P., Antonelli, A., & Salotti, L. 2009, Nature, 462, 620

Telesco, C. M. & Harper, D. A. 1980, ApJ, 235, 392

Thompson, R. I., Rieke, G. H., Tokunaga, A. T., & Lebofsky, M. J. 1979, ApJ, 234, L135

Titarchuk, L. & Shrader, C. R. 2002, ApJ, 567, 1057

Tonry, J. L., Dressler, A., Blakeslee, J. P., Ajhar, E. A., Fletcher, A. B., Luppino, G. A., Metzger, M. R., & Moore, C. B. 2001, ApJ, 546, 681

Tozzi, P., Rosati, P., Nonino, M., Bergeron, J., Borgani, S., Gilli, R., Gilmozzi, R., Hasinger, G., Grogin, N., Kewley, L., Koekemoer, A., Norman, C., Schreier, E., Szokoly, G., Wang, J. X., Zheng, W., Zirm, A., & Giacconi, R. 2001, ApJ, 562, 42

Truemper, J. 1982, Advances in Space Research, 2, 241

van den Bergh, S. 2000, PASP, 112, 529

van den Heuvel, E. P. J. 1975, ApJ, 198, L109

van den Heuvel, E. P. J. 1994, in Saas-Fee Advanced Course 22: Interacting Binaries, ed. S. N. Shore, M. Livio, E. P. J. van den Heuvel, H. Nussbaumer, & A. Orr, 263–474

van den Heuvel, E. P. J., Bhattacharya, D., Nomoto, K., & Rappaport, S. A. 1992, A&A, 262, 97

van der Klis, M. 2004, ArXiv Astrophysics e-prints

van Kerkwijk, M. H., Charles, P. A., Geballe, T. R., King, D. L., Miley, G. K., Molnar, L. A., van den Heuvel, E. P. J., van der Klis, M., & van Paradijs, J. 1992, Nature, 355, 703

Verbunt, F. 1987, ApJ, 312, L23

Verbunt, F. 2002, in Astronomical Society of the Pacific Conference Series, Vol. 265, Omega Centauri, A Unique Window into Astrophysics, ed. F. van Leeuwen, J. D. Hughes, & G. Piotto, 289

Verbunt, F. & van den Heuvel, E. P. J. 1995, X-ray Binaries, 457

Vladimirskiĭ, B. M., Gal'per, A. M., Luchkov, B. I., & Stepanyan, A. A. 1985, Soviet Physics Uspekhi, 28, 153

Voss, R. & Gilfanov, M. 2006, A&A, 447, 71

Voss, R., Gilfanov, M., Sivakoff, G. R., Kraft, R. P., Jordán, A., Raychaudhury, S., Birkinshaw, M., Brassington, N. J., Croston, J. H., Evans, D. A., Forman, W. R., Hardcastle, M. J., Harris, W. E., Jones, C., Juett, A. M., Murray, S. S., Sarazin, C. L., Woodley, K. A., & Worrall, D. M. 2009, ApJ, 701, 471

Walter, F., Weiss, A., & Scoville, N. 2002, ApJ, 580, L21

Waltman, E. B., Ghigo, F. D., Johnston, K. J., Foster, R. S., Fiedler, R. L., & Spencer, J. H. 1995, AJ, 110, 290

Walton, D. J., Roberts, T. P., Mateos, S., & Heard, V. 2011, MNRAS, 416, 1844

Watson, M. G., Schröder, A. C., Fyfe, D., Page, C. G., Lamer, G., Mateos, S., Pye, J., Sakano, M., Rosen, S., Ballet, J., Barcons, X., Barret, D., Boller, T., Brunner, H., Brusa, M., Caccianiga, A., Carrera, F. J., Ceballos, M., Della Ceca, R., Denby, M., Denkinson, G., Dupuy, S., Farrell, S., Fraschetti, F., Freyberg, M. J., Guillout, P., Hambaryan, V., Maccacaro, T., Mathiesen, B., McMahon, R., Michel, L., Motch, C., Osborne, J. P., Page, M., Pakull, M. W., Pietsch, W., Saxton, R., Schwope, A., Severgnini, P., Simpson, M., Sironi, G., Stewart, G., Stewart, I. M., Stobbart, A.-M., Tedds, J., Warwick, R., Webb, N., West, R., Worrall, D., & Yuan, W. 2009, A&A, 493, 339

Weiß, A., Neininger, N., Hüttemeister, S., & Klein, U. 2001, A&A, 365, 571

Weisskopf, M. C., Tananbaum, H. D., Van Speybroeck, L. P., & O'Dell, S. L. 2000, in Society of Photo-Optical Instrumentation Engineers (SPIE) Conference Series, Vol. 4012, Society of Photo-Optical Instrumentation Engineers (SPIE) Conference Series, ed. J. E. Truemper & B. Aschenbach, 2–16

Welch, G. A., Sage, L. J., & Young, L. M. 2010, ApJ, 725, 100

White, N. E., Nagase, F., & Parmar, A. N. 1995, X-ray Binaries, 1

Yan, L.-H. & Wang, J.-C. 2011, Research in Astronomy and Astrophysics, 11, 631

Yu, W. & Yan, Z. 2009, ApJ, 701, 1940

Zampieri, L. & Roberts, T. P. 2009, MNRAS, 400, 677

Zdziarski, A. A., Poutanen, J., & Johnson, W. N. 2000, ApJ, 542, 703

Zepf, S. E. & Ashman, K. M. 1993, MNRAS, 264, 611

Zepf, S. E., Maccarone, T. J., Bergond, G., Kundu, A., Rhode, K. L., & Salzer, J. J. 2007, ApJ, 669, L69

Zepf, S. E., Stern, D., Maccarone, T. J., Kundu, A., Kamionkowski, M., Rhode, K. L., Salzer, J. J., Ciardullo, R., & Gronwall, C. 2008, ApJ, 683, L139

Zhang, F., Han, Z., Li, L., & Hurley, J. R. 2004, A&A, 415, 117

Zhang, Z., Gilfanov, M., Voss, R., Sivakoff, G. R., Kraft, R. P., Brassington, N. J., Kundu, A., Jordán, A., & Sarazin, C. 2011, A&A, 533, A33

Zhu, C., Lü, G., Wang, Z., & Wang, N. 2012, PASP, 124, 195